MODELING AND EXPERIMENTAL VALIDATION OF ELECTROPLATING DEPOSIT DISTRIBUTIONS IN COPPER SULFATE SOLUTIONS

by

Mark Robert Robison

A thesis submitted to the faculty of
The University of Utah
in partial fulfillment of the requirements for the degree of

Master of Science

Department of Metallurgical Engineering

The University of Utah

May 2014

The University of Utah Graduate School

STATEMENT OF THESIS APPROVAL

The thesis of **Mark Robert Robison**

has been approved by the following supervisory committee members:

Michael Free	, Chair	**2/28/2014**
		Date Approved
Zhigang Zak Fang	, Member	**2/28/2014**
		Date Approved
Keith Prisbrey	, Member	
		Date Approved

and by **Manoranjan Misra** , Chair/Dean of

the Department/College/School of Metallurgical Engineering

and by David B. Kieda, Dean of The Graduate School.

ABSTRACT

Uniform deposits are typically desired in electrodeposition; however, the geometry of the deposited surface often makes a uniform deposit difficult to achieve. The objectives of this thesis are to provide experimental and modeling data for deposit uniformity of several geometries in a copper sulfate solution and to create a model capable of predicting deposit uniformity on any geometry. Bench scale electroplating cells were set up to test deposit distributions of multiple geometries as well as to test deposit uniformity with varying copper concentrations and temperatures ranging from 30 g/L to 50 g/L Cu^{2+} and 30 °C to 60 °C. The deposit uniformity was determined by cross-sectioning the samples.

Models were generated using a finite element analysis-based software package named COMSOL Multiphysics. The model results were compared to experimental results to verify model accuracy. Model results were determined to be accurate as long as the cathode size was not too small. In addition, a numerical model was developed based on cell geometry, current density, and limiting current density. This numerical model was compared with the COMSOL model, and the results show very good agreement between the two models. Results from the electrodeposition experiments, COMSOL model, and numerical model can be used to predict copper electrodeposition profiles and uniformity in a wide range of conditions and geometries.

To my loving wife

TABLE OF CONTENTS

LIST OF TABLES

Table Page

CHAPTER 1

INTRODUCTION

1.1 Copper Electrodeposition

Copper is one of the most commonly electrodeposited metals and is used in a wide variety of applications such as plastics, printed wiring boards, zinc die castings, heat treatment, automotive and aerospace coatings, electrorefining, electrowinning, and electroreforming. Electrodeposited copper has excellent coverage on irregularly shaped parts as well as very high plating efficiency. Once deposited, copper coatings retain the typical properties of copper such as high conductivity and corrosion resistance (*1, 2*).

There are several types of plating baths used to electrodeposit copper which include acid copper, cyanide copper, and pyrophosphate systems (*3*). Although all three systems can be found in use today, acid copper plating is the most common system used for copper electrodeposition. Within acid copper plating there are many more varieties of baths, although the major baths used in industrial applications are sulfate and fluoborate baths. This study will focus on sulfate based acid copper electrodeposition.

1.2 Electrodeposition Thermodynamics

In copper electrodeposition, electrodes are immersed in a solution containing copper, and an electrical current is applied to the electrodes. The current goes into the

negative electrode, called the cathode, through the solution and into the positive electrode, called the anode. As this current flows, copper ions in the solution gain electrons and deposit on the cathode. This reaction at the cathode is written as

$$Cu^{2+}_{(aq)} + 2e^- \leftrightarrow Cu_{(s)} \quad \textbf{(1.1)}$$

The standard electrode pote4ntial for the above reaction is 0.34 V. If the anode is made of copper, as in electrorefining, the reaction at the anode is the reverse of the above equation. If the anode is an inert material such as lead or platinum, the standard electrode potential is 1.23 V. At the anode, water or hydroxyl ions are dissociated into oxygen and hydrogen ions as shown in eq 1.2.

$$H_2O_{(l)} \leftrightarrow 2H^+_{(aq)} + 2e^- + \frac{1}{2}O_{2(g)} \quad \textbf{(1.2)}$$

In the case of an inert anode, the overall standard cell potential is 0.89 V (1.23 V – 0.34 V). This is the reversible potential for the reaction. In practice, solution resistances, contact resistances, and overvoltages cause the actual applied voltage to be much higher than 0.89 V. The applied potential for deposition can be expressed as:

$$\begin{aligned} \Delta V_{applied} = {} & \Delta V_{Half\ Cell} + \Delta V_{cathodic\ overpotential} \\ & + \Delta V_{anodic\ overpotential} \\ & + \Delta V_{solution+contact+misc.} \end{aligned} \quad \textbf{(1.3)}$$

which can alternatively be expressed as

$$V_{applied} = E_{anodic} - E_{cathodic} + \eta_{anodic} + \eta_{cathodic} + IR_{solution} + IR_{other} \quad \textbf{(1.4)}$$

If the applied potential is less than the cell potential and the combined resistances, deposition will not occur. In addition, if the applied potential is not significantly greater than the cell potential and resistances, deposition may be too slow to be of any practical use.

If the anode is made from copper, the overall cell potential is 0 V because the same reaction happens at both the cathode and the anode. The applied potential only needs to overcome solution resistance and overvoltage for deposition to occur. This greatly reduces the energy requirement to deposit copper using copper anodes; however, as the copper is deposited, the copper anode dissolves and changes the shape and surface area of the anode, which can be a problem for some electrodeposition applications.

The cell potentials mentioned above are the potentials if the solution is at 298 K, 1 bar, and the activities of the reactants are unity. In practical applications, the conditions do not match standard values, so an analysis of the free energy is used to determine how the reaction will proceed under nonstandard conditions. The standard free energy of a reaction can be calculated by using eq 1.5.

$$\Delta G^0_{reaction} = \Sigma \Delta G^0_{products} - \Sigma \Delta G^0_{reactants} \quad \textbf{(1.5)}$$

In the case of deposited metal, the standard free energy of formation is zero, and the values of the dissolved species at standard atmospheric conditions can be found in literature. If the free energy is negative, then the reaction will proceed forward, but if the

free energy is positive, the reaction will go backward and consume products and create reactants.

For nonstandard conditions, eq 1.6 can be used to calculate the free energy

$$\Delta G_{reaction} = \Sigma \Delta G^0_{reaction} + RT \ln Q \quad \textbf{(1.6)}$$

where

R is the universal gas constant,

T is the absolute temperature, and

Q is the ratio of products to reactants with the appropriate stoichiometric consideration.

Although free energy has its uses, it cannot be directly measured. The potential in an electrochemical reaction can be easily measured: Equation 1.7 and eq 1.8 can be used to predict the cell potential of a reaction under nonstandard conditions from a free energy calculation.

$$G = -nFE \quad \textbf{(1.7)}$$

$$E = E_0 - \frac{RT}{nF} \ln Q \quad \textbf{(1.8)}$$

Equation 1.8 is known as the Nernst equation, where *n* is the number of electrons transferred in the reaction, *F* is the Faraday constant, and E_0 is the potential under standard conditions.

When current is applied to an electroplating cell, electrons are supplied to the cathode and electrons are removed from the anode. If electrons are supplied to the cathode faster than the electrochemical reaction at the cathode can take place, a buildup of electrons occurs at the cathode. Correspondingly, the anode may have a deficiency of electrons. As the electrons build up or become depleted, the electrodes become polarized and their potentials deviate from the equilibrium potential. This change in potential from the equilibrium potential for a specific half-cell reaction is called the overpotential, η. The overpotential is simply equal to $E - E_{eq}$, where E is the electrode potential and E_{eq} is the equilibrium potential for a specific half-cell reaction.

1.3 Electrodeposition Kinetics

Free energy and reaction potential are thermodynamic quantities. A kinetic expression is needed to predict an electrochemical reaction rate. Results from the Nernst Equation can then be applied to eq 1.9 to predict the current density and thus reaction rate of the electrochemical reaction. The Butler–Volmer equation is

$$i = i_0 \left[\exp\left(\frac{\alpha_a F \eta_a}{RT}\right) - \exp\left(-\frac{\alpha_c F \eta_c}{RT}\right)\right] \qquad \textbf{(1.9)}$$

where

i is the current density,

i_0 is the exchange current density,

α_a is the anodic charge transfer coefficient,

α_c is the cathodic charge transfer coefficient,

η_c is the overpotential at the cathode, and

η_a is the overpotential at the anode.

At equilibrium, there exists a small amount of current between the electrode and electrolyte that balances, resulting in a net current of zero. The exchange current density is that current density at equilibrium. When the potential is either increased or decreased from equilibrium potential, the Butler–Volmer equation describes the net current density.

The Butler–Volmer equation assumes the reaction is controlled by the electrical charge transfer without any consideration for mass transfer limitations. In many cases, mass transfer is slow compared to the reaction, and reactant concentrations in the vicinity of the electrodes can be depleted. By adding in terms to account for the mass transfer limitations the Butler–Volmer Equation becomes

$$i = i_0 \left[\frac{\mathrm{C_O}}{\mathrm{C_O^*}} \exp\left(\frac{\alpha_a n F \eta}{RT}\right) - \frac{\mathrm{C_R}}{\mathrm{C_R^*}} \exp(-\frac{\alpha_c n F \eta}{RT})\right] \qquad \textbf{(1.10)}$$

where

$\mathrm{C_O}$ is the concentration of the oxidized species,

$\mathrm{C_O^*}$ is the initial concentration of the oxidized species in the bulk solution,

$\mathrm{C_R}$ is the concentration of the reduced species, and

$\mathrm{C_R^*}$ is the initial concentration of the reduced species in the bulk solution.

Mass transfer in solution has two main mechanisms, diffusion and convection. Diffusion is driven by the concentration gradient in a solution according to Fick's first law:

$$N = KA(C_{bulk} - C) \quad \textbf{(1.11)}$$

where

N is the molar mass transfer rate,

K is the mass transfer coefficient,

A is the area of mass transfer,

C_{bulk} is the concentration of the species in the bulk solution, and

C is the local concentration of the species.

The diffusivity of a species in solution can be described as

$$D = D_0 \exp\left(-\frac{E_A}{RT}\right) \quad \textbf{(1.12)}$$

where

D is the diffusivity,

D_0 is the maximum diffusion coefficient (the diffusivity at infinite temperature), and

E_A is the activation energy for diffusion.

The limiting current density is the maximum amount of current that can be carried by a solution before mass transfer limitations prevent the reaction from proceeding any faster. Additional current can be applied to the cell; however, the current can only affect side reactions, such as electrolysis, where hydrogen and oxygen are generated at the electrodes.

$$i_l = \frac{nFD(C_{bulk} - C)}{\delta} \quad \textbf{(1.13)}$$

where

i_l is the limiting current density,

δ is the thickness of the diffusion layer, and

D is the diffusivity.

To increase the mass transfer and thus the limiting current density, the bulk concentration of the solution can be increased, diffusivity can be increased by increasing the temperature, or the thickness of the diffusion layer can be decreased by increased solution agitation.

Convection in a plating solution can be either passive or active convection. Passive convection can be created by temperature gradients caused by uneven heating and cooling in the plating cell or by concentration gradients caused by consumption of reactants at the cathode and generation of reactants at the anode. Active forms of convection are typically referred to as agitation. More common methods of agitation are air agitation produced by bubbling air into the bottom of the plating cell or mechanical agitation produced either by propellers in the solution or by external pumps pumping solution through nozzles or through eductors in solution.

1.4 Electrodepositon Geometry

The geometry of a plating cell can often have a greater influence on the plating performance than the solution chemistry. Electrodeposition on irregularly shaped surfaces can result in large differences in the deposit distribution. Recessed areas will

have depleted levels of reactant while more accessible areas are able to replenish faster than the recessed areas. Recessed areas also have higher solution resistance as a result of a longer distance for the current to travel through solution.

CHAPTER 2

LITERATURE

2.1 Speciation of Copper Sulfate

The composition of an aqueous system of copper sulfate and sulfuric acid depends on many factors, such as copper sulfate concentration, sulfuric acid concentration, pH, and temperature. The species present in such a system include 11 distinct species (*4*); however, the most important species are $CuSO_4$, Cu^{2+}, SO_4^{2-}, H_2SO_4, HSO_4^-, and H^+. Bath compositions under various conditions have been studied and can be found in literature. At 25 ºC and in the range of concentrations in this study (30 to 50 g/L Cu^{2+}), approximately 6 to 7% of the copper sulfate exists as $CuSO_4$ with the balance as dissociated Cu^{2+}, SO_4^{2-} (*4*).

In this study, the model made the simplifying assumption that all species were completely dissociated as Cu^{2+}, SO_4^{2-}, and H^+. Including all species in the model would have been possible; though, determining diffusivity values for each species under each set of conditions would have been difficult and was beyond the scope of this study.

2.2 Copper Sulfate Diffusivity

Diffusivity of the species present in the solution was treated as an overall diffusivity rather than as a diffusivity of each species individually. As mentioned

previously, determining the diffusivity values of all the species present in solution under all of the experimental conditions would be very difficult and beyond the scope of this study. The overall diffusivity at each set of experimental conditions was determined from literature and entered into the model.

Many values of copper diffusivity in copper sulfate have been published in literature; however, the diffusivity values often conflict with other reported values (*5*). Papers reporting copper diffusivity tend to only include experiments at 25 °C, which is not useful for application in a model at higher temperatures.

Diffusivity values used in the model were calculated using data from Moats et al. (*6*). This paper included diffusivity values with varying concentrations and temperatures relevant to copper electrorefining, and the conditions in this study fit within the conditions in Moats et al.

Experimental values for the diffusion constant at 65 °C were back calculated using eq 2.1 and plotted in Figure 2.1. A linear regression was used to estimate the diffusion constant, D_0, at varying copper concentrations, shown in Figure 2.1. The slope of the fitted line was used to estimate the value of the diffusion constant, and this value was used in eq 2.1 to predict the diffusivity at varying concentrations and temperatures.

$$D = D_0 e^{-E_a/RT} \qquad \textbf{(2.1)}$$

where

D is the diffusivity,

D_0 is the diffusion constant, and

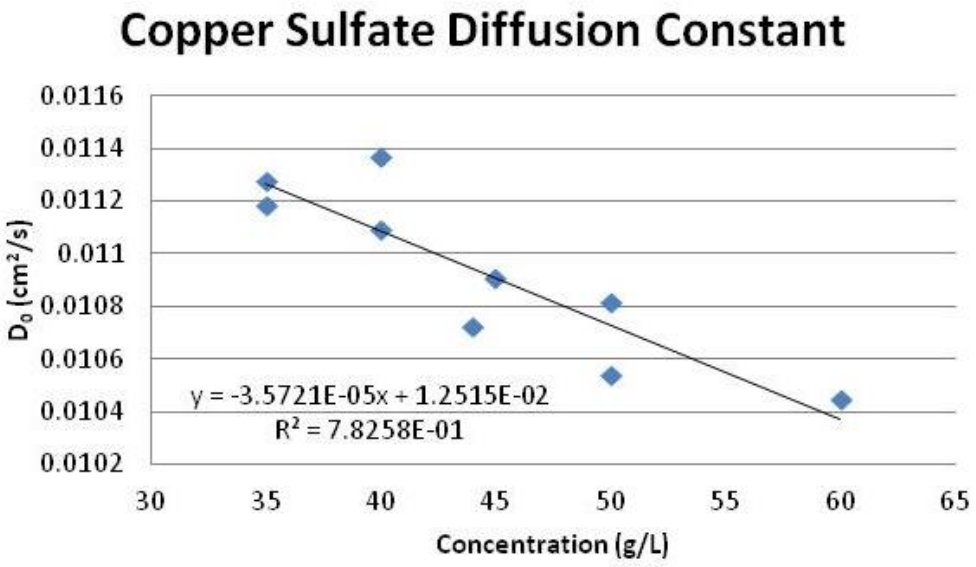

Figure 2.1 Linear regression of experimental data from Moats et al. (*6*) to solve for the diffusion constant

E_a is the activation energy of diffusion.

The resulting equation was then compared to the data from Moats et al. (*6*) and was shown to have acceptable accuracy over the range of temperatures and concentrations relevant to industrial copper electrodeposition. Calculated diffusivity values and their corresponding experimental values are shown in Table 2.1.

Equation 2.2 was used to calculate the diffusivity in the model.

$$D = ((Cu*(-3.57214e-5)+1.25148e-2)*\exp(-19.2/.008314/T) \quad \textbf{(2.2)}$$

where

Cu is the copper concentration in g/L, and

T is the temperature in K.

This equation was derived from data where the concentration of H_2SO_4 is 160 g/L.

2.3 Throwing Power

Deposit distribution is heavily dependent on the geometry of the cathodes, anodes, and the plating cell in general. Therefore, comparing the deposit distributions of different plating cells often does not provide any useful information. The term *throwing power* was developed in order to quantitatively describe the plating behavior of an electroplating bath to provide a more systematic way of comparing plating solutions independent of the geometry.

Many papers have been written on the subject of electrodeposit distribution, with the first major paper written in 1923 by Haring and Blum (*7*). Their paper proposed a

Table 2.1

Calculated and Experimental Diffusivity Values

T C	T K	Concentration g/L	D_0 cm^2/s	D cm^2/s	$D_{experimental}$ cm^2/s
40	313.15	40	0.0111	6.95E-06	6.87E-06
45	318.15	40	0.0111	7.80E-06	7.69E-06
50	323.15	40	0.0111	8.73E-06	8.62E-06
60	333.15	40	0.0111	1.08E-05	1.07E-05
65	338.15	35	0.0113	1.22E-05	1.22E-05
65	338.15	40	0.0111	1.20E-05	1.23E-05
65	338.15	45	0.0109	1.18E-05	1.18E-05
65	338.15	50	0.0107	1.16E-05	1.14E-05

systematic way of defining an electrodeposit distribution, which they called *throwing power*. They defined *throwing power* as "the deviation (in percent) of the metal distribution ratio from the primary current distribution ratio." The equation they developed to describe throwing power is

$$T = 100\left[1 - \frac{D_n}{D_f}\left(1 - \frac{e_f - e_n}{E_f}\right)\right] \quad \textbf{(2.3)}$$

If the current efficiencies are equal, then the equation for throwing power could also be written as

$$T = 100\left(\frac{e_f - e_n}{E_f}\right) \quad \textbf{(2.4)}$$

By replacing E_f with $I_f\ KR_n$ the equation becomes

$$T = 100\left(\frac{e_f - e_n}{I_f} * \frac{1}{KR_n}\right) \quad \textbf{(2.5)}$$

where

T is the throwing power of the solution,

D_n is the cathode efficiency at the near surface of the cathode,

D_f is the cathode efficiency at the far surface of the cathode,

e_f is the potential at the far surface of the cathode,

e_n is the potential at the near surface of the cathode,

E_f is the potential drop through solution to the far surface of the cathode,

I_f is the current density at the far surface of the cathode,

K is the ratio of the solution resistance between cathode and anode at the far and near surfaces, which is determined by the physical arrangement of the cell (electrode shape, distances, orientation, etc.), and

R_n is the effective resistance through the solution from the anode to the near surface of the cathode.

Therefore, in the Haring–Blum model the throwing power is a function of

(1) potentials at the cathode during the passage of current,

(2) current density at the far surface of the cathode,

(3) resistivity of the solution, and

(4) physical arrangement of the cell.

Haring and Blum also proposed a standardized method of experimentally determining throwing power by using a cell (later known as a Haring–Blum cell), which has an anode with two cathodes at different distances from the anode on opposite sides of the anode. The cell measures 10 cm by 10 cm by 60 cm with the cathodes on each end of the cell. The anode can be placed at varying locations to achieve different distance ratios between the anode and cathodes. This cell produces the deposit distribution ratio that is used in eq 2.3.

This way of representing throwing power produces a value from infinity to negative infinity which is not a very practical way of describing throwing power. While the Haring–Blum method is useful for a more theoretical approach, it is not as practical for use in the electroplating industry. Because of this limitation, several papers have

since been published proposing more practical methods of determining throwing power and deposit distribution.

Jelinek and David (*8*) have proposed a linear throwing power index to describe the throwing power of a solution. This index is based on a plot of the metal distribution ratio versus the linear ratio, which then has a line connecting the point L = 1 and M = 1 and the experimental result. The throwing index is the reciprocal of the slope of the connecting line. This gives the linear throwing index in eq 2.6.

$$a = \frac{L - 1}{M - 1} \qquad \textbf{(2.6)}$$

This throwing index has the advantage of being very simple with only two easily measured variables; however, it loses accuracy over wide ranges of concentrations or temperatures. While not very well suited for theoretical research, this method of determining throwing power is advantageous in industry where the range of concentrations and temperatures is typically very small and very little data is collected on a continuous basis.

Chin (*9*) has proposed a logarithmic throwing index in order to provide a throwing index that will describe a solution's behavior over a wide range of linear ratios, something the linear throwing index fails to accomplish. Chin found that a logarithmic mathematical relationship is more accurate, which is shown as eq 2.7.

$$M = L^{1/A} \qquad \textbf{(2.7)}$$

which can also be written as

$$A = \frac{\log L}{\log M} \qquad \textbf{(2.8)}$$

Assaf (*10*) developed a simple and effective method to determine the throwing power of plating baths. In this method, a small metal plate is plated in the solution followed by a measurement of the thicknesses on the front and back of the plate. The ratio of the difference between the thicknesses on the front and back is representative of the throwing power of the solution. This method is simple, intuitive, and faster than the other methods discussed.

CHAPTER 3

EXPERIMENTAL PROCEDURES

Two phases of experiments were completed; the first phase used a Hull Cell to create a deposit distribution in a well-recognized and standardized geometry. In the second phase, copper was electrodeposited on different shaped cathodes from a flat copper anode.

3.1 Hull Cell

For the Hull Cell experiments, the interior dimensions of the Hull Cell are shown in Figure 3.1. The solution level was approximately 50 mm high, which required a volume of 267 mL. The volume of the cell was designed to be small enough to require very little chemical to run a test while at the same time being an even multiple of a gallon to simplify calculating additions to plating tanks (*11*). The Hull Cell setup has a cathode with varying distances from the anode, which is designed to test the plating quality of a plating bath over a range of current densities (*12*). Approximate local current densities are typically read from a scale designed specifically for Hull Cell plating shown in Figure 3.2 (*13*).

In this study, a Hull cell was used to determine the electrodeposit distribution across varying concentrations and temperatures to characterize the throwing power of the

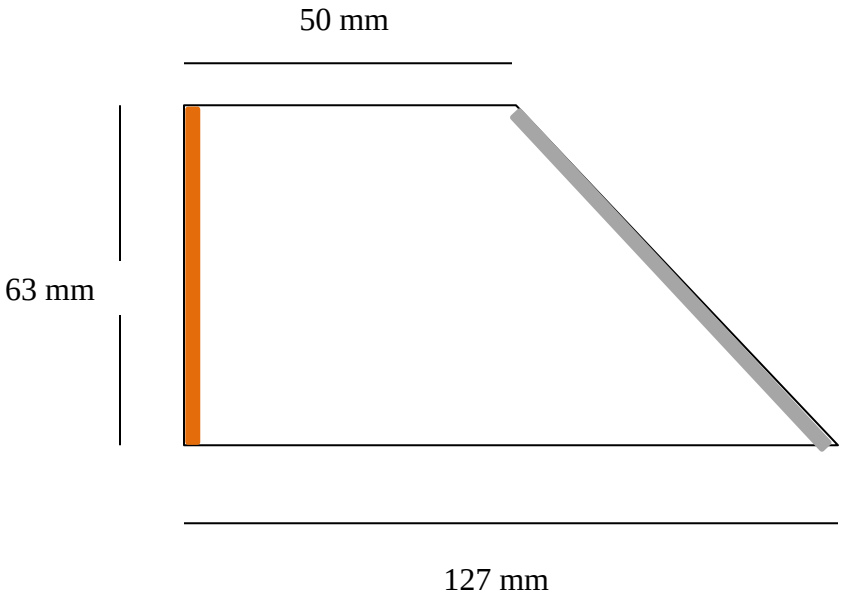

Figure 3.1 Interior dimensions of the Hull Cell

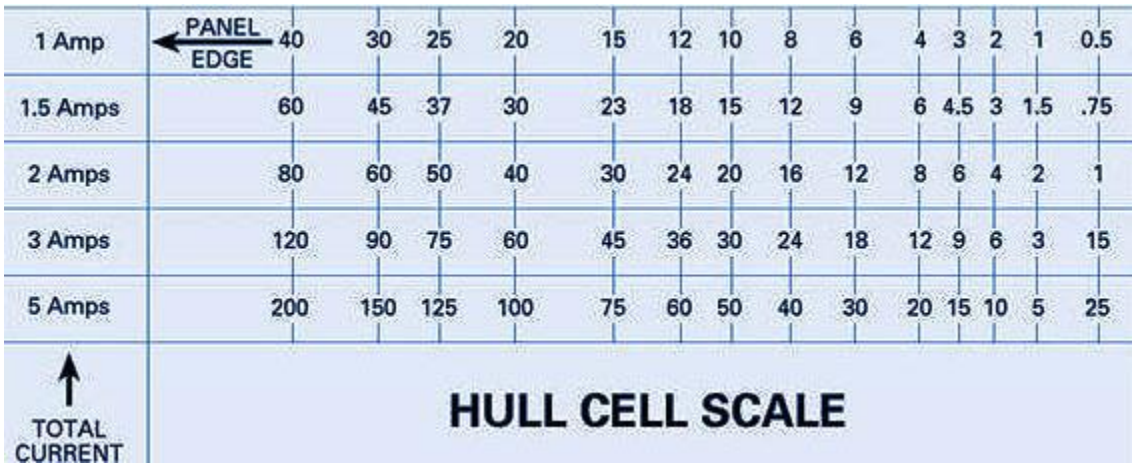

Figure 3.2 Hull Cell Scale showing approximate local current densities

solution. Each cathode was made from a 0.040-inch 316 stainless steel sheet cut 10 cm by 6 cm. Plater's tape was used to mask off most of the cathode, leaving a 2 cm by 10 cm horizontal strip exposed to the solution. The anode was a piece of copper masked in the same manner, but having a 2 cm by 6 cm strip exposed to solution. Both exposed areas began 2 cm from the bottom of the cell. A picture of the experimental setup is shown in Figure 3.3.

Each sample was plated at 1500 mA for 30 seconds to ensure coverage of the entire surface was achieved. The initial flash of copper was followed by plating at 800 mA for 4 hours. The experimental conditions in each experiment are shown in Table 3.1.

Each solution also contained 160 g/L sulfuric acid, 42.9 µg/L thiourea, and 26.4 µg/L glue. Sulfuric acid concentrations in electrorefining and electrowinning often vary from 10 to 220 g/L, and a concentration of 160 g/L was chosen because it is a common concentration in industrial processes, and it is also within the ranges where both electrorefining and electrowinning operate (*14*). Without smoothing agents, the deposit became quite rough, which made it difficult to accurately measure the thickness of the deposit. Thiourea and glue are commonly used smoothing agents in industrial electrorefining and were added to the solution to smooth the deposit profile (*15*).

Following the copper deposition, the samples were removed from solution and rinsed in distilled water. The tape was removed, and the panel was rerinsed and then dried using compressed air. The stainless steel sheet was flexed to detach the copper deposit from the cathode sheet. The copper deposit was cut down the center axis to produce two 1 cm by 10 cm samples. To allow for easier mounting, one piece was again cut down the middle to produce two 1 cm by 5 cm samples. The two 1 cm by 5 cm

Figure 3.3 Hull Cell Experimental Setup

Table 3.1

Conditions in Hull Cell Experiments

Run Number	Cu Concentration (g/L)	Temperature (C)
1	30	50
2	45	40
3	60	30
4	45	40
5	60	50
6	45	40
7	45	40
8	45	40
9	30	30

pieces of the sample were bent in half and mounted in epoxy with the edge that was the centerline of the sample facing down. Black pigment was added to the epoxy during mixing to aid in measuring the thickness by creating more contrast between the copper deposit and the epoxy.

Once mounted, the samples were polished and viewed under an optical microscope. A custom software package based in the Zeiss AxioVision software was used to measure the thickness of the deposit. Multiple thickness measurements were taken of the deposits, and the results were stitched together in Microsoft Excel to generate a deposition profile for the entire deposit.

3.2 Shaped Cathodes

In the second phase, flat anodes were used to deposit copper on differently shaped cathodes. The cathodes were all 316 stainless steel and 7 cm tall. One sample was a 2-inch diameter pipe, a second was a 0.75-inch diameter pipe, a third was a 2-inch angle (1/8-inch thick), and a fourth was a 0.75-inch angle (1/8-inch thick). Teflon blocks were used to maintain the nearest point between the cathode and anode. The minimum distance was 1.2 cm for each experiment. The cathodes were 7 cm tall with a horizontal strip 3 cm tall running the length of the cathode open to the solution. The strip of cathode open to solution was 2 cm from the bottom of the cell, with the rest of the cathode masked using nail polish. The angled cathode surfaces included the inner radius of the angle and the two adjacent flat sections.

The pipe cathode surfaces include one half of the circumference of the pipe. The size of each cathode surface is shown in Table 3.2. The samples were plated at 80

Table 3.2

Dimensions of Plated Areas

Sample	Surface Dimensions
Large Angle	3 cm x 9 cm
Small Angle	3 cm x 2.8 cm
Large Pipe	3 cm x 8 cm
Small Pipe	3 cm x 3 cm

mA/cm^2 for 30 seconds immediately followed by 40 mA/cm^2 for 4 hours. After plating, the samples were rinsed in distilled water and dried. Samples were then mounted in epoxy before cutting. As in the first phase, black pigment was added to the epoxy during mixing to aid in measuring the thickness by creating more contrast between the copper deposit and the epoxy. Samples were cut so that the copper deposit was cut down the middle of the 3 cm wide deposit.

In accordance with the first phase, once mounted the samples were polished and viewed under an optical microscope. Again, a custom software package based in the Zeiss AxioVision software was used to measure the thickness of the deposit. Multiple thickness measurements of the deposits were made, and the results were stitched together in Microsoft Excel to generate a deposition profile for the entire deposit.

CHAPTER 4

MODELING

Modeling and simulations can be cost effective ways of predicting the behavior of an electroplating system, and much work has been done to develop various software packages for simulations. Simulations typically calculate the solution conductivity, electrode and solution potentials, solution concentration, current distribution, and deposit thickness.

Many mathematical models have been developed to describe an electrolyte's current distribution; however, the models are usually restricted to specific simplified geometries such as flat panels, rotating discs, or triangular geometries (*16–18*).

Commercially available software packages have been developed that can make modeling complex geometries possible. Software packages currently on the market include Cell Design, Elsyca, and COMSOL Multiphysics.

4.1 COMSOL Multiphysics Description

The software package used in this study is COMSOL Multiphysics with the Electrodeposition Module. COMSOL Multiphysics uses the finite element method to calculate model solutions. COMSOL Multiphysics was chosen because of its ability to combine electrodeposition and fluid flow into one model. In addition, the software.

package is capable of modeling in up to three dimensions.

The Tertiary Nernst–Planck interface was chosen to model the electrodeposition in all models in this study. The COMSOL manual describes the interface thus:

> The Electrodeposition, Tertiary Nernst–Planck interface accounts for the transport of species through diffusion, migration, and convection and is therefore able to describe the effects of variations in composition on the electrodeposition process. The kinetics expressions for the electrochemical reactions account for both activation and concentration overpotential. The Electrodeposition, Tertiary Nernst–Planck interface applies the equations of electroneutrality to the set of equations that describe the species and current balances. This also implies that all charged species in the electrolyte have to be defined in the simulations, except those species that are present at very low concentrations and can therefore be neglected in the balance of current.
>
> –*Introduction to Electrodeposition Module*, page 8 (*19*).

In the bulk fluid, the Nernst–Planck equation governs the mass transfer in the solution.

$$N_i = -D_i \nabla c_i - z_i \mu_i F c_i \nabla V \qquad \textbf{(4.1)}$$

where

N_i is the mass transport vector of the ith species,

D_i is the diffusivity of the ith species,

c_i is the concentration of the ith species,

z_i is the charge of the ith species,

μ_i is the mobility of the ith species,

F is the Faraday constant, and

V is the electric potential.

In this model, the mobility was estimated using the following relationship:

$$\mu = \frac{D}{RT} \quad \textbf{(4.2)}$$

where

R is the universal gas constant, and

T is the temperature of the solution.

In the Tertiary Nernst–Planck interface, the conductivity of the solution is governed by eq 4.3.

$$\sigma_l = F^2 \sum_{i=1}^{n} z_i^2 \mu_{m,i} c_i \quad \textbf{(4.3)}$$

This expression is an approximation that can introduce inaccuracies in the model. Equation 4.3 calculates the conductivity based on the mobility, which is in turn based on the diffusivity. In copper plating solutions, sulfuric acid is added to increase the conductivity, but adding sulfuric acid also decreases the diffusivity slightly. Therefore, the way COMSOL calculates the conductivity can cause conductivity to drop when sulfuric acid is added to the solution, even though literature reports an opposite effect (*4*). COMSOL does allow the user to define conductivity; however, this option is only possible for models using secondary current distribution. When using tertiary current distribution, conductivity must be calculated using eq 4.3 without any option to define conductivity manually. The effect of this limitation of the model was minimized by running all models in this study with a constant sulfuric acid concentration of 160 g/L, which is also the same concentration used to calculate the diffusivity of the solution.

At the electrodes, the boundary condition is governed by the Butler–Volmer equation. The model was run using concentration dependent kinetics, which means the form of the Butler–Volmer equation in eq 4.4 was used.

$$i = i_0 \left[\frac{C_O}{C_O^*}\exp\left(\frac{\alpha_a nF\eta}{RT}\right) - \frac{C_R}{C_R^*}\exp(-\frac{\alpha_c nF\eta}{RT})\right] \quad \textbf{(4.4)}$$

Diffusion coefficients were calculated using the data and methods described previously, treating the diffusivity as an overall diffusivity. Copper ions, sulfate ions, and hydrogen ions were all assumed to have the same overall diffusivity for each set of bath conditions. Complete dissociation of the copper and sulfate ions was also assumed. The cathodic and anodic symmetry factors were assumed to be 0.5 and 1.5, respectively (*20*). The chemical reaction of the copper deposition was assumed to be:

$$Cu^{2+}_{(aq)} + 2e^- \rightarrow Cu_{(s)} \quad \textbf{(4.5)}$$

4.2 Model Properties

All models in this study used 3-D geometries. The electrodeposition and laminar flow modules were utilized in conjunction to simulate copper electrodeposition in the various experiments.

All experimental cells were closed cells, and the only driving force for fluid flow in the model was the gravitational effects of the density gradients. As the copper concentration was depleted at the cathode or increased at the anode, the density gradients created a natural convection within the cell. The natural convection was created by

multiplying eq 4.6 (*21*) by the gravitational constant and inputting the result to the volume force in the negative z direction.

$$\rho = (1022+.00224*[Cu]+.00055*[H_2SO_4] -.58T \quad \textbf{(4.6)}$$

The value of the diffusion activation energy, E_a, in the model is 19.2 is kJ/mol (*5*, *6*). The exchange current density, i_0, was assumed to be 0.2 A/m^2 for all conditions (*20*).

The study solver was set to calculate both laminar flow and electrodeposition together, rather than separately, because of their interactions. The concentration gradients created from the addition of copper to the solution at the anode and from the removal of copper from the solution at the cathode generate density gradients that drive the natural convection in the cell. The solution flow in turn affects the deposition because the deposition rate is concentration dependent.

4.3 Hull Cell Model

The Hull Cell model used a plating cell with a geometry matching the description in Figure 3.1. The cathode and anode were 2 cm from the bottom of the cell, and the solution level was 5 cm from the bottom of the cell. Figure 4.1 shows the 3-D cell geometry.

The temperature and copper concentration in the solution was varied according to Table 4.1. The concentration of H_2SO_4 in all Hull Cell models was 160 g/L, and the

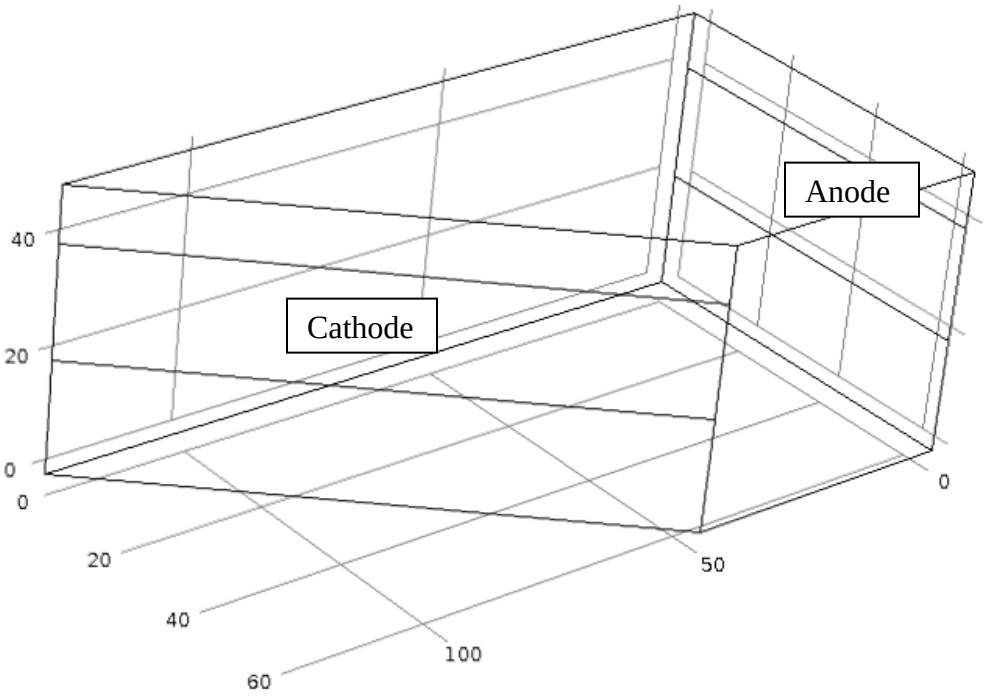

Figure 4.1 Hull Cell model geometry with units in mm.

Table 4.1

Copper Concentrations and Temperatures used in the Hull Cell model

Cu^{2+} (g/L)	Temperature (C)
30	30
30	60
40	45
50	30
50	60

deposit profile of the model was determined by generating a line plot of the thickness, which was drawn horizontally across the middle of the cathode.

4.4 Haring–Blum Model

Simulations of the Haring–Blum cell electrodeposition were generated by creating a cell geometry with a 60-cm by 10-cm by 10-cm cell full of electrolyte with cathodes at each end of the cell. A 1 mm thick anode was placed at a location 10 cm from one cathode and 50 cm from the other. The solution flow was generated by the laminar flow module and was governed by the density effects of the solution with no additional agitation.

Several variables were changed to simulate the conditions in each experimental run; the values for those variables are shown in Chapter 8. To determine the ratio of the deposition of copper on the two cathodes, a surface integration or the total mass change was calculated for each cathode.

4.5 Effects of Mesh on Model Results

The models in this study used a triangular mesh to create a network of nodes for calculation as shown in Figure 4.2. In a plating bath, if a nodule or other irregular feature grows out further than the surface around it, the nodule will continue to grow faster than the surface around it because of increased access to solution and lower resistance for current to flow to the feature. This effect is also seen in this model; nevertheless, it has some significant differences. The nodules are angular because of the nature of the mesh as no rounded curves are possible in a triangular mesh. Edges can be rounded out by

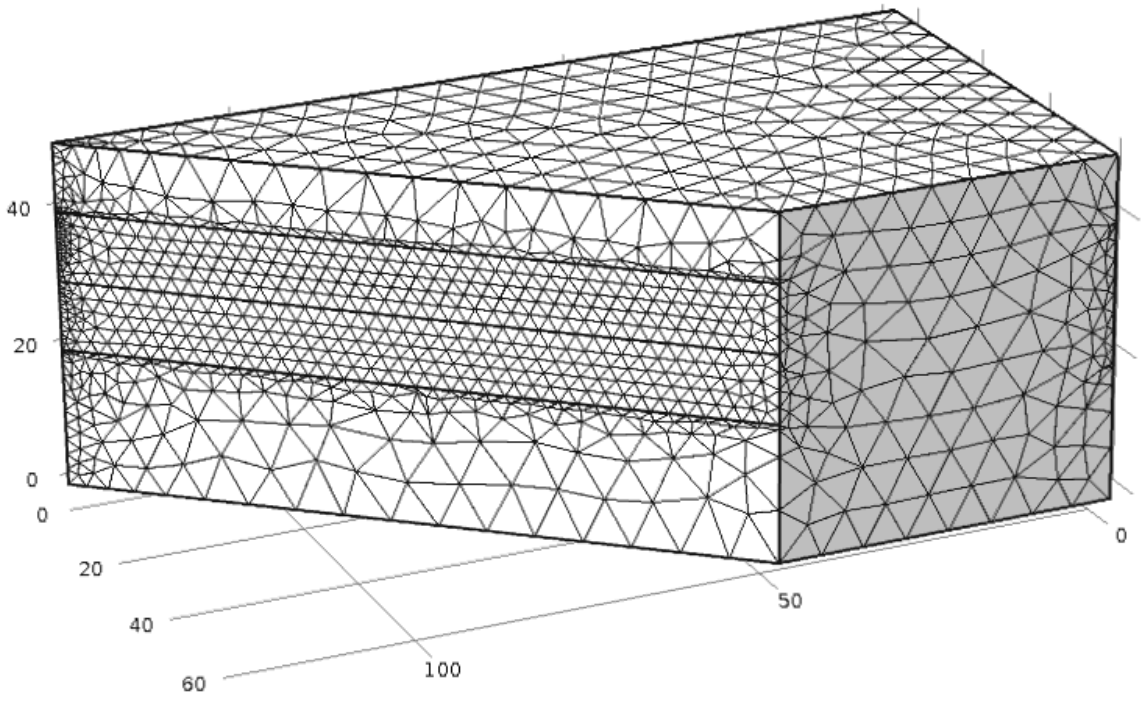

Figure 4.2 Triangular mesh in a Hull Cell model with units in mm

refining the mesh to approximate a rounded edge; yet, it can never be truly round.

Refining the mesh does not change the overall shape of the deposit; however, it has the effect of creating a rougher deposit as seen in Figure 4.3. In Figure 4.3, the refined, medium, and coarse meshes had maximum element sizes of 0.5 mm, 2.0 mm, and 3.5 mm, respectively, at the cathode surface. All models in this study used the medium mesh size, which is a predefined element size in COMSOL labeled *Extremely Fine*. The bulk solution had used a maximum mesh size of 8 mm, which is the predefined *Finer* setting.

An excessively rough model deposit could be smoothed by running multiple models and averaging the results of the models. This technique was used for the Hull Cell models to smooth the predicted deposits.

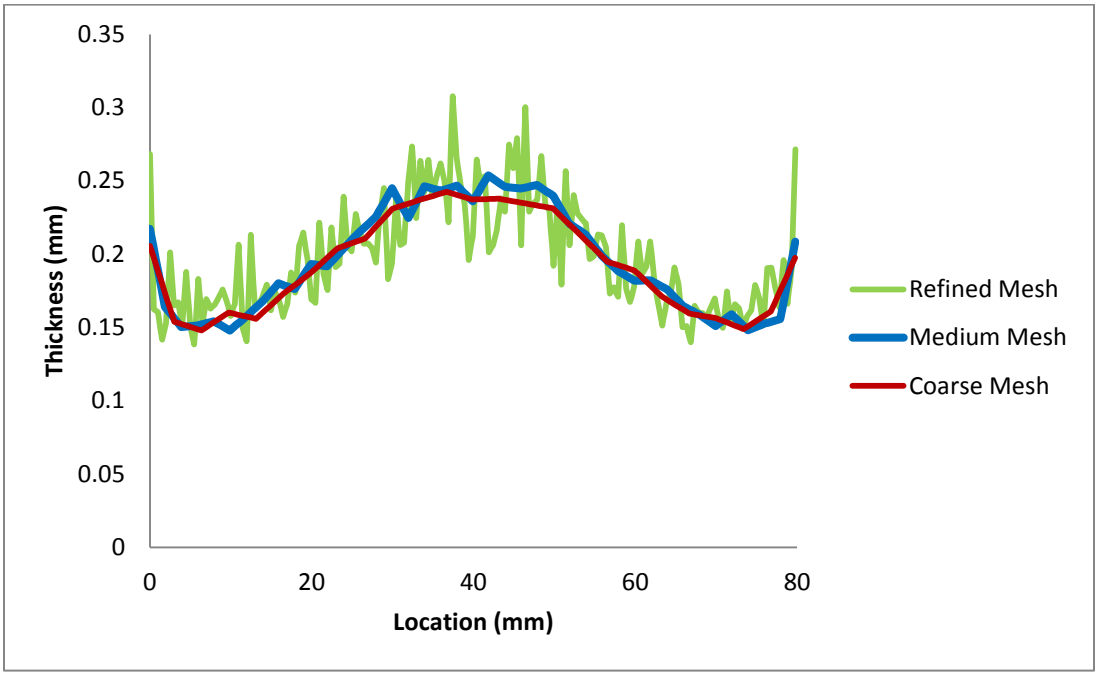

Figure 4.3 Predicted deposit distribution on a large pipe with different mesh sizes

CHAPTER 5

HULL CELL RESULTS AND DISCUSSION

5.1 Solution Flow

Figure 5.1 and Figure 5.2 show the velocity profile of the solution along the center of the cell with the units in m/s. In the model, the flow does not settle into a steady state flow, although the flow does maintain the same general flow. Figures 5.1 and 5.3 show the solution flow at 100s where the flow is still very uniform. As the simulation continues, some unusual flow patterns develop as shown in Figures 5.2, 5.4, and 5.5. The flow patterns develop because of the asymmetry of the plating cell and because of the varying density gradients across the cathode. As the solution circulates, crosscurrents develop that cause the flow patterns to become asymmetrical and irregular.

5.2 Current Density

The current density in the Hull Cell model as shown in Figure 5.6 has a higher density at the edges of the electrodes and the current spreads out into the solution as it travels between the electrodes, as expected.

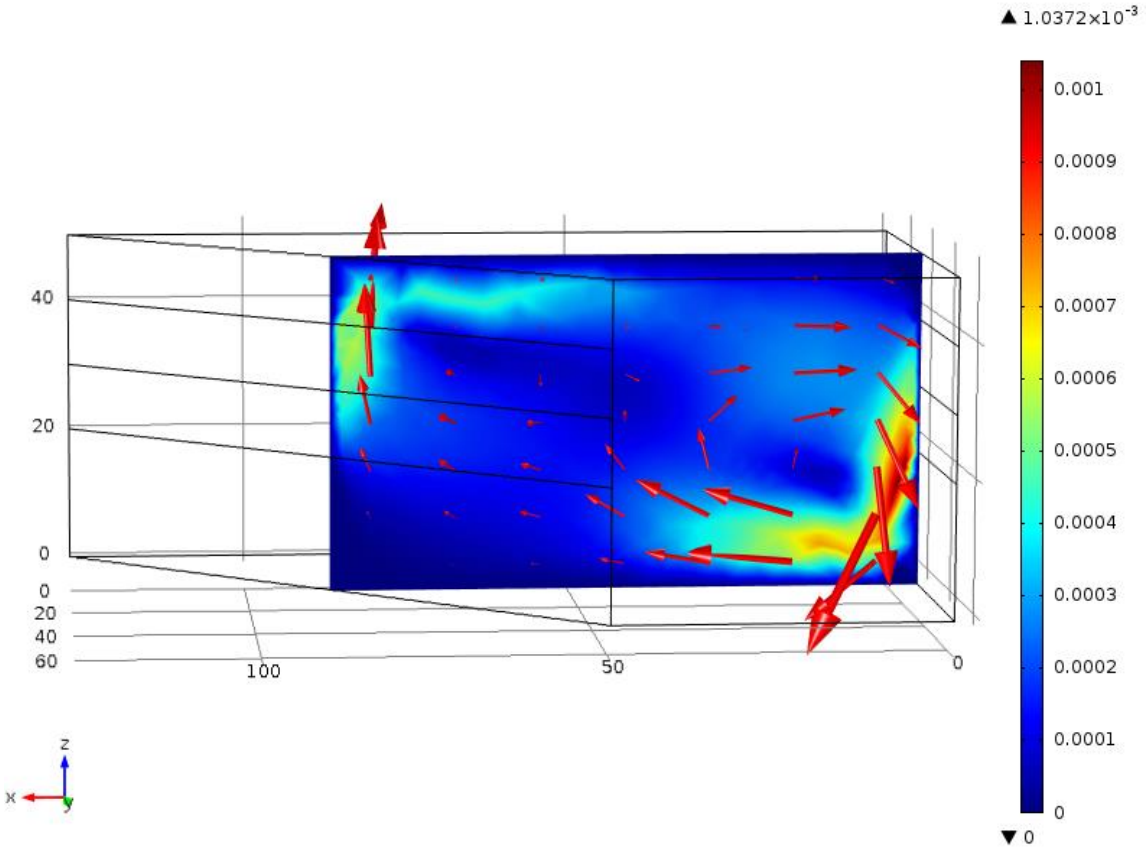

Figure 5.1 Model of the solution flow during electrodeposition with 40 g/L Cu^{2+}, 160 g/L H_2SO_4, 42.9 µg/L thiourea, and 26.4 µg/L glue at 45 °C and t = 100s

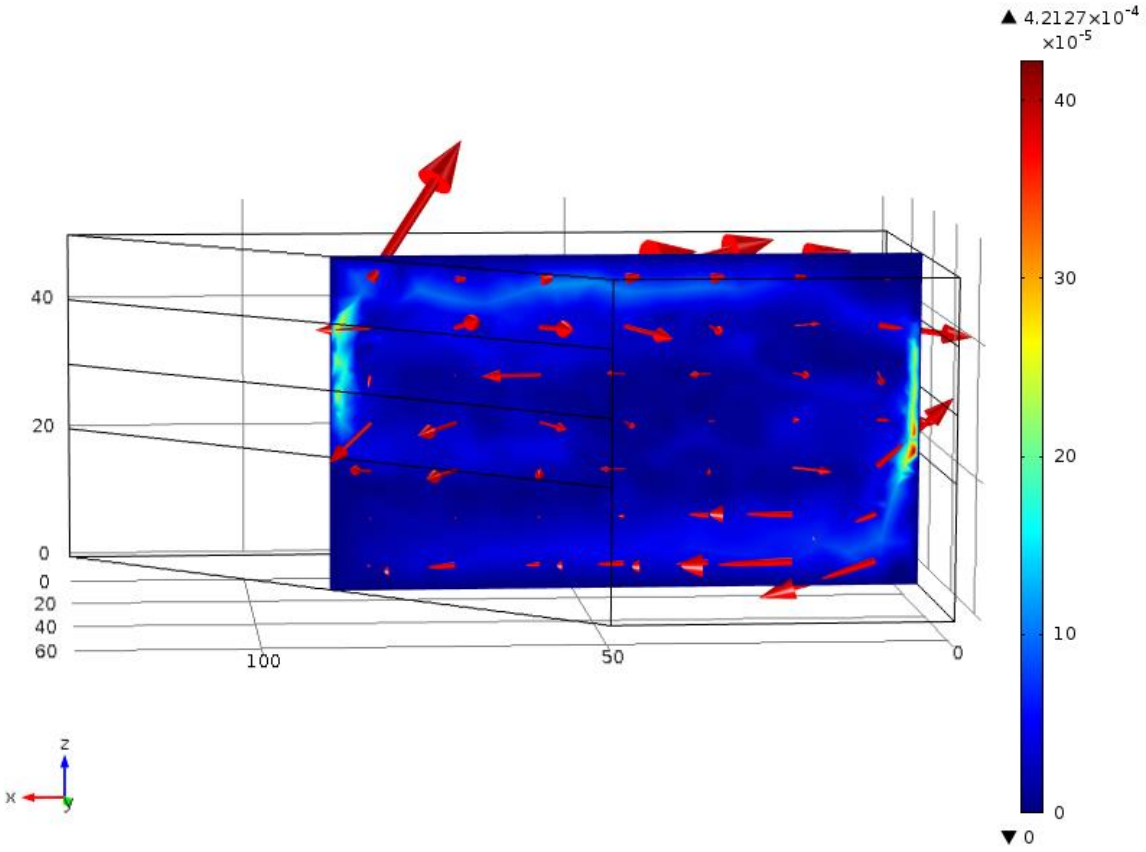

Figure 5.2 Model of the solution flow during electrodeposition with 40 g/L Cu^{2+}, 160 g/L H_2SO_4, 42.9 µg/L thiourea, and 26.4 µg/L glue at 45 °C and t = 14400s

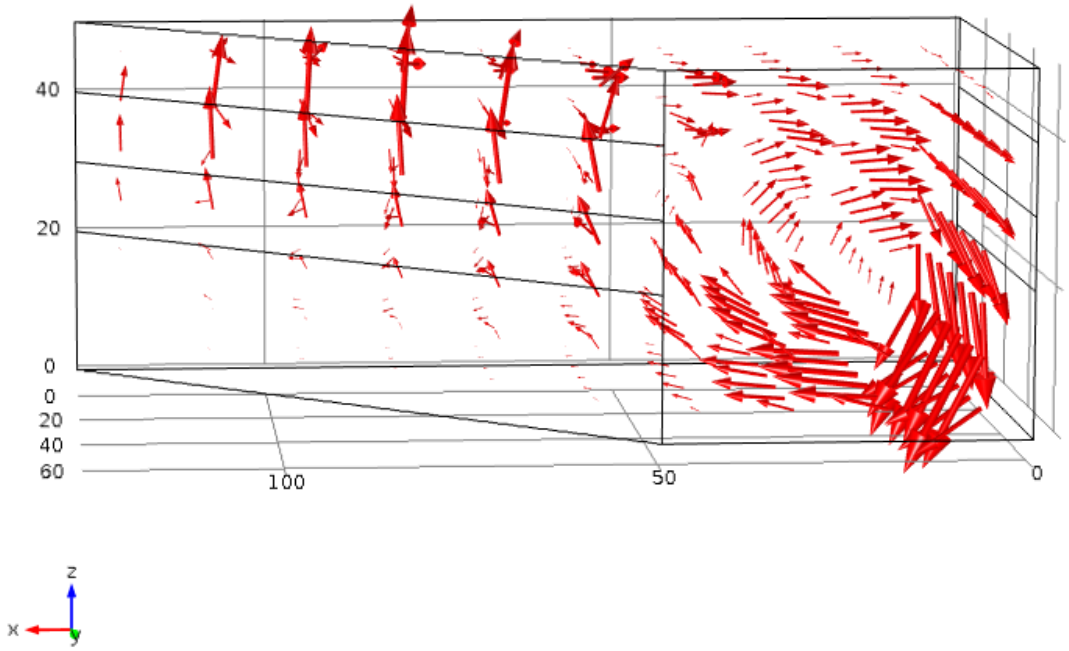

Figure 5.3 Model of the solution flow during electrodeposition with 40 g/L Cu^{2+}, 160 g/L H_2SO_4, 42.9 µg/L thiourea, and 26.4 µg/L glue at 45 °C and t = 100s

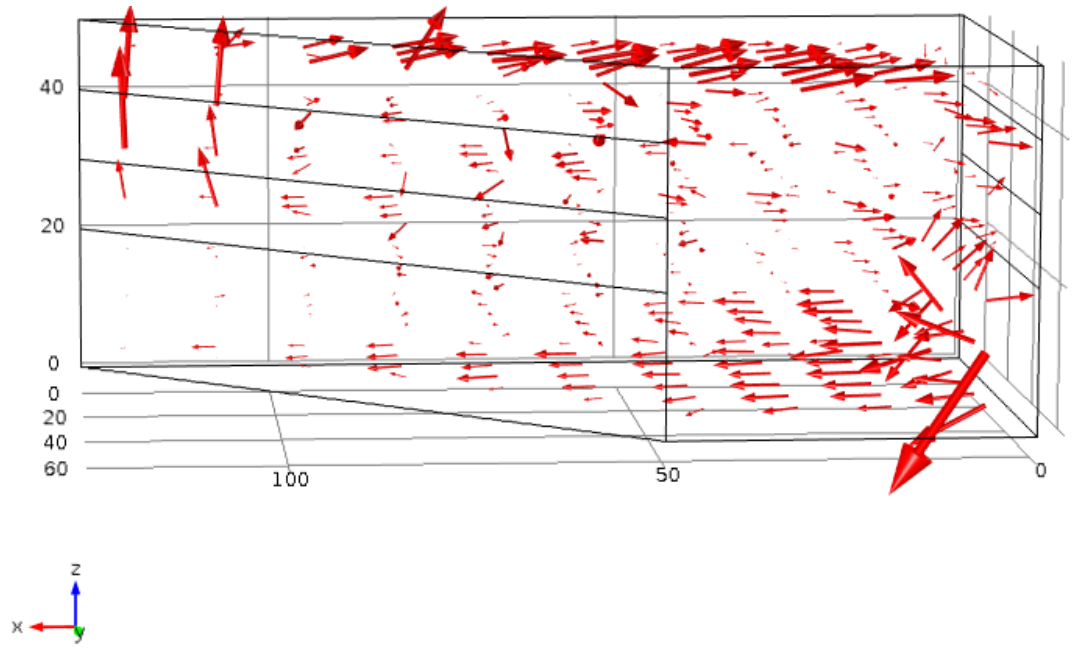

Figure 5.4 Model of the solution flow during electrodeposition with 40 g/L Cu^{2+}, 160 g/L H_2SO_4, 42.9 µg/L thiourea, and 26.4 µg/L glue at 45 °C and t = 14400s

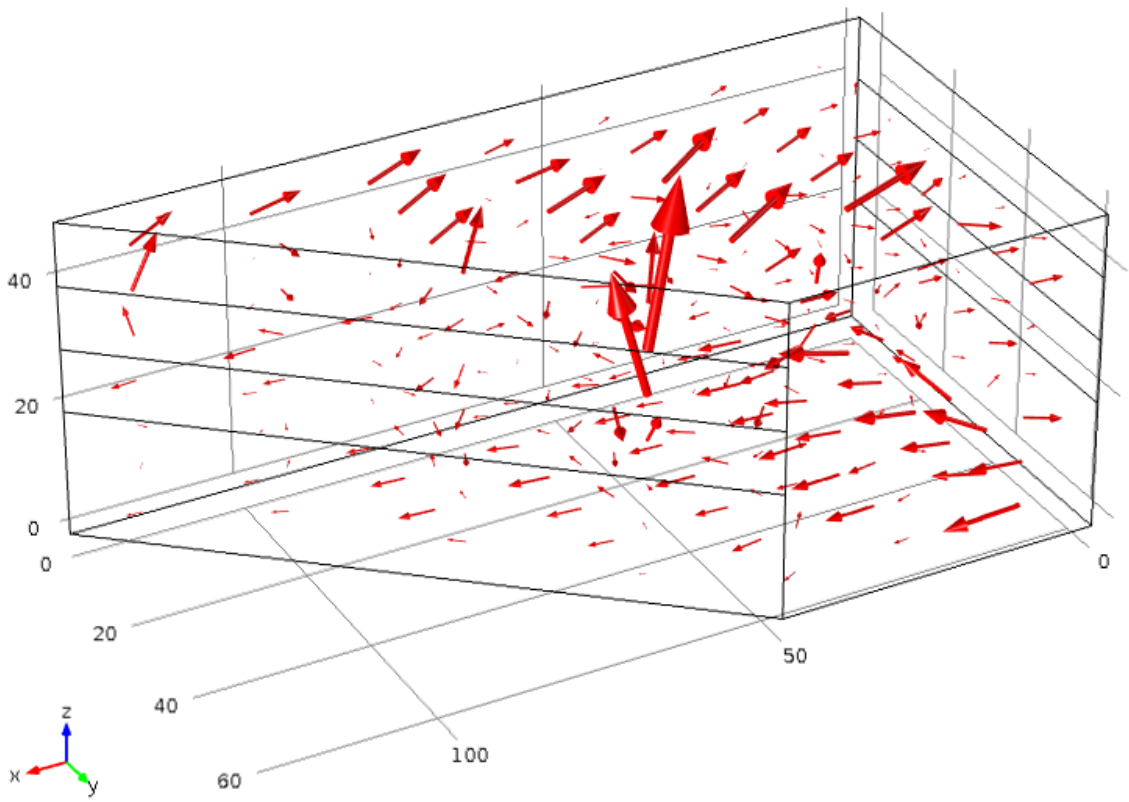

Figure 5.5 Model of the solution flow during electrodeposition with 40 g/L Cu^{2+}, 160 g/L H_2SO_4, 42.9 µg/L thiourea, and 26.4 µg/L glue at 45 °C and t = 14400s

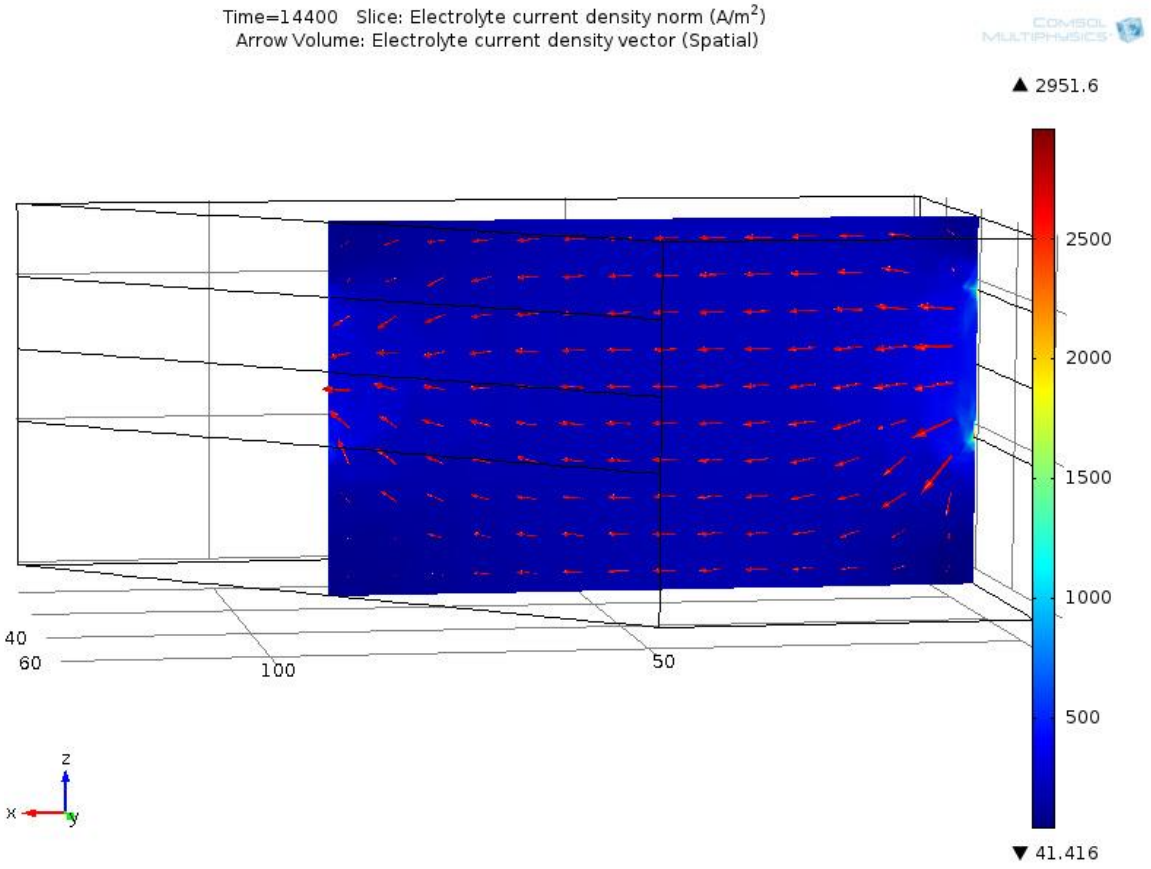

Figure 5.6 Model of the electrical current flow during electrodeposition with 40 g/L Cu^{2+}, 160 g/L H_2SO_4, 42.9 µg/L thiourea, and 26.4 µg/L glue at 45 °C and t = 14400s

5.3 Concentration

The copper concentration profile also behaves as expected; the model shows copper depletion at the surface of the cathode and a buildup of copper at the anode. In Figure 5.7, the effects of the convection flow can be seen as the copper is replenished at the cathode and carried away at the anode. The copper concentration also tends to be higher towards the bottom of the cell.

5.4 Deposit Profile

The deposit distributions from the Hull Cell experiments and their corresponding model results are displayed in Figures 5.8–5.12. The plots show the deposit distribution along the center of the 2-cm strip of plating with the position on the x-axis representing the horizontal location along the cathode beginning at the side of the cathode nearest to the anode.

In Figure 5.8, the measured deposit profile at 30 g/L and 30 °C had significant nodules that distorted the shape of the deposit. A low concentration of copper combined with a low temperature made it difficult for copper ions to migrate to the surface of the cathode, encouraging the growth of any irregular deposit feature that began to form during deposition. The model was not designed to predict nodule growth and therefore predicted a much more uniform deposit.

In Figure 5.9, the measured deposit profile at 30 g/L and 60 °C had a thick growth at the edge nearest to the anode and a linearly decreasing thickness across the cathode. This thick edge buildup was expected and this effect has been documented in literature (*22*). The model predicts a similar thickness at each end of the cathode, but the region

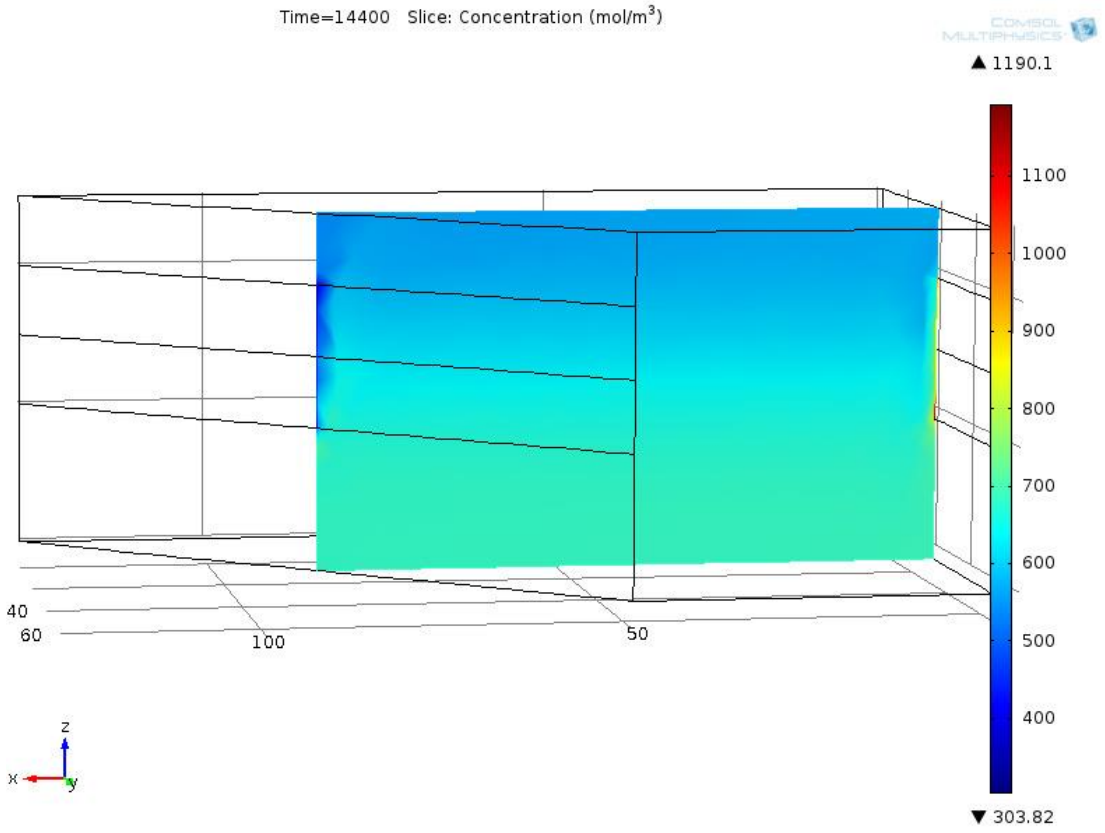

Figure 5.7 Model of the copper concentration in mol/m^3 during electrodeposition with 40 g/L Cu^{2+}, 160 g/L H_2SO_4, 42.9 µg/L thiourea, and 26.4 µg/L glue at 45 °C and t = 14400s

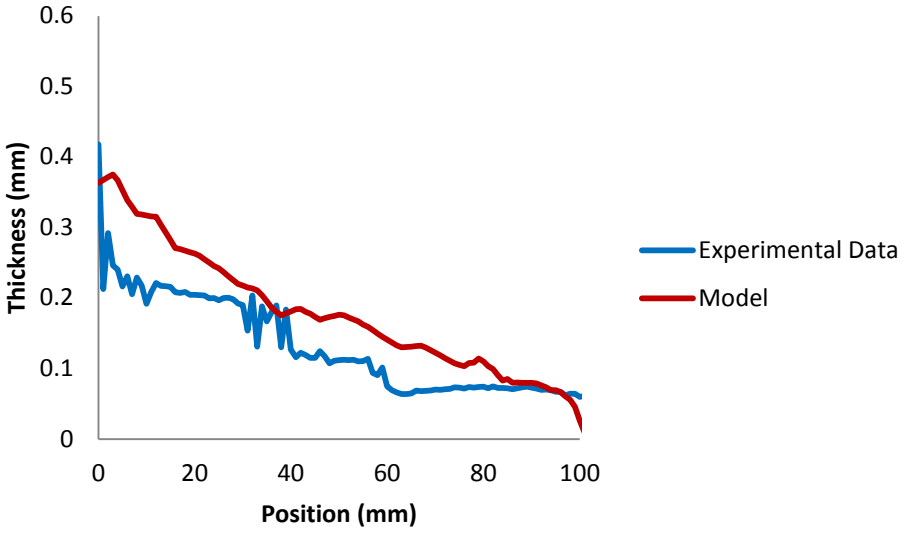

Figure 5.8 Experimental deposit profile and model deposit profile with 30 g/L Cu^{2+}, 160 g/L H_2SO_4, 42.9 µg/L thiourea, and 26.4 µg/L glue at 30 °C and t = 14400s

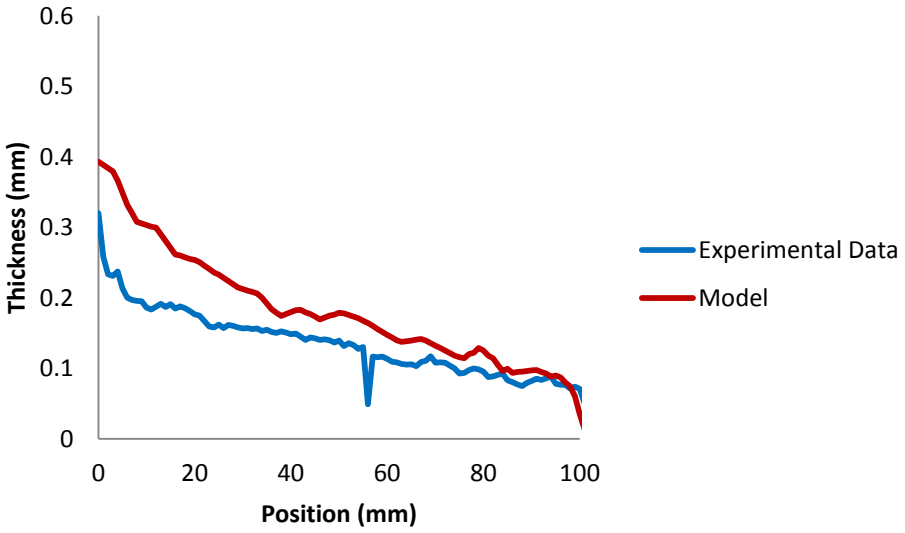

Figure 5.9 Experimental deposit profile and model deposit profile with 30 g/L Cu^{2+}, 160 g/L H_2SO_4, 42.9 µg/L thiourea, and 26.4 µg/L glue at 60 °C and t = 14400s

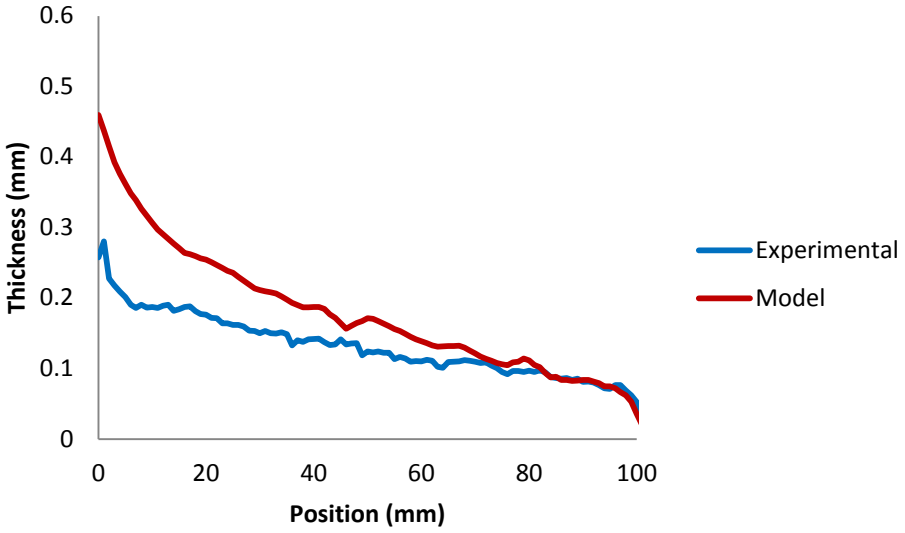

Figure 5.10 Experimental deposit profile and model deposit profile with 40 g/L Cu^{2+}, 160 g/L H_2SO_4, 42.9 µg/L thiourea, and 26.4 µg/L glue at 45 °C and t = 14400s

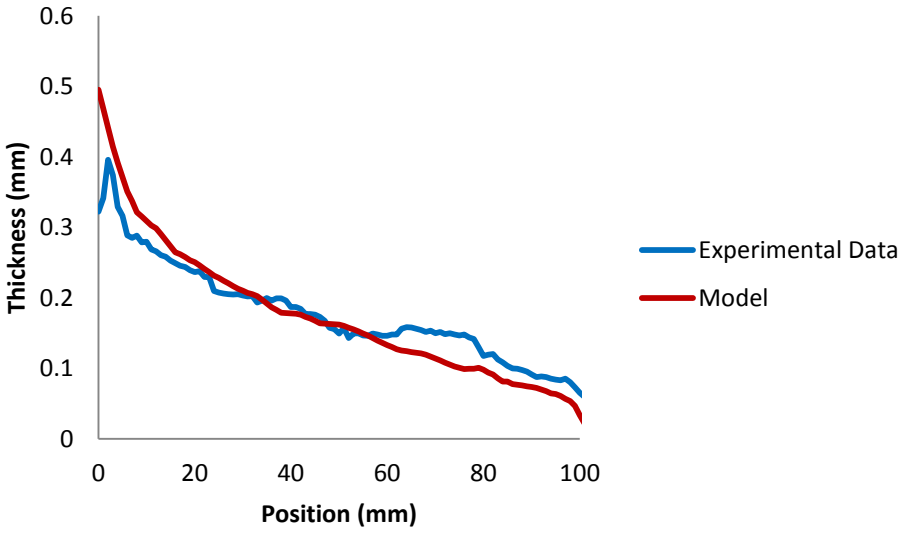

Figure 5.11 Experimental deposit profile and model deposit profile with 50 g/L Cu^{2+}, 160 g/L H_2SO_4, 42.9 µg/L thiourea, and 26.4 µg/L glue at 30 °C and t = 14400s

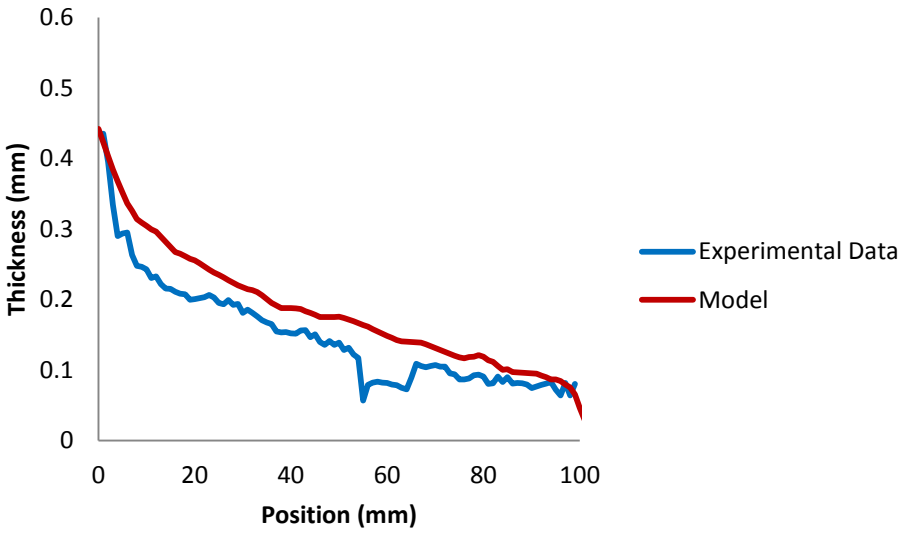

Figure 5.12 Experimental deposit profile and model deposit profile with 50 g/L Cu^{2+}, 160 g/L H_2SO_4, 42.9 µg/L thiourea, and 26.4 µg/L glue at 60 °C and t = 14400s

adjacent to the near edge predicts a much thicker deposit with a shallower slope as the deposit thickness decreases across the cathode.

The measured deposit and model deposit profile at 40 g/L and 45 °C are similar to what was seen at 30 g/L and 60 °C. Multiple experiments were conducted under these conditions and the profile shown in Figure 5.10 is an average profile. The model and experimental results have very similar shapes, but the model predicts a thicker deposit at the near region of the cathode than was seen experimentally.

The experimental results and the model prediction at 50 g/L and 30 °C in Figure 5.11 and at 50 g/L and 60 °C in Figure 5.12 show very similar results and good correlation.

The model was more accurate for solutions containing 50 g/L of copper; under conditions of lower copper concentration, the model predicts a much thicker deposit than is seen experimentally. Significant amounts of copper powder were found in the bottom of the Hull Cell following electrodeposition, indicating that much of the difference between the model and experimental results can be attributed to copper powder generation. Industrial electrolytic copper powder generation is typically generated with the conditions shown in Table 5.1 (*23*).

Most of the conditions of the experiments at 30 g/L fall within the ranges commonly seen in electrolytic copper powder production. The average cathodic current density was 400 A/m^2, but the current density at the region of the cathode closest to the anode exceeded 600 A/m^2 and, thus, fall within the range of current densities used for copper powder production.

Table 5.1

Typical Operating Conditions for Copper Powder Production

Parameter	Range of Values
Copper Concentration	30 g/L
H_2SO_4 Concentration	150–250 g/L
Anodic Current Density	300–600 A/m2
Cathodic Current Density	600–4000 A/m2
Temperature	40–60 °C

5.5 Hull Cell Comparison

Table 5.2 contains a summary of the Hull Cell results, where the deposit ratio is the ratio of the average deposit thickness on half of the cathode closest to the anode divided by the average deposit thickness on half of the cathode furthest from the anode. The average percent error is the average percent difference between the model prediction and the experimental results.

Plots of the main effects and interactions for the Hull Cell experiments and model are shown in Figures 5.13–5.18. Contour and 3-D surface plots are shown in Figures 5.19–5.24.

The model and experimental results have similar deposit profiles, but the effects of temperature and concentration on the deposit ratios do not agree. The experimental results showed more uneven deposition with either high concentration and high temperature or low concentration and low temperature, whereas the model predicted the most uneven deposit under conditions of high concentration and low temperature.

5.6 Current Efficiency

For a sample plated at 1500 mA for 30 seconds followed by 800 mA for 4 hours, the theoretical deposit weight calculated from eq 5.1 is 3.809 g. When 800 mA is applied to the cell, the average current density is 400 A/m^2.

$$\frac{i * t * MW}{F * z} \qquad \textbf{(5.1)}$$

Table 5.2

Summary of Hull Cell Results

Temperature (C)	Concentration (g/L)	Deposit Ratio	Model Deposit Ratio	Model to Experimental Ratio	Average % Error
30	30	2.482874	2.320283	0.934515	33.1
30	50	1.859775	2.49298	1.340474	19.7
45	40	1.754666	2.303369	1.312711	31.2
60	30	1.805198	2.065402	1.144142	26.8
60	50	2.349941	2.119184	0.901803	24.2

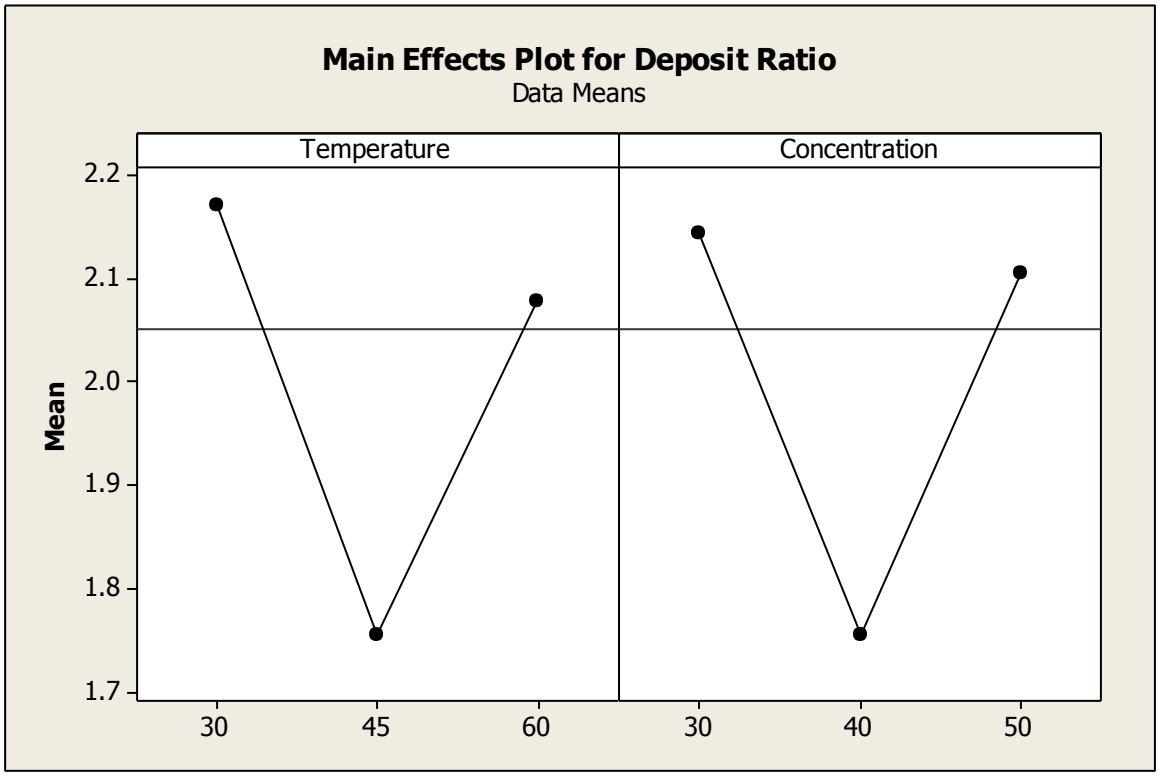

Figure 5.13 Plot of the effects of temperature and concentration on the deposit ratio with 30 to 60 g/L Cu^{2+}, 160 g/L H_2SO_4, 42.9 µg/L thiourea, and 26.4 µg/L glue at 30 to 60 °C and a current density of 400A/m^2. See Table 5.2 for additional detail on the concentrations and temperatures.

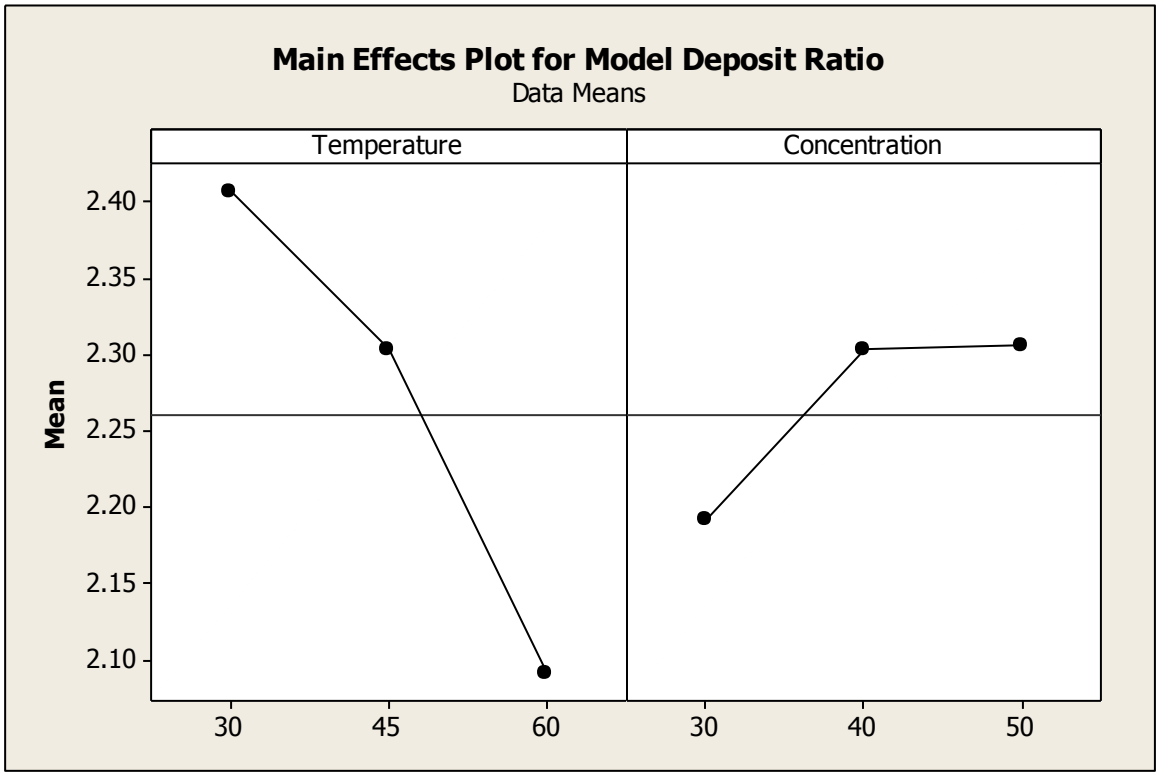

Figure 5.14 Plot of the effects of temperature and concentration on the model deposit ratio with 30 to 60 g/L Cu^{2+}, 160 g/L H_2SO_4, 42.9 µg/L thiourea, and 26.4 µg/L glue at 30 to 60 °C and a current density of 400A/m^2. See Table 5.2 for additional detail on the concentrations and temperatures.

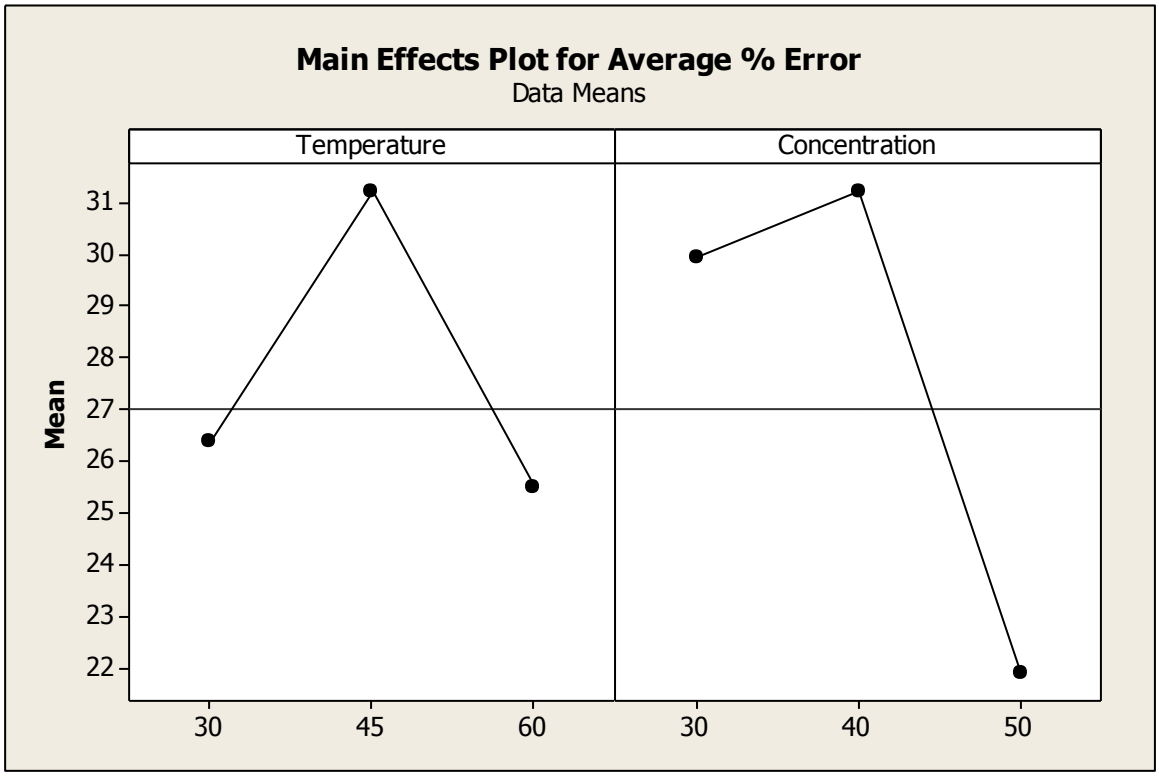

Figure 5.15 Plot of the effects of temperature and concentration on the average percent error between the experimental and model deposit thickness with 30 to 60 g/L Cu^{2+}, 160 g/L H_2SO_4, 42.9 µg/L thiourea, and 26.4 µg/L glue at 30 to 60 °C and a current density of 400A/m^2. See Table 5.2 for additional detail on the concentrations and temperatures.

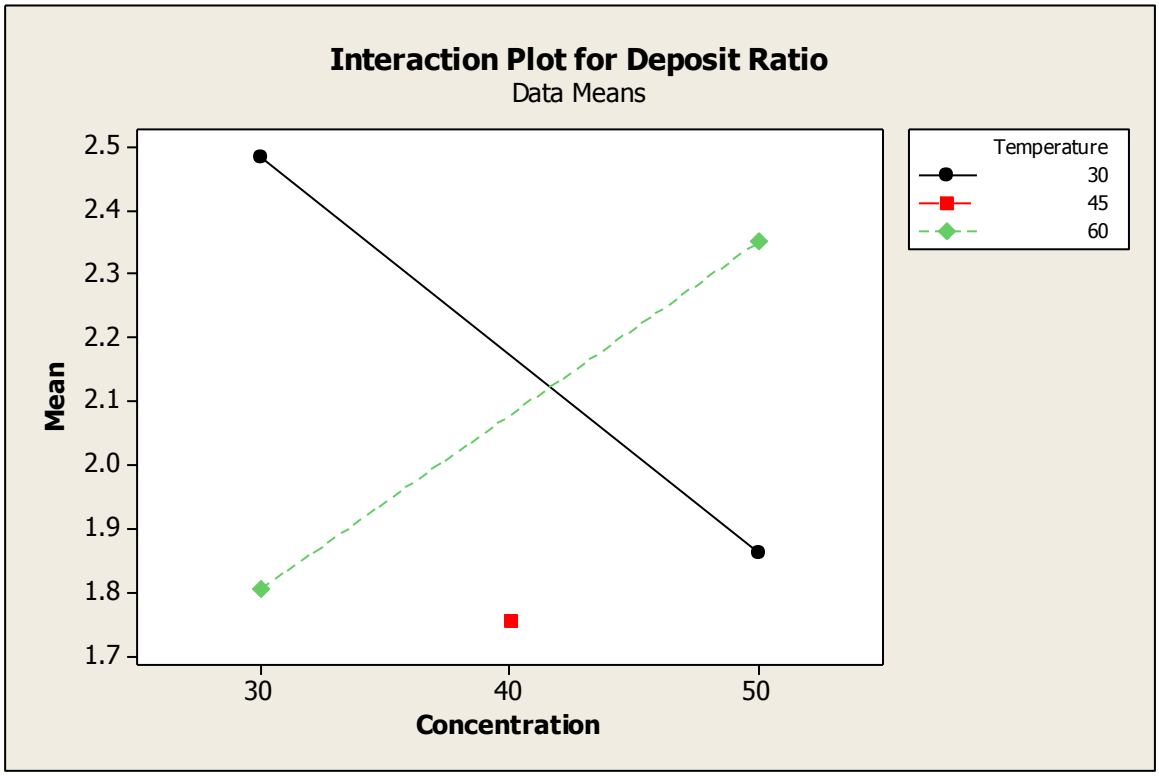

Figure 5.16 Plot of the interaction of temperature and concentration on the deposit ratio with 30 to 60 g/L Cu^{2+}, 160 g/L H_2SO_4, 42.9 µg/L thiourea, and 26.4 µg/L glue at 30 to 60 °C and a current density of 400A/m^2. See Table 5.2 for additional detail on the concentrations and temperatures.

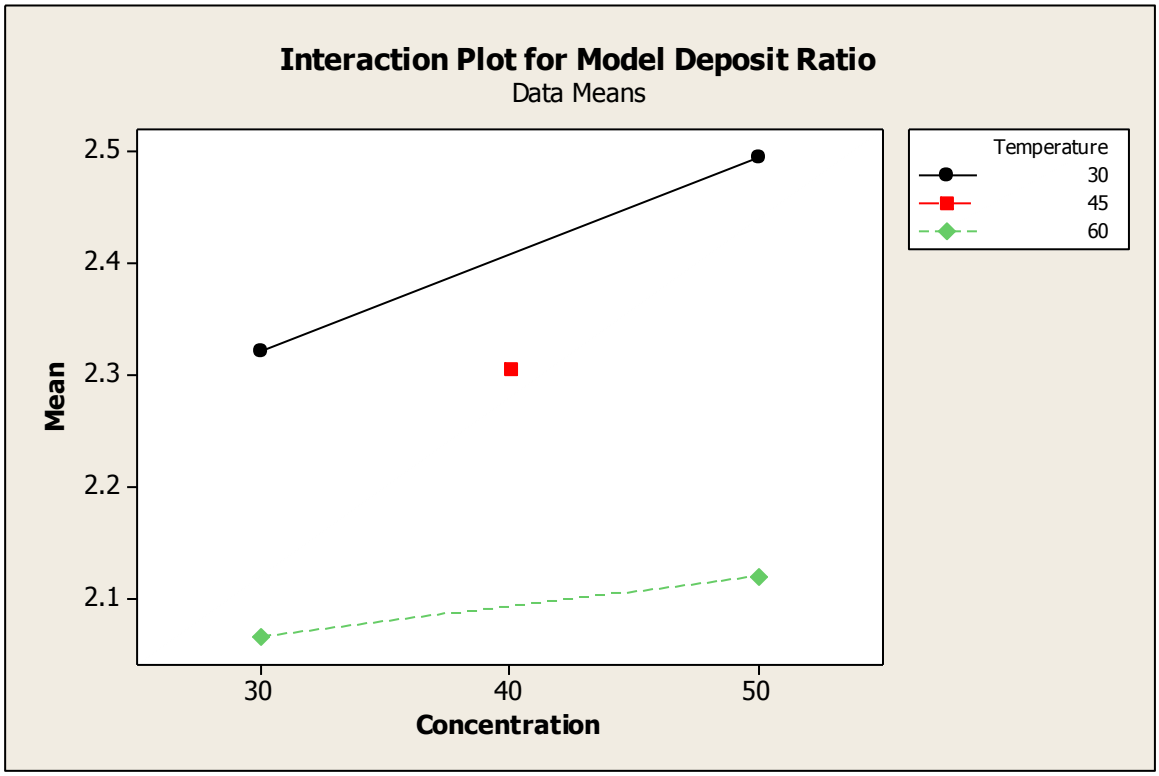

Figure 5.17 Plot of the interaction of temperature and concentration on the model deposit ratio with 30 to 60 g/L Cu^{2+}, 160 g/L H_2SO_4, 42.9 µg/L thiourea, and 26.4 µg/L glue at 30 to 60 °C and a current density of 400A/m^2. See Table 5.2 for additional detail on the concentrations and temperatures.

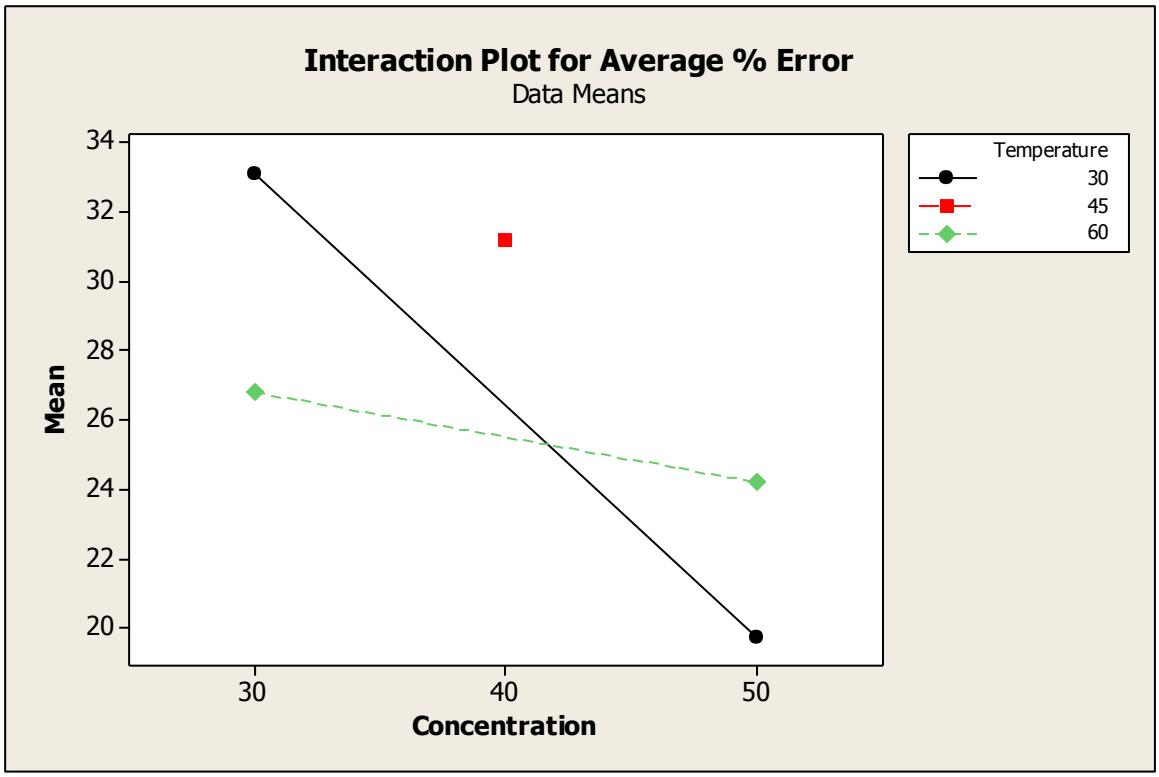

Figure 5.18 Plot of the interaction of temperature and concentration on the average percent error between the experimental and model deposit thickness with 30 to 60 g/L Cu^{2+}, 160 g/L H_2SO_4, 42.9 µg/L thiourea, and 26.4 µg/L glue at 30 to 60 °C and a current density of 400A/m^2. See Table 5.2 for additional detail on the concentrations and temperatures.

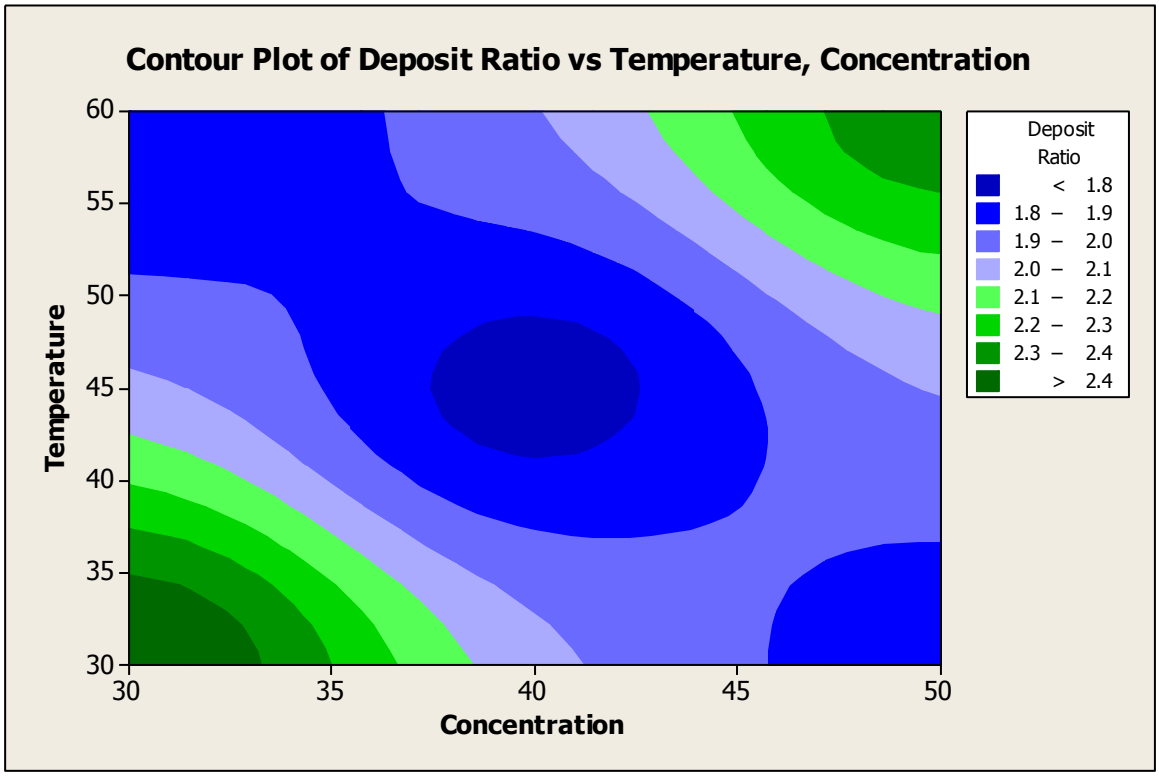

Figure 5.19 Contour plot of the effect of temperature and concentration on the deposit ratio with 30 to 60 g/L Cu^{2+}, 160 g/L H_2SO_4, 42.9 µg/L thiourea, and 26.4 µg/L glue at 30 to 60 °C and a current density of 400A/m^2. See Table 5.2 for additional detail on the concentrations and temperatures.

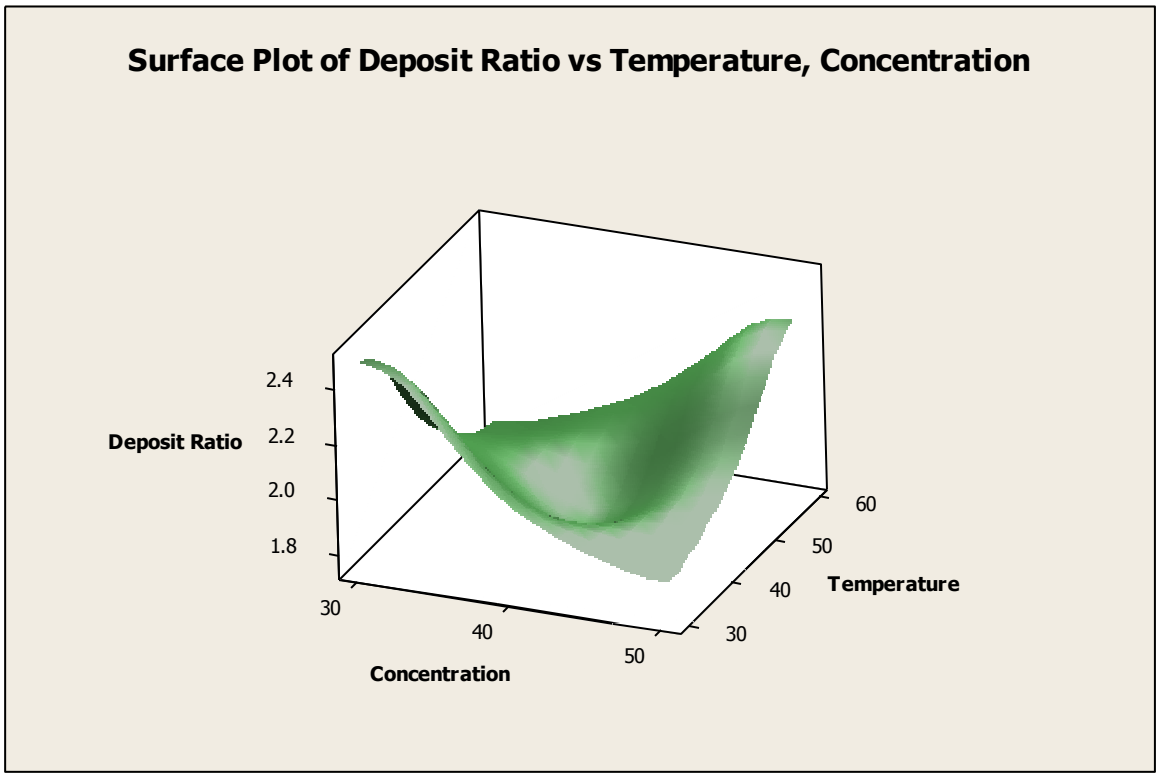

Figure 5.20 3-D surface plot of the effect of temperature and concentration on the deposit ratio with 30 to 60 g/L Cu^{2+}, 160 g/L H_2SO_4, 42.9 µg/L thiourea, and 26.4 µg/L glue at 30 to 60 °C and a current density of 400A/m^2. See Table 5.2 for additional detail on the concentrations and temperatures.

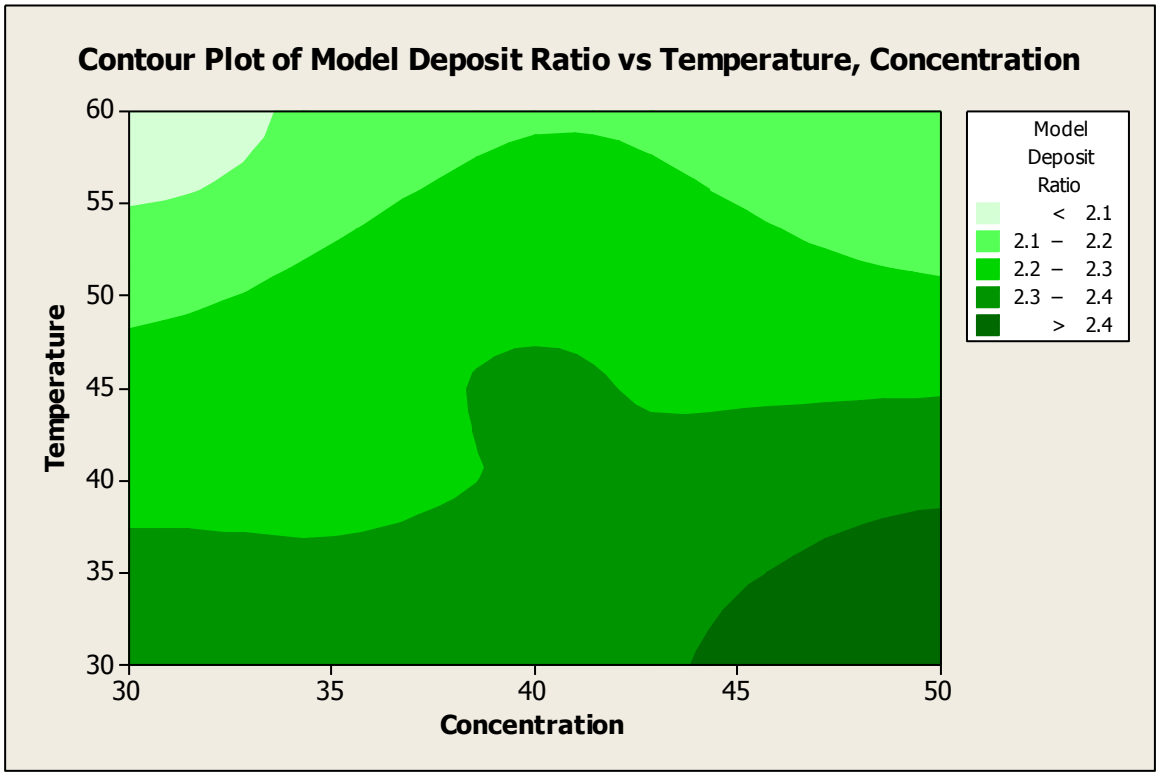

Figure 5.21 Contour plot of the effect of temperature and concentration on the model deposit ratio with 30 to 60 g/L Cu^{2+}, 160 g/L H_2SO_4, 42.9 µg/L thiourea, and 26.4 µg/L glue at 30 to 60 °C and a current density of 400A/m^2. See Table 5.2 for additional detail on the concentrations and temperatures.

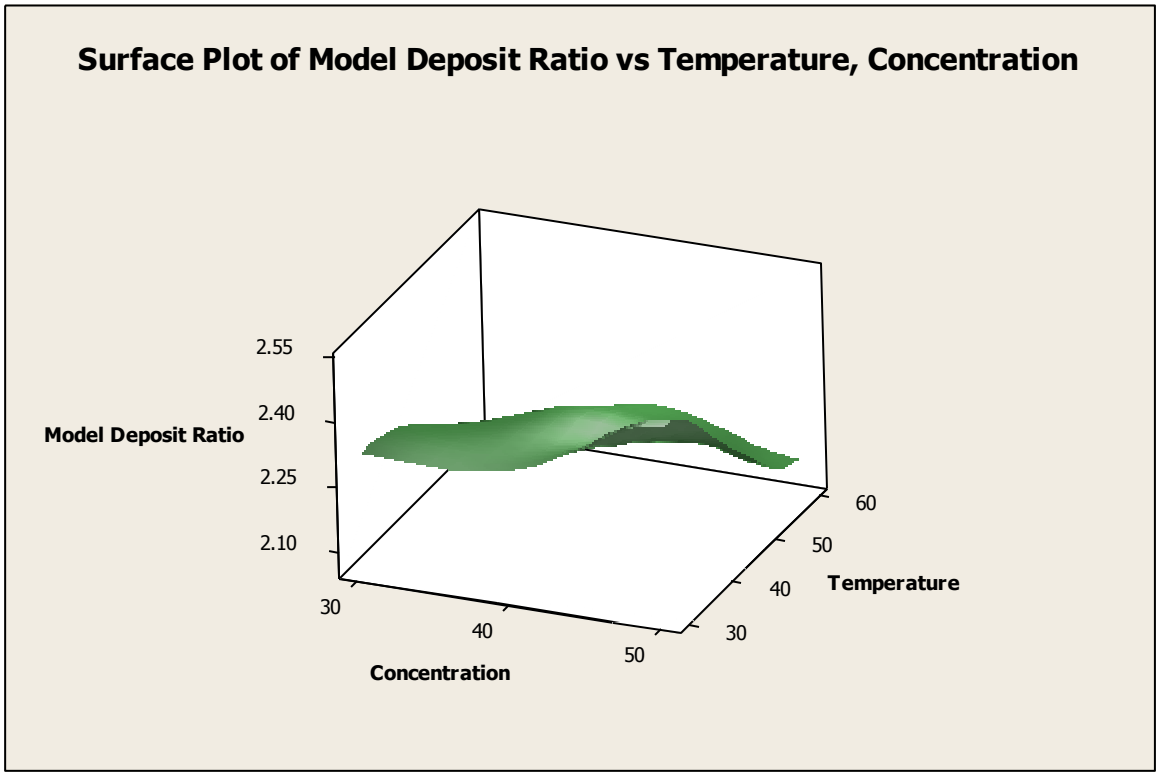

Figure 5.22 3-D surface plot of the effect of temperature and concentration on the model deposit ratio with 30 to 60 g/L Cu^{2+}, 160 g/L H_2SO_4, 42.9 µg/L thiourea, and 26.4 µg/L glue at 30 to 60 °C and a current density of 400A/m^2. See Table 5.2 for additional detail on the concentrations and temperatures.

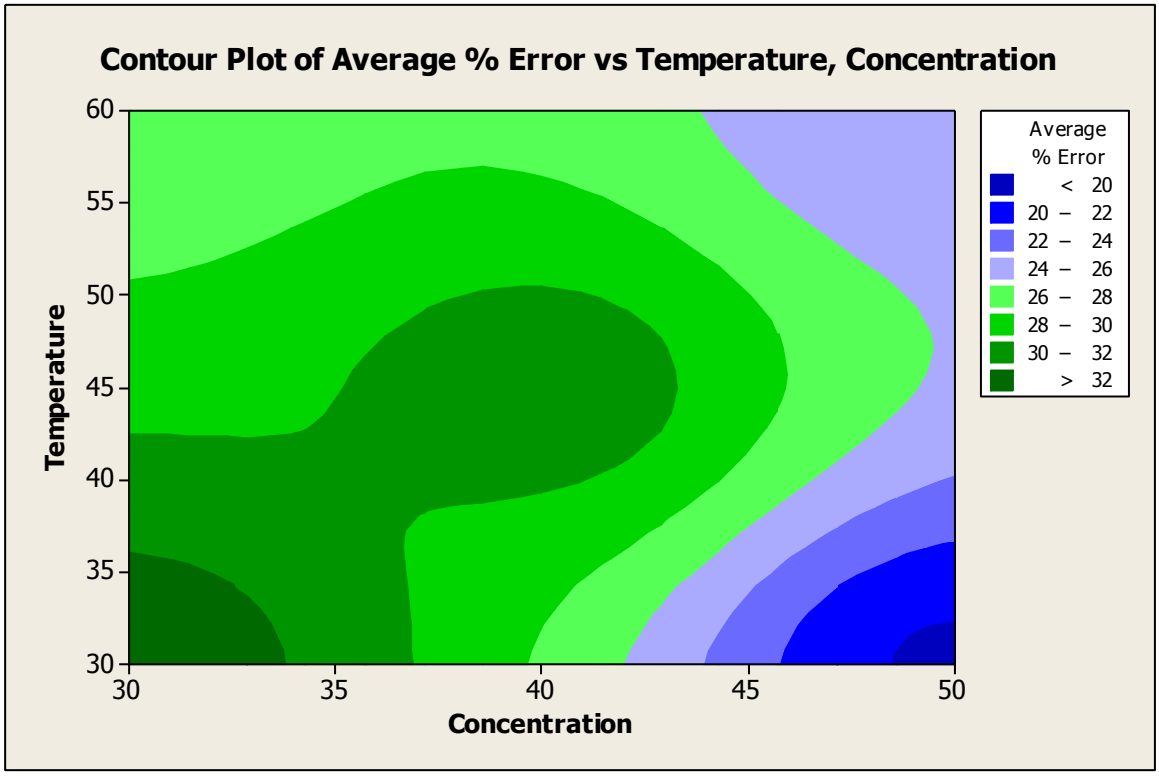

Figure 5.23 Contour plot of the effect of temperature and concentration on the average percent error between the experimental and model deposit thickness with 30 to 60 g/L Cu^{2+}, 160 g/L H_2SO_4, 42.9 µg/L thiourea, and 26.4 µg/L glue at 30 to 60 °C and a current density of 400A/m^2. See Table 5.2 for additional detail on the concentrations and temperatures.

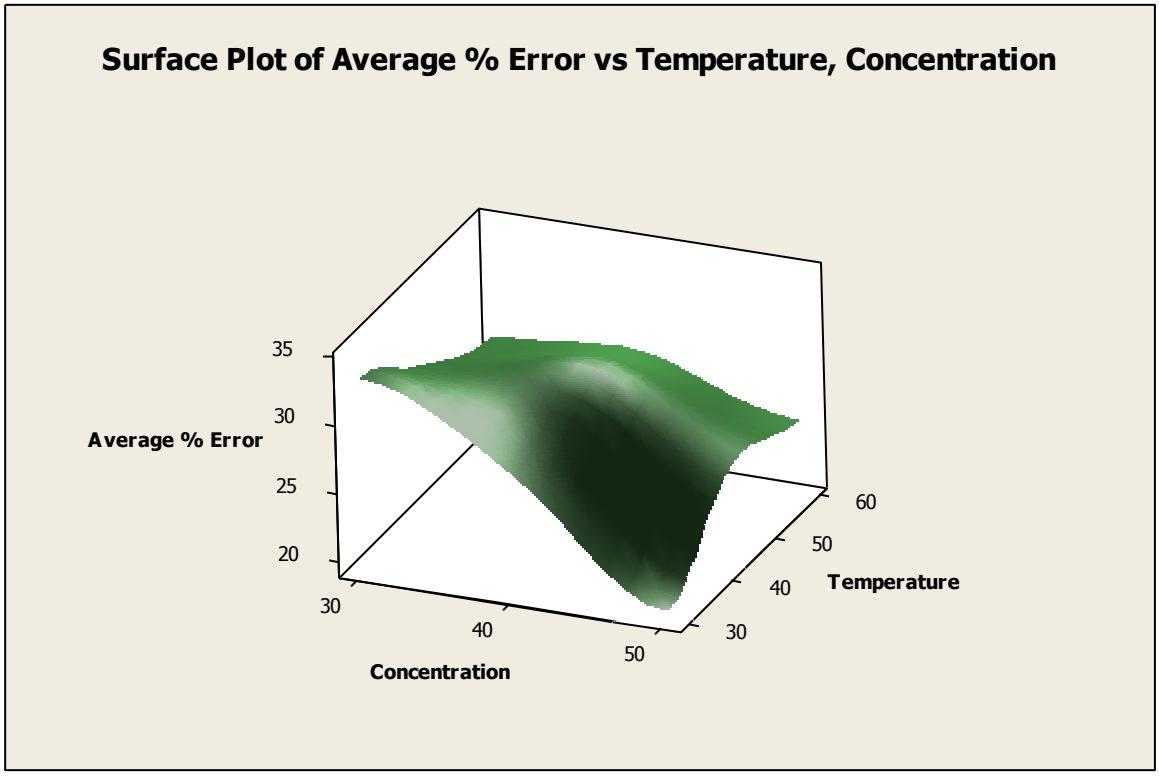

Figure 5.24 3-D surface plot of the effect of temperature and concentration on the average percent error between the experimental and model deposit thickness with 30 to 60 g/L Cu^{2+}, 160 g/L H_2SO_4, 42.9 µg/L thiourea, and 26.4 µg/L glue at 30 to 60 °C and a current density of 400A/m^2. See Table 5.2 for additional detail on the concentrations and temperatures.

The average deposit weight observed was significantly lower than the theoretical value, with an average deposit weight 66.8% of the theoretical weight. Deposit weights of each sample are shown in Table 5.3.

Table 5.3

Experimental Conditions of Hull Cell Experiments

Run Number	Concentration	Temperature	Deposit Weight	Efficiency
1	30	50	2.5970	68.2%
2	45	40	2.4739	65.0%
3	60	30	2.5522	67.0%
4	45	40	2.5387	66.7%
5	60	50	2.5534	67.0%
6	45	40	2.6184	68.7%
7	45	40	2.5058	65.8%
8	45	40	2.5123	66.0%
9	30	30	2.5561	67.1%

CHAPTER 6

SHAPED CATHODES RESULTS AND DISCUSSION

Four geometries were modeled and validated using experimental data: a 2-inch angle, a 0.75-inch angle, a 2-inch diameter pipe, and a 0.75-inch diameter pipe referred to as Large Angle, Small Angle, Large Pipe, and Small Pipe, respectively. The geometries of the shaped cathodes were described in more detail in Section 3.2.

6.1 Solution Flow

In the shaped cathode models, the flow reached a steady state, unlike the solution flow in the Hull Cell. This resulted in a more uniform solution flow that solved more rapidly than the Hull Cell models. Figures 6.1–6.4 show the velocity profile of the solutions in each of the shaped cathodes.

6.2 Concentration

The concentration gradients in the solutions are shown in Figures 6.5–6.12.

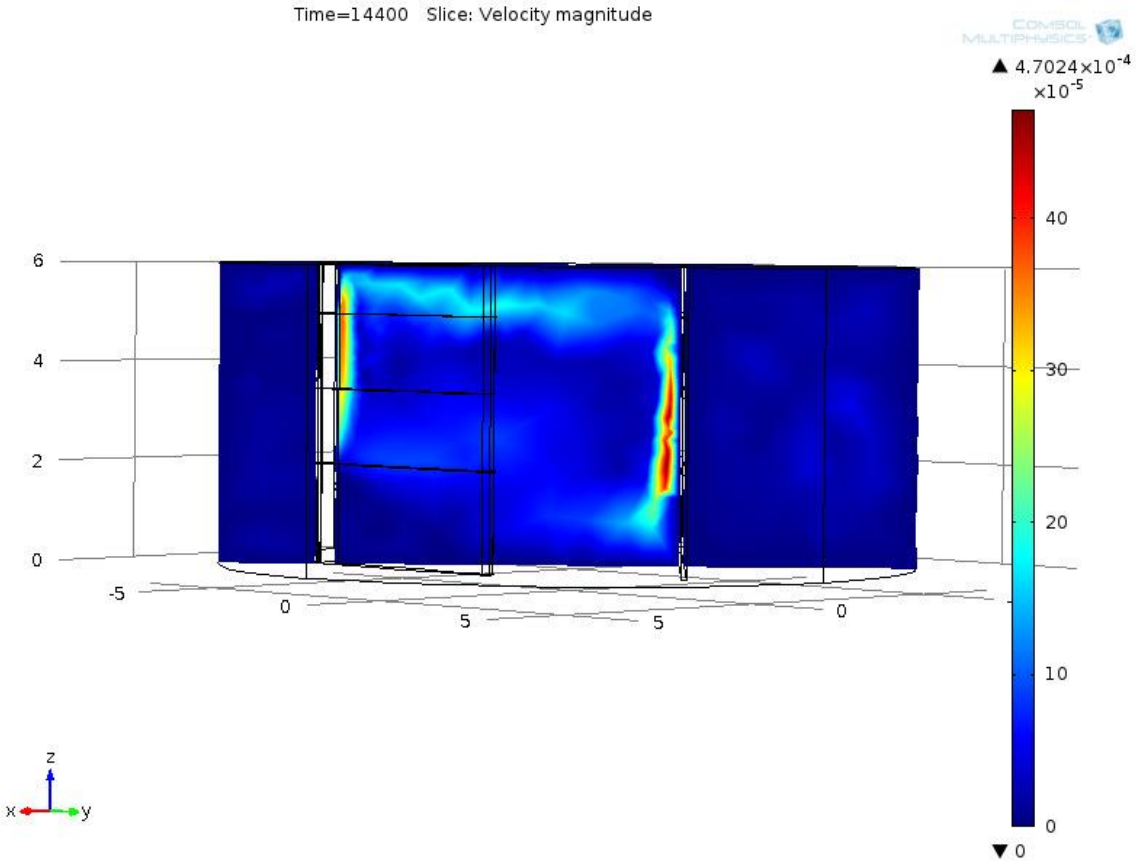

Figure 6.1 Solution flow in the Large Angle model during electrodeposition with 40 g/L Cu^{2+}, 160 g/L H_2SO_4, 42.9 µg/L thiourea, and 26.4 µg/L glue at 45 °C and t = 14400s

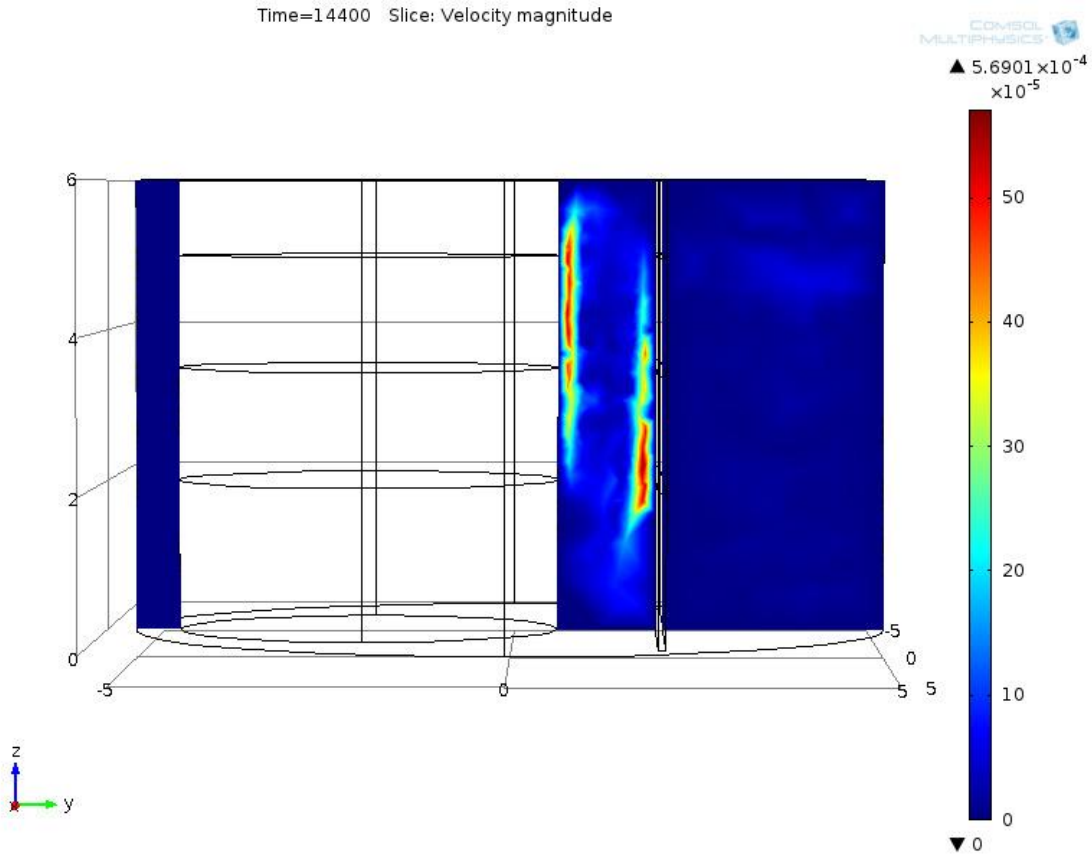

Figure 6.2 Solution flow in the Large Pipe model during electrodeposition with 40 g/L Cu^{2+}, 160 g/L H_2SO_4, 42.9 µg/L thiourea, and 26.4 µg/L glue at 45 °C and t = 14400s

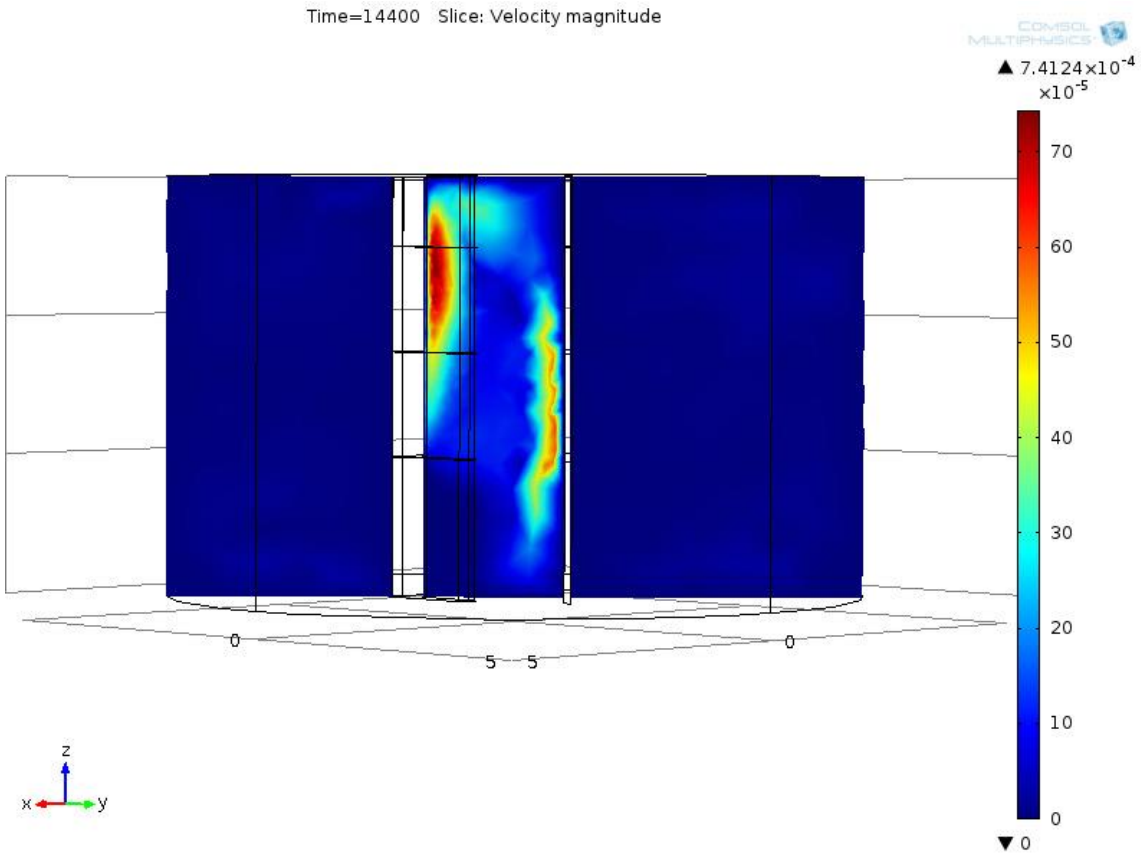

Figure 6.3 Solution flow in the Small Angle model during electrodeposition with 40 g/L Cu^{2+}, 160 g/L H_2SO_4, 42.9 µg/L thiourea, and 26.4 µg/L glue at 45 °C and t = 14400s

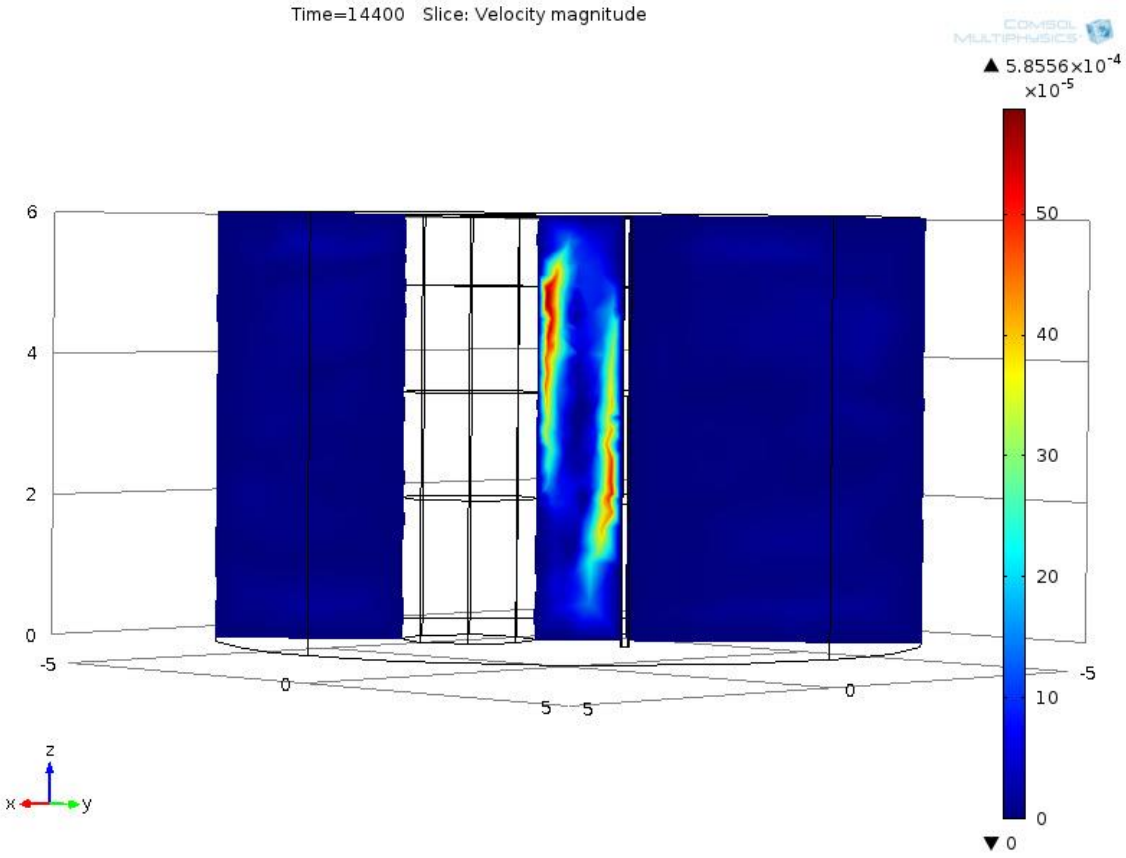

Figure 6.4 Solution flow in the Small Pipe model during electrodeposition with 40 g/L Cu^{2+}, 160 g/L H_2SO_4, 42.9 µg/L thiourea, and 26.4 µg/L glue at 45 °C and t = 14400s

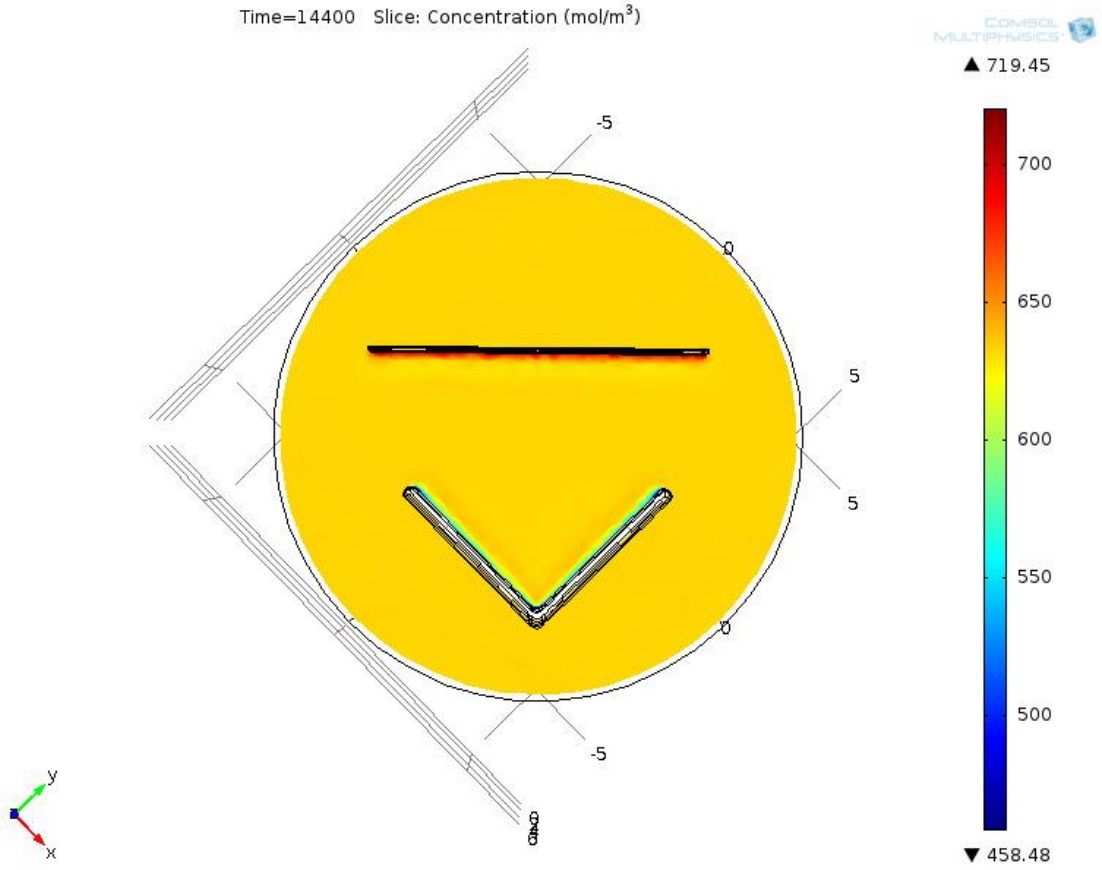

Figure 6.5 Concentration of Cu^{2+} in the Large Angle model during electrodeposition with 40 g/L Cu^{2+}, 160 g/L H_2SO_4, 42.9 µg/L thiourea, and 26.4 µg/L glue at 45 °C and t = 14400s

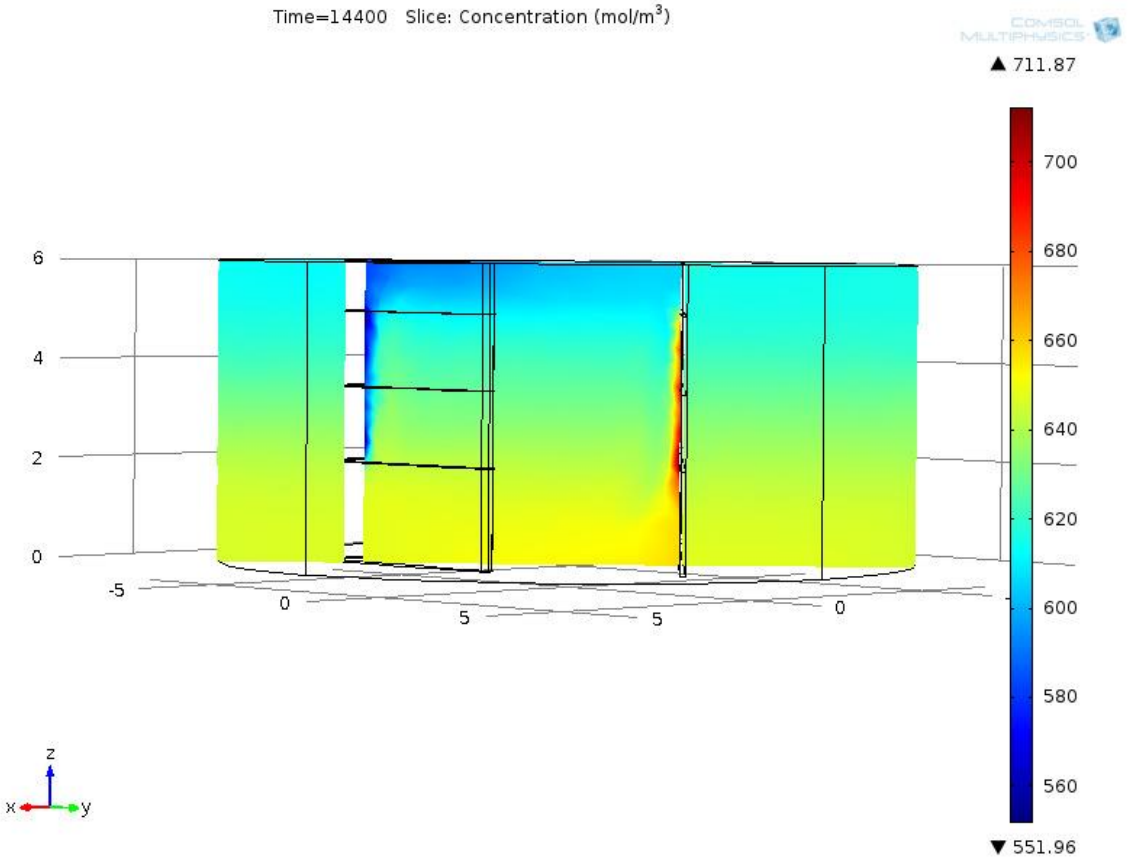

Figure 6.6 Concentration of Cu^{2+} in the Large Angle model during electrodeposition with 40 g/L Cu^{2+}, 160 g/L H_2SO_4, 42.9 µg/L thiourea, and 26.4 µg/L glue at 45 °C and t = 14400s

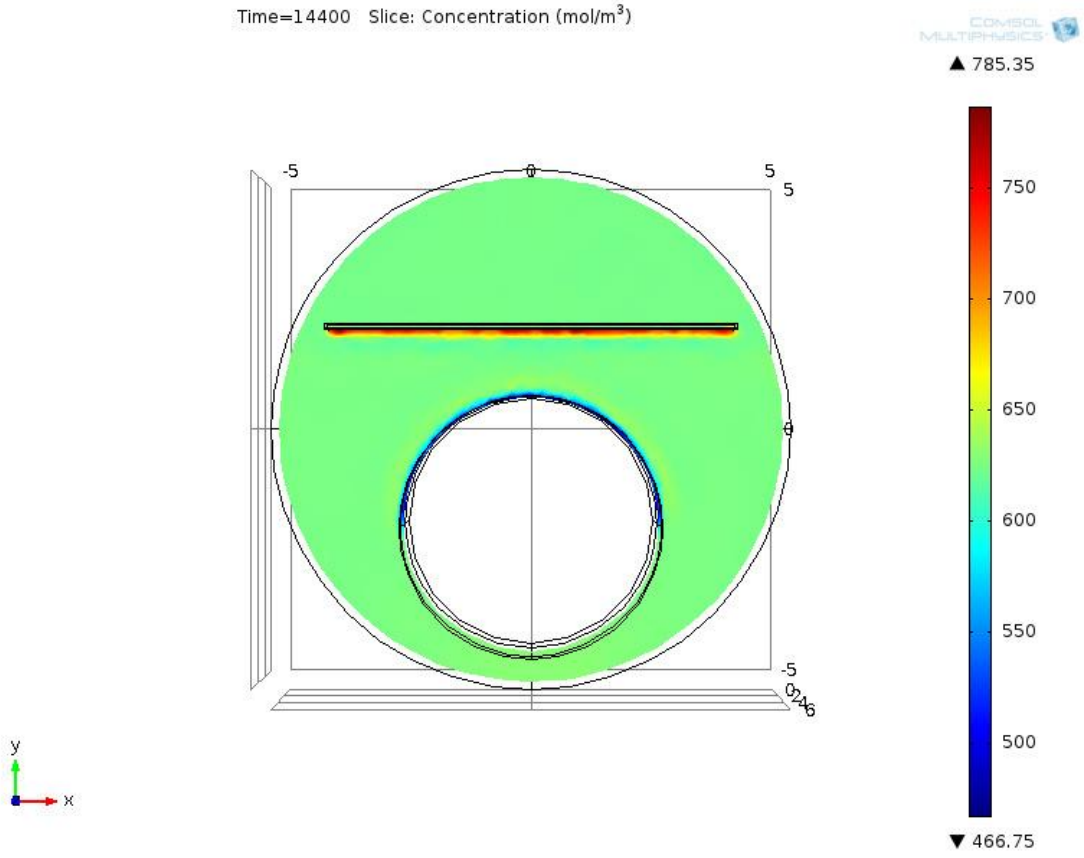

Figure 6.7 Concentration of Cu^{2+} in the Large Pipe model during electrodeposition with 40 g/L Cu^{2+}, 160 g/L H_2SO_4, 42.9 µg/L thiourea, and 26.4 µg/L glue at 45 °C and t = 14400s

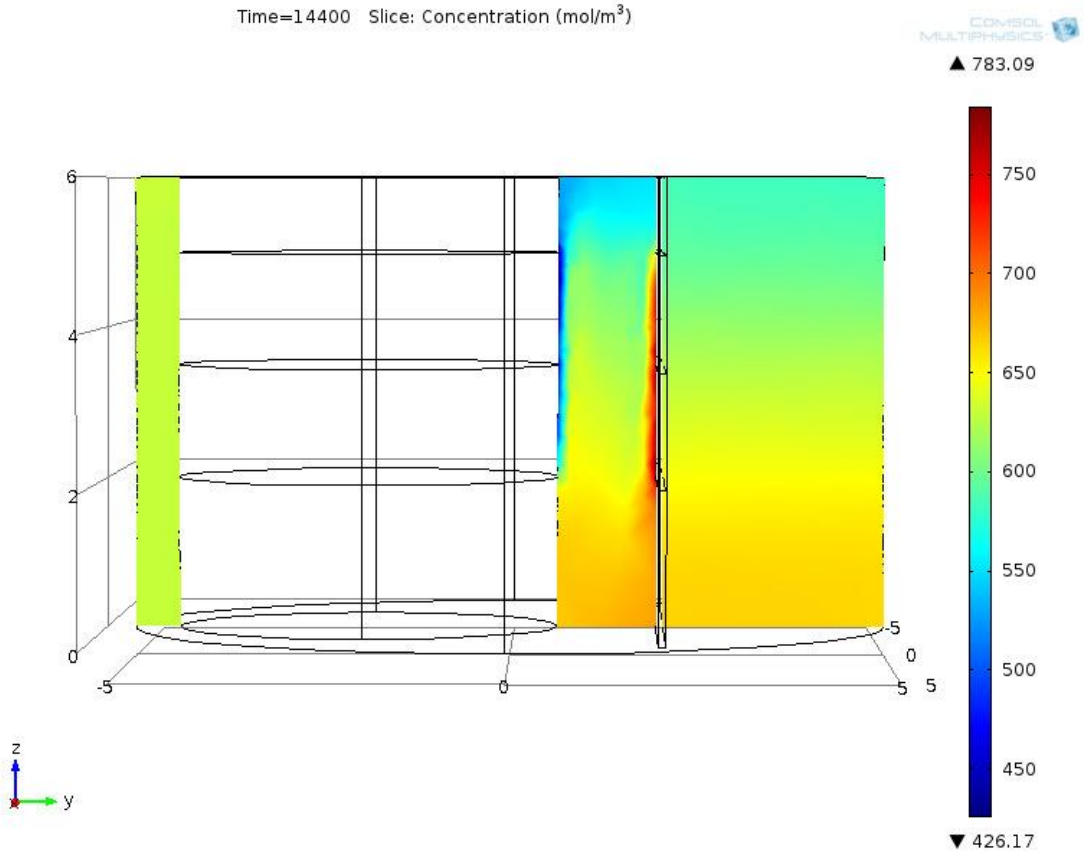

Figure 6.8 Concentration of Cu^{2+} in the Large Pipe model during electrodeposition with 40 g/L Cu^{2+}, 160 g/L H_2SO_4, 42.9 µg/L thiourea, and 26.4 µg/L glue at 45 °C and t = 14400s

Figure 6.9 Concentration of Cu^{2+} in the Small Angle model during electrodeposition with 40 g/L Cu^{2+}, 160 g/L H_2SO_4, 42.9 µg/L thiourea, and 26.4 µg/L glue at 45 °C and t = 14400s

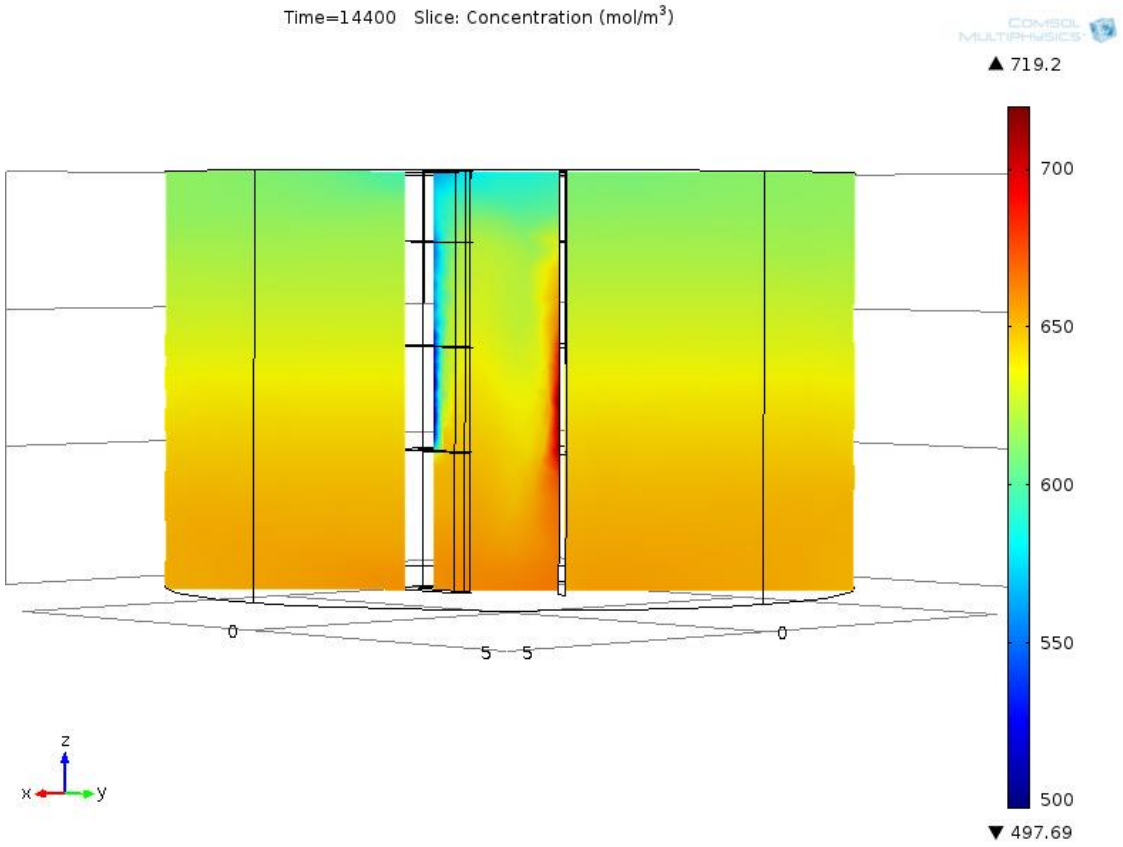

Figure 6.10 Concentration of Cu^{2+} in the Small Angle model during electrodeposition with 40 g/L Cu^{2+}, 160 g/L H_2SO_4, 42.9 µg/L thiourea, and 26.4 µg/L glue at 45 °C and t = 14400s

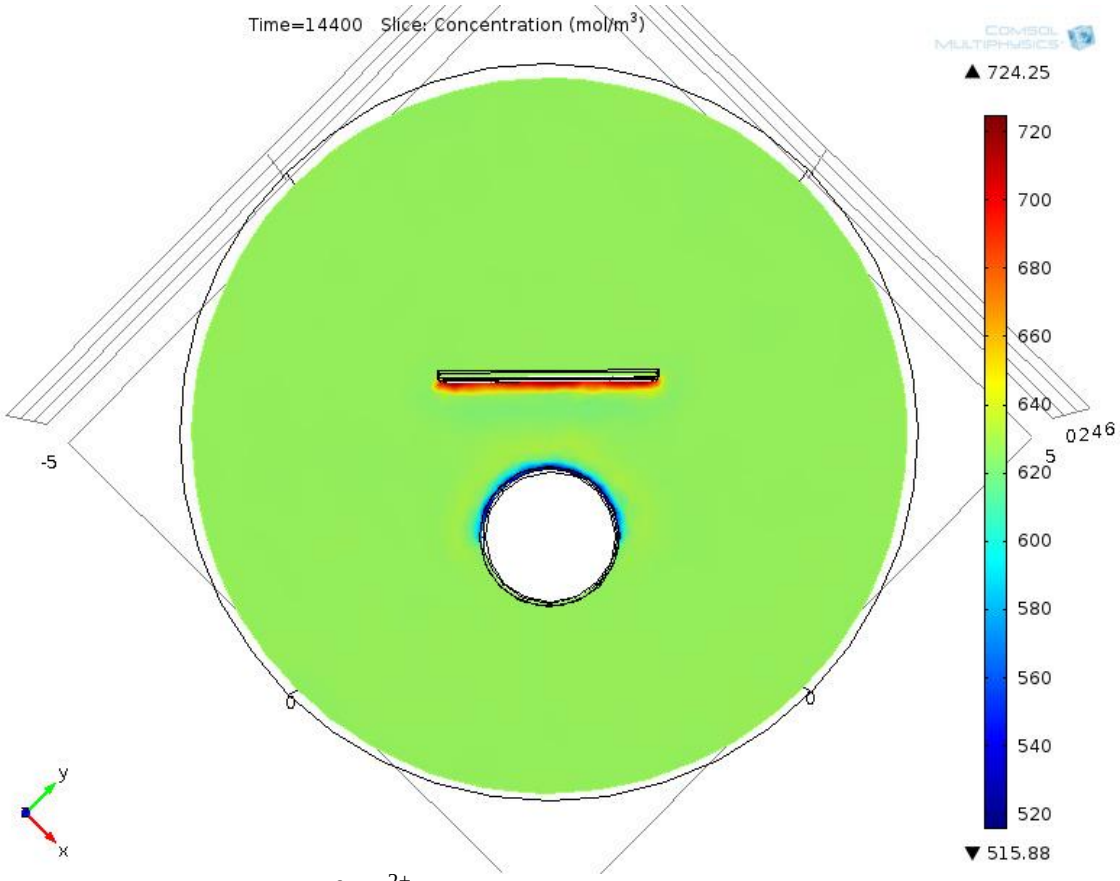

Figure 6.11 Concentration of Cu^{2+} in the Small Pipe model during electrodeposition with 40 g/L Cu^{2+}, 160 g/L H_2SO_4, 42.9 µg/L thiourea, and 26.4 µg/L glue at 45 °C and t = 14400s

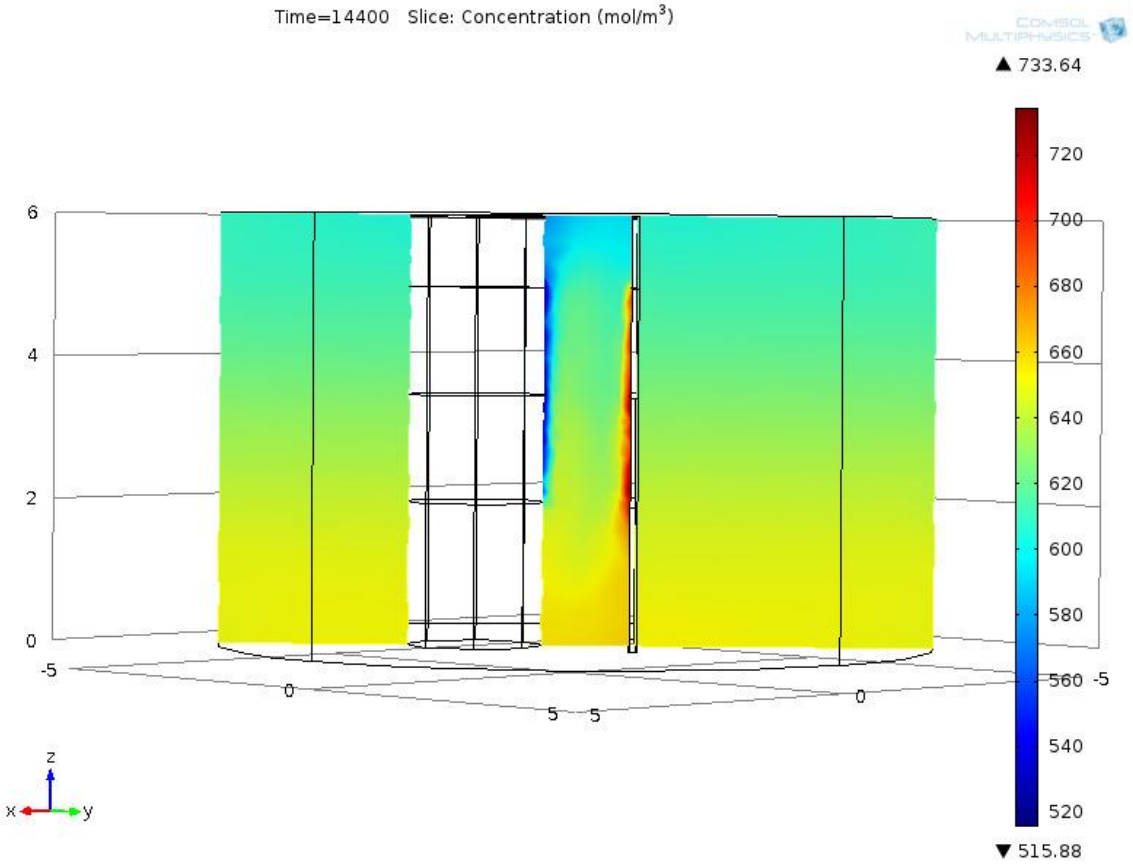

Figure 6.12 Concentration of Cu^{2+} in the Small Pipe model during electrodeposition with 40 g/L Cu^{2+}, 160 g/L H_2SO_4, 42.9 µg/L thiourea, and 26.4 µg/L glue at 45 °C and t = 14400s

6.3 Deposit Profile

The experimental and model deposit distributions are shown in Figures 6.13–6.16. The large pipe model and the experimental data show very good correlation, even at the edges of the deposit (Figure 6.13).

The small pipe model predicted a fairly uniform deposit with a thicker deposit at the edges and the area closest to the anode. The experimental deposit was almost completely flat with surface roughness exceeding the magnitude of any deposit features from the geometry (Figure 6.14).

The large angle deposit distributions correlate very well throughout most of the deposit; however, the model predicts a much larger buildup at the edges. After each run there was copper powder present in the bottom of the cell due to the generation of electrolytic copper powder at the edges of the cathode (Figure 6.15).

The small angle measured deposit was fairly flat with minimal thickness increases away from the center of the cathode. The model predicted a much larger increase in thickness everywhere along the cathode except the center (Figure 6.16).

6.4 Shaped Cathode Comparison

The deposit ratios from the shaped cathode experiments are shown in Table 6.1. In this study, deposit ratio is defined as the ratio of the thickness of the half of the cathode closest to the anode to the thickness of the half of the cathode furthest from the anode. The max/min ratio is the ratio of the thickest deposit feature to the thinnest deposit feature. The linear ratio is the ratio of the distance between the half of the cathode furthest from the anode and the half of the cathode closest to the anode.

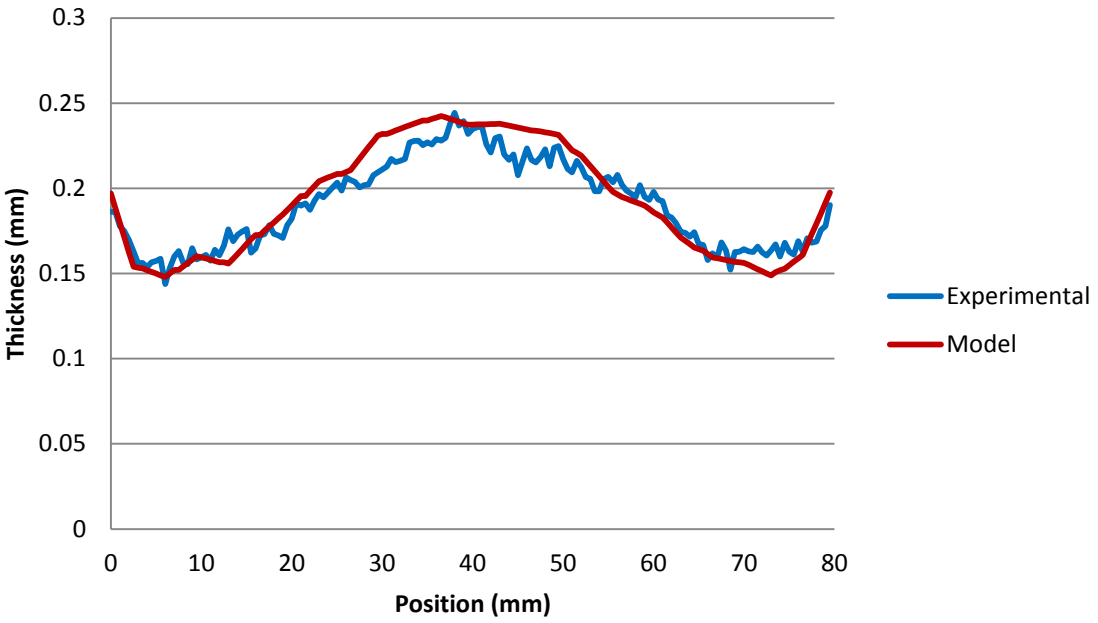

Figure 6.13 Experimental deposit profile and model deposit profile of the Large Pipe with 40 g/L Cu^{2+}, 160 g/L H_2SO_4, 42.9 µg/L thiourea, and 26.4 µg/L glue at 45 °C and t = 14400s

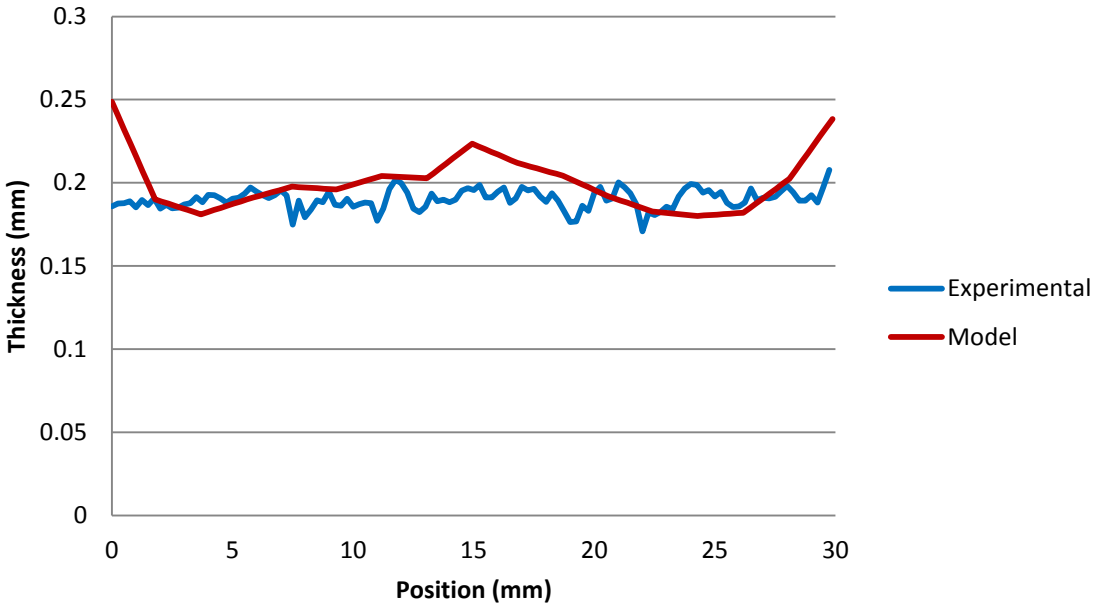

Figure 6.14 Experimental deposit profile and model deposit profile of the Small Pipe with 40 g/L Cu^{2+}, 160 g/L H_2SO_4, 42.9 µg/L thiourea, and 26.4 µg/L glue at 45 °C and t = 14400s

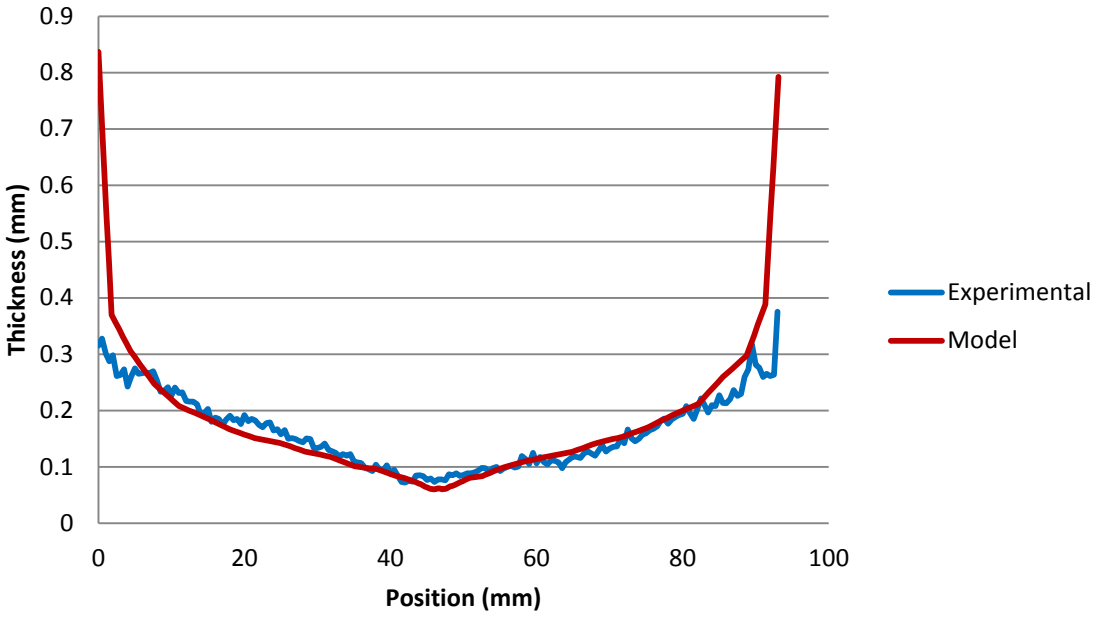

Figure 6.15 Experimental deposit profile and model deposit profile of the Large Angle with 40 g/L Cu^{2+}, 160 g/L H_2SO_4, 42.9 µg/L thiourea, and 26.4 µg/L glue at 45 °C and t = 14400s

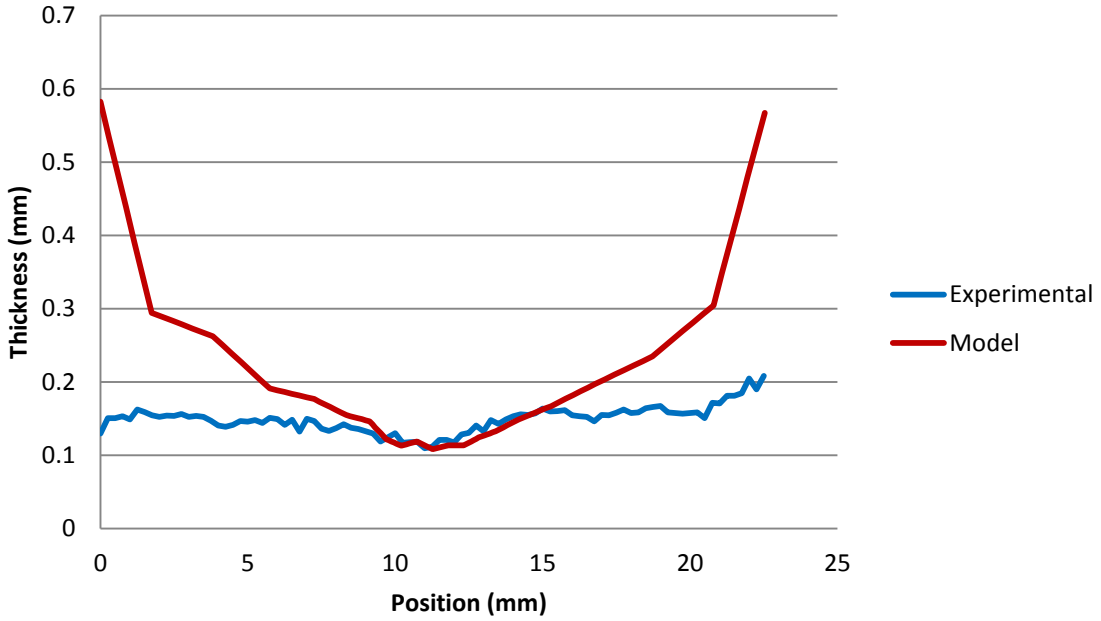

Figure 6.16 Experimental deposit profile and model deposit profile of the Small Angle with 40 g/L Cu^{2+}, 160 g/L H_2SO_4, 42.9 µg/L thiourea, and 26.4 µg/L glue at 45 °C and t = 14400s

Table 6.1

Comparison of the Deposit Ratios of the Shaped Cathodes

	Deposit Ratio		Max/Min Ratio		Linear Ratio	Correlation
	Model	Exp	Model	Exp		
Large Pipe	1.34901	1.268105	1.639248	1.699385	1.986573	0.96767
Small Pipe	1.040011	0.99977	1.334706	1.215658	1.405098	0.161045
Large Angle	2.398879	1.97072	13.09525	5.191803	1.824624	0.859006
Small Angle	2.05389	1.148116	5.206214	1.900978	1.366689	0.748901

Pipe shaped cathodes have much more uniform deposit ratios than angled cathodes because the thicker deposit on the edge of the cathode is close to the anode for the angles and far away from the anode for the pipes. The experimental and model ratios for the large cathode shapes show very good correlation, while the small cathode shapes have poor model accuracy. The small cathode shapes have much smaller linear ratios, so they would be expected to have smaller deposit ratios because of the relatively close proximity of the entire cathode to the anode. However, the deposit ratios are much smaller than model predictions.

Additional modeling was done with the large pipe and angle under the same conditions, but at different standoff distances. A plot of the deposit ratio versus linear ratio is shown in Figure 6.17, and a plot of the maximum/minimum deposit ratio is shown in Figure 6.18.

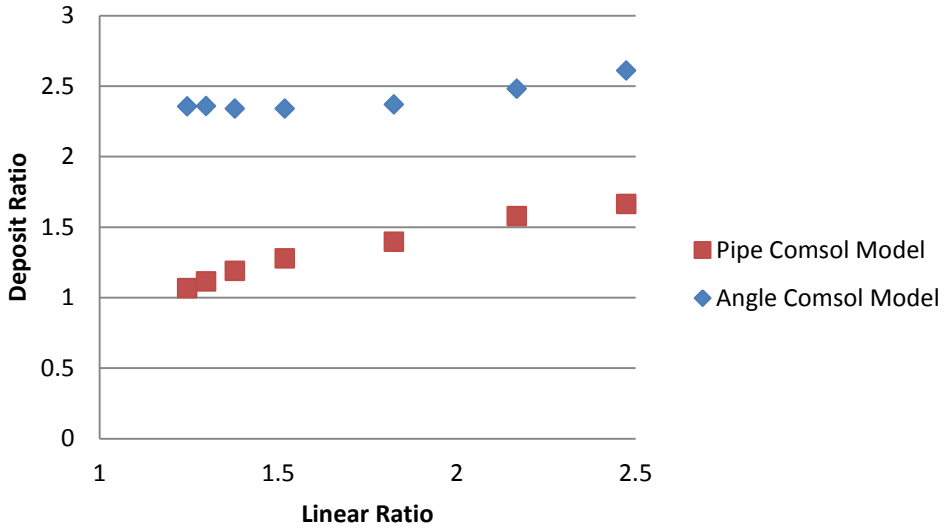

Figure 6.17 Plot of deposit ratio vs. linear ratio from COMSOL model results for the shaped cathode deposits under conditions of 400 A/m^2, 40 g/L Cu^{2+}, 160 g/L H_2SO_4, 42.9 µg/L thiourea, and 26.4 µg/L glue at 45 °C and t = 14400s

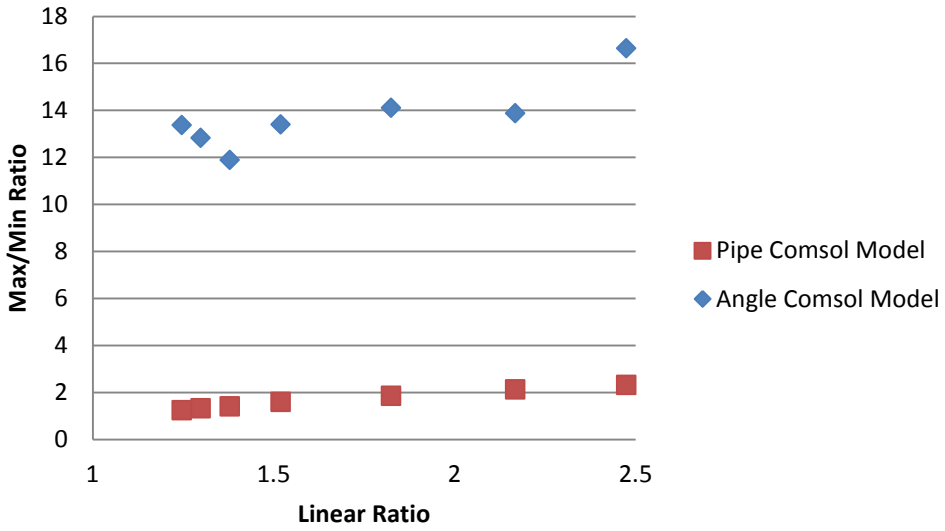

Figure 6.18 Plot of deposit maximum/minimum ratio vs. linear ratio from COMSOL model results for the shaped cathode deposits under conditions of 400 A/m^2, 40 g/L Cu^{2+}, 160 g/L H_2SO_4, 42.9 µg/L thiourea, and 26.4 µg/L glue at 45 °C and t = 14400s

CHAPTER 7

NEW EMPIRICAL DEPOSIT DISTRIBUTION EQUATION

7.1 Equation

Modeling using a software package such as COMSOL Multiphysics has been shown to be effective; nevertheless, not all electroplaters have access to such software. A mathematical equation valid for all complex geometries would be either nearly impossible to generate or impractical to use; however, an equation with accurate results that can be applied to several common geometries other than flat plates or rotating discs could be useful.

An equation was developed to describe the deposit thickness on recessed or protruding areas based on research experience and results from COMSOL simulations of deposition on a pipe and an angle.

$$\frac{T(x)}{T(near)} = \frac{D(near)}{D(x)}^{K1(\frac{Adeposition}{Aflux})^{K2}(\frac{i}{iL})^{K3}} \quad \textbf{(7.1)}$$

where

T(x) is the thickness of the deposit at point *x* on the cathode,

T(near) is the thickness of the deposit at the nearest point on the cathode to the anode,

D(near) is the distance from the cathode to the anode at the nearest point,

D(x) is the distance from the cathode to the anode at point *x* on the cathode,

K_1, K_2, and K_3 are constants discussed below,

$A_{deposition}$ is the area of the cathode available for deposition,

A_{flux} is the area through which the current can travel between the cathode and anode,

i is the current density applied to the cathode, and

i_L is the limiting current density for the cell conditions.

Fifty separate COMSOL models were run under conditions ranging from 30 to 50 g/L Cu^{2+}, 30 to 60 °C, and 40 to 400 A/m^2. Two different geometries were modeled, a 2-inch diameter cylinder and a 2-inch angle. See Section 3.2 for details on the measurements of the geometries. Table 7.1 provides the conditions of each run. All 50 runs assumed a closed cell with 160 g/L H_2SO_4, 42.9 µg/L thiourea, and 26.4 µg/L glue.

The three constants in eq 7.1 were solved for by minimizing the sum of the squared error for all 50 runs. The values of K_1, K_2, and K_3 are 0.609334, 2.909082, and 0.48147, respectively.

The limiting current density, i_L, was calculated by using data from Wilke et al. (*24*). The data was collected at room temperature with varying copper concentrations. By interpolating the data and using eq 1.12 and eq 1.13, the value for the limiting current density was calculated for each of the experimental conditions listed in Table 7.1

This equation does not accurately describe the thick deposit buildup at the edge of the cathode, but it does adequately predict the relative thickness along the rest of the

Table 7.1

Conditions of 50 COMSOL Models and Error of Each Model When Compared to Eq 7.1

Run Number	Geometry	Cu^{2+} Concentration (g/L)	Temperature (C)	Current Density (A/m^2)	Sum Sq Error
1	Pipe	30	30	40	0.112593
2	Pipe	30	30	100	0.075085
3	Pipe	30	30	200	0.120712
4	Pipe	30	30	300	0.190514
5	Pipe	30	30	400	0.292123
6	Pipe	30	60	40	0.156418
7	Pipe	30	60	100	0.094247
8	Pipe	30	60	200	0.113056
9	Pipe	30	60	300	0.162845
10	Pipe	30	60	400	0.212216
11	Pipe	40	45	40	0.061809
12	Pipe	40	45	100	0.03679
13	Pipe	40	45	200	0.095957
14	Pipe	40	45	300	0.125153
15	Pipe	40	45	400	0.25688
16	Pipe	50	30	40	0.015831
17	Pipe	50	30	100	0.079408
18	Pipe	50	30	200	0.160916
19	Pipe	50	30	300	0.149525
20	Pipe	50	30	400	0.11524
21	Pipe	50	60	40	0.046846
22	Pipe	50	60	100	0.024451
23	Pipe	50	60	200	0.116184
24	Pipe	50	60	300	0.192686
25	Pipe	50	60	400	0.231782
26	Angle	30	30	40	0.406363
27	Angle	30	30	100	0.14153
28	Angle	30	30	200	0.245088
29	Angle	30	30	300	0.485832
30	Angle	30	30	400	0.817834
31	Angle	30	60	40	0.859723
32	Angle	30	60	100	0.297077
33	Angle	30	60	200	0.171827
34	Angle	30	60	300	0.214321
35	Angle	30	60	400	0.289063
36	Angle	40	45	40	0.239104

Table 7.1 Continued

Run Number	Geometry	Cu^{2+} Concentration (g/L)	Temperature (C)	Current Density (A/m^2)	Sum Sq Error
37	Angle	40	45	100	0.090108
38	Angle	40	45	200	0.224702
39	Angle	40	45	300	0.21834
40	Angle	40	45	400	0.160218
41	Angle	50	30	40	0.041111
42	Angle	50	30	100	0.422796
43	Angle	50	30	200	0.521628
44	Angle	50	30	300	0.337199
45	Angle	50	30	400	0.215307
46	Angle	50	60	40	0.20853
47	Angle	50	60	100	0.093866
48	Angle	50	60	200	0.457887
49	Angle	50	60	300	0.603199
50	Angle	50	60	400	0.582376

cathode. The pipe models did not include the data within 10 mm of the edge, and the angle models did not include data within 5 mm of the edge. Figures 7.1–7.10 show the predicted deposit thickness of the new empirical eq 7.1 and the COMSOL model.

Taking the natural log of eq 7.1 results in eq 7.2.

$$ln\left(\frac{T(x)}{T(near)}\right) = ln\left(\frac{D(near)}{D(x)}\right) K1(\frac{Adeposition}{Aflux})^{K2}(\frac{i}{iL})^{K3} \qquad \textbf{(7.2)}$$

If the results of the model are plotted with $ln\left(\frac{T(x)}{T(near)}\right)$ versus $ln\left(\frac{D(near)}{D(x)}\right)$, then the slope of the results is $K1(\frac{Adeposition}{Aflux})^{K2}(\frac{i}{iL})^{K3}$. Figures 7.11 and 7.12 contain log-log plots of eq 7.1 at the different conditions described in Table 7.1.

If the edge effects are excluded from the plot, the log-log plot of eq 7.1 applied to the cylinder has improved correlation as shown in Figures 7.13–7.14; however, the log-log plot of eq 7.1 applied to the angle shows minimal improvement. Table 7.2 contains the slope of eq 7.2 for each of the conditions in Table 7.1.

7.2 Effect of K Values

The K values solved for in this study are valid for solutions of copper sulfate with sulfuric acid over a range of temperatures and concentrations. If a different solution were to be used, new K values would need to be calculated. This study has not included data from other plating baths, but Figures 7.15–7.17 show the effect of varying K values on the deposit distribution.

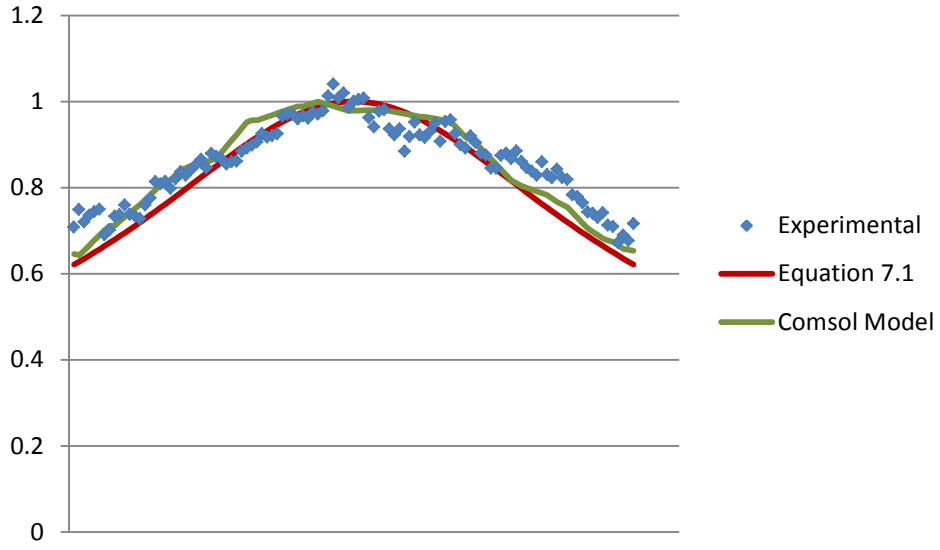

Figure 7.1 Experimental deposit profile, COMSOL model deposit profile, and predicted deposit profile using eq 7.1 on a Large Pipe with 40 g/L Cu^{2+}, 160 g/L H_2SO_4, 42.9 µg/L thiourea, and 26.4 µg/L glue at 45 °C and t= 14400s and i = 400 A/m^2

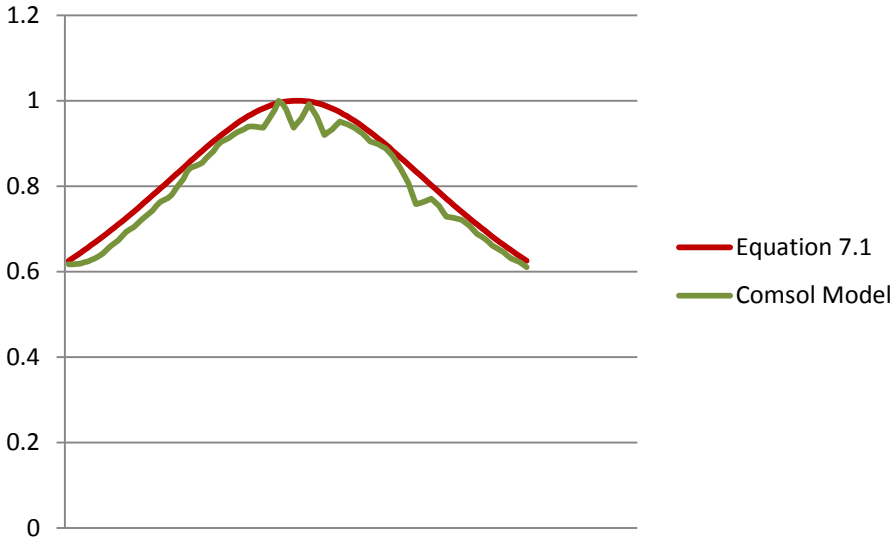

Figure 7.2 COMSOL model deposit profile and predicted deposit profile using eq 7.1 on a Large Pipe with 40 g/L Cu^{2+}, 160 g/L H_2SO_4, 42.9 µg/L thiourea, and 26.4 µg/L glue at 45 °C and t = 14400s and i = 300 A/m^2

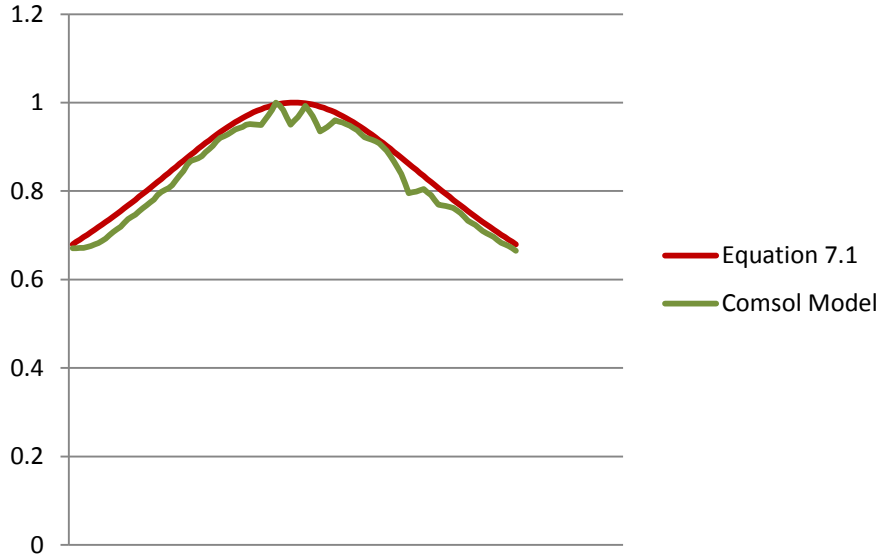

Figure 7.3 COMSOL model deposit profile and predicted deposit profile using eq 7.1 on a Large Pipe with 40 g/L Cu^{2+}, 160 g/L H_2SO_4, 42.9 µg/L thiourea, and 26.4 µg/L glue at 45 °C and t = 14400s and i = 200 A/m^2

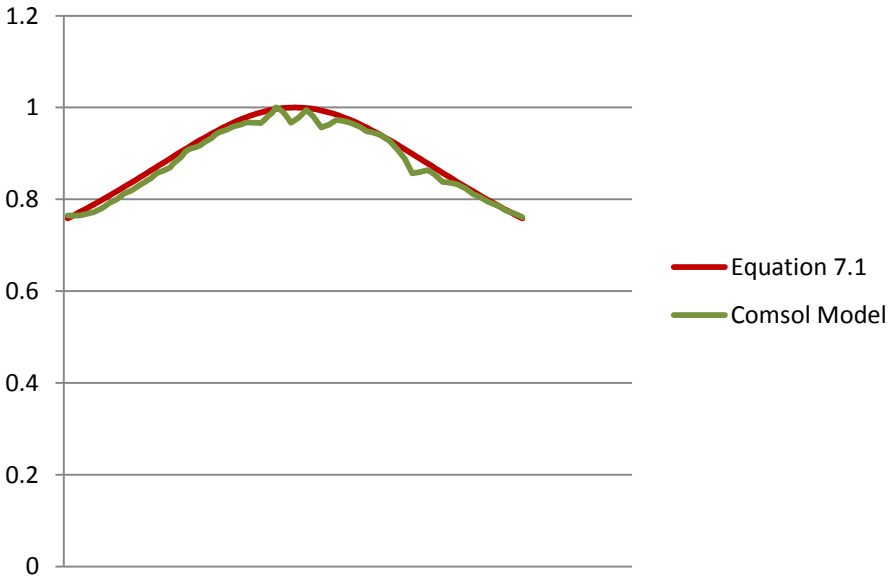

Figure 7.4 COMSOL model deposit profile and predicted deposit profile using eq 7.1 on a Large Pipe with 40 g/L Cu^{2+}, 160 g/L H_2SO_4, 42.9 µg/L thiourea, and 26.4 µg/L glue at 45 °C and t = 14400s and i = 100 A/m^2

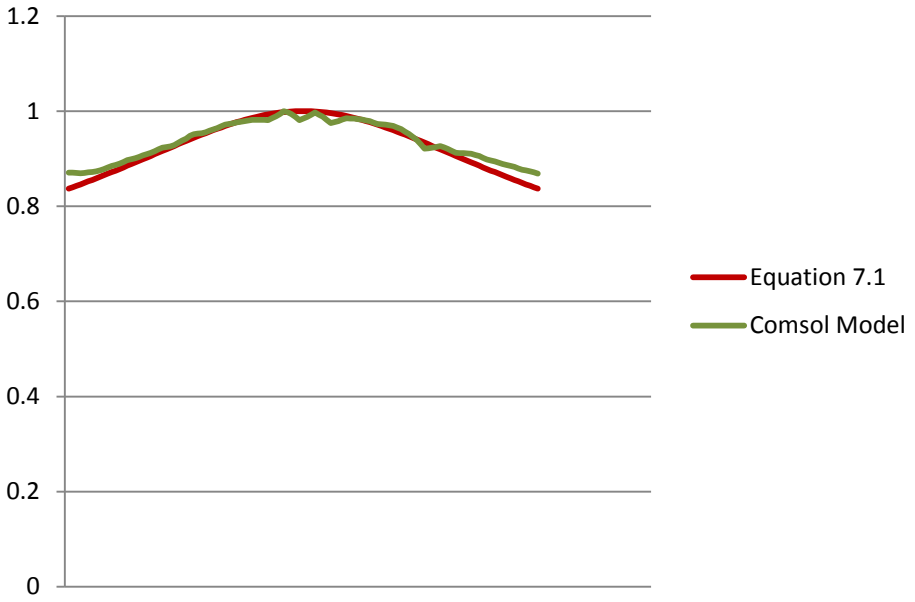

Figure 7.5 COMSOL model deposit profile and predicted deposit profile using eq 7.1 on a Large Pipe with 40 g/L Cu^{2+}, 160 g/L H_2SO_4, 42.9 µg/L thiourea, and 26.4 µg/L glue at 45 °C and t = 14400s and i = 40 A/m^2

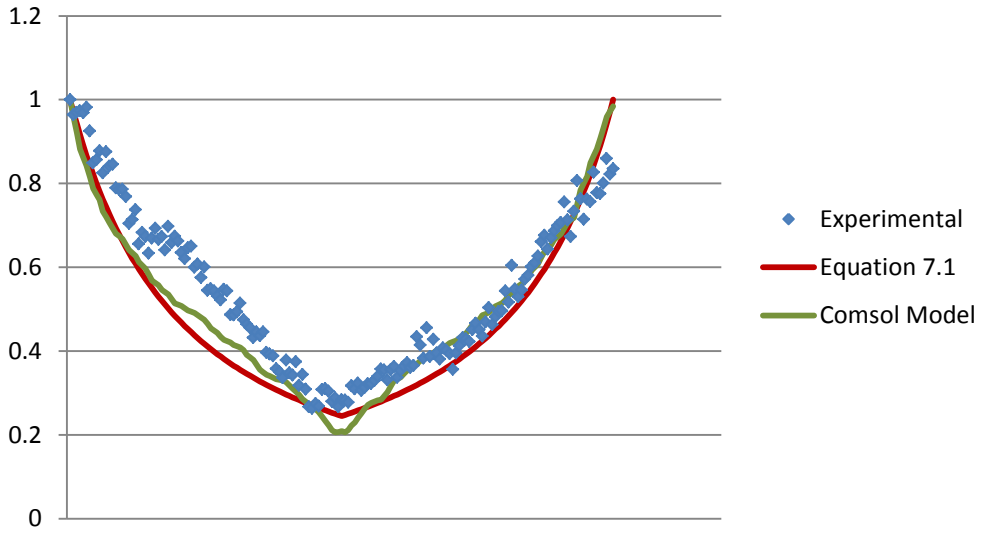

Figure 7.6 Experimental deposit profile, COMSOL model deposit profile, and predicted deposit profile using eq 7.1 on a Large Angle with 40 g/L Cu^{2+}, 160 g/L H_2SO_4, 42.9 µg/L thiourea, and 26.4 µg/L glue at 45 °C and t = 14400s and i = 400 A/m^2

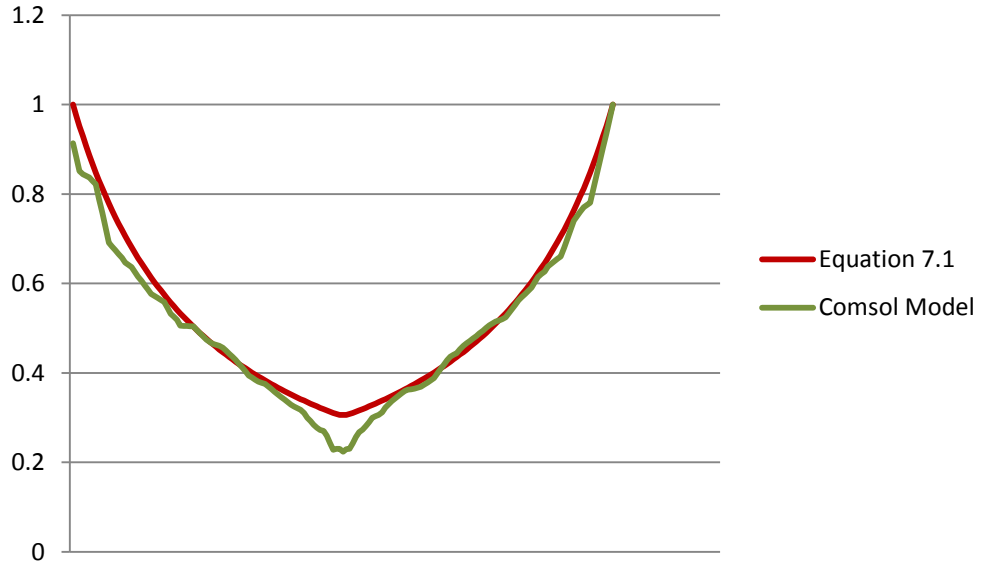

Figure 7.7 COMSOL model deposit profile and predicted deposit profile using eq 7.1 on a Large Angle with 40 g/L Cu^{2+}, 160 g/L H_2SO_4, 42.9 µg/L thiourea, and 26.4 µg/L glue at 45 °C and t = 14400s and i = 300 A/m^2

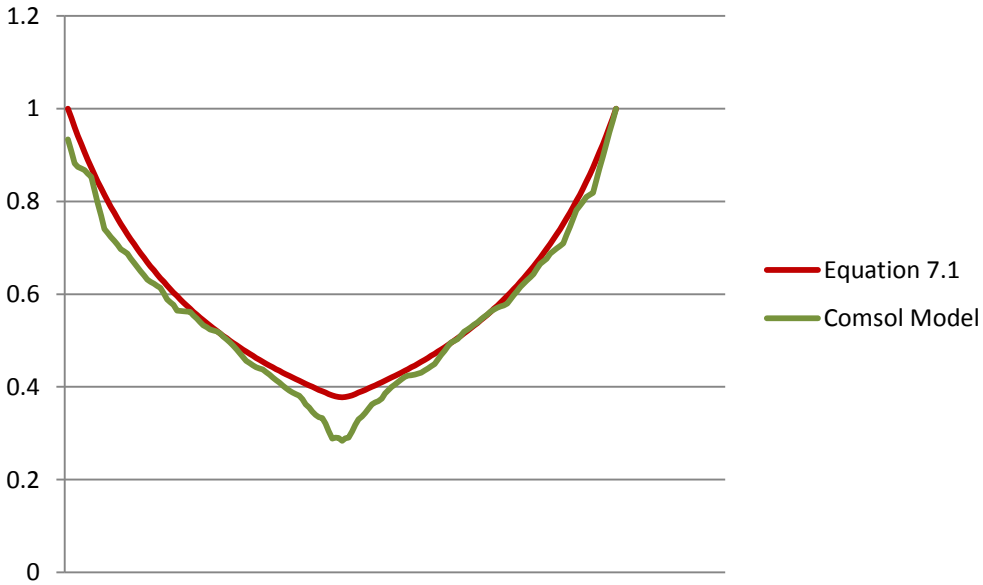

Figure 7.8 COMSOL model deposit profile and predicted deposit profile using eq 7.1 on a Large Angle with 40 g/L Cu^{2+}, 160 g/L H_2SO_4, 42.9 µg/L thiourea, and 26.4 µg/L glue at 45 °C and t = 14400s and i = 200 A/m^2

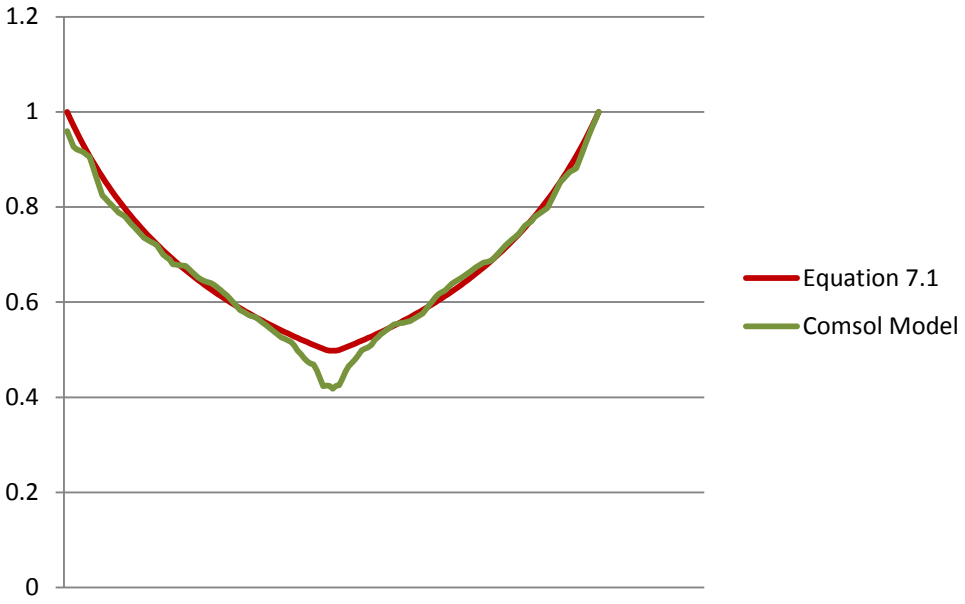

Figure 7.9 COMSOL model deposit profile and predicted deposit profile using eq 7.1 on a Large Angle with 40 g/L Cu^{2+}, 160 g/L H_2SO_4, 42.9 µg/L thiourea, and 26.4 µg/L glue at 45 °C and t = 14400s and i = 100 A/m^2

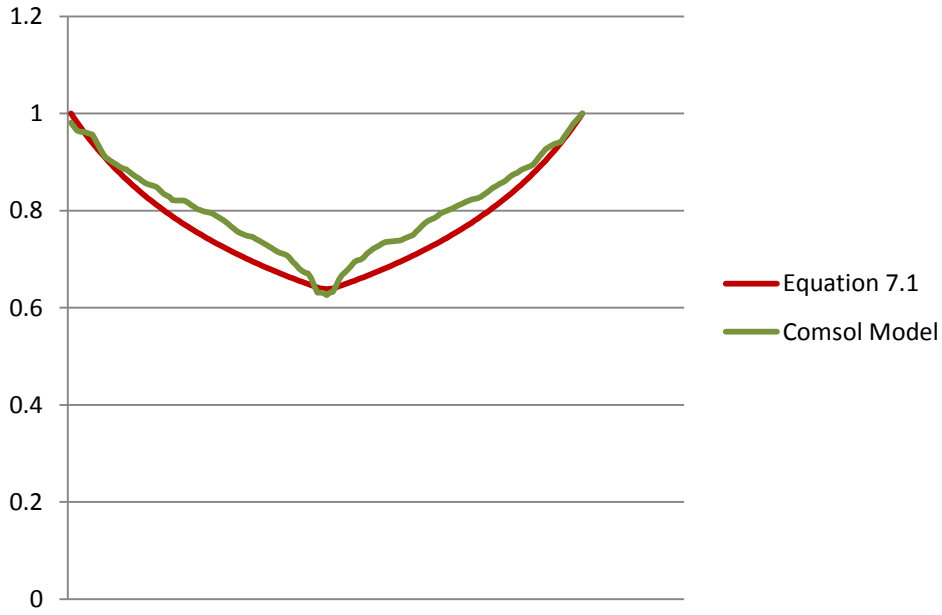

Figure 7.10 COMSOL model deposit profile and predicted deposit profile using eq 7.1 on a Large Angle with 40 g/L Cu^{2+}, 160 g/L H_2SO_4, 42.9 µg/L thiourea, and 26.4 µg/L glue at 45 °C and t = 14400s and i = 40 A/m^2

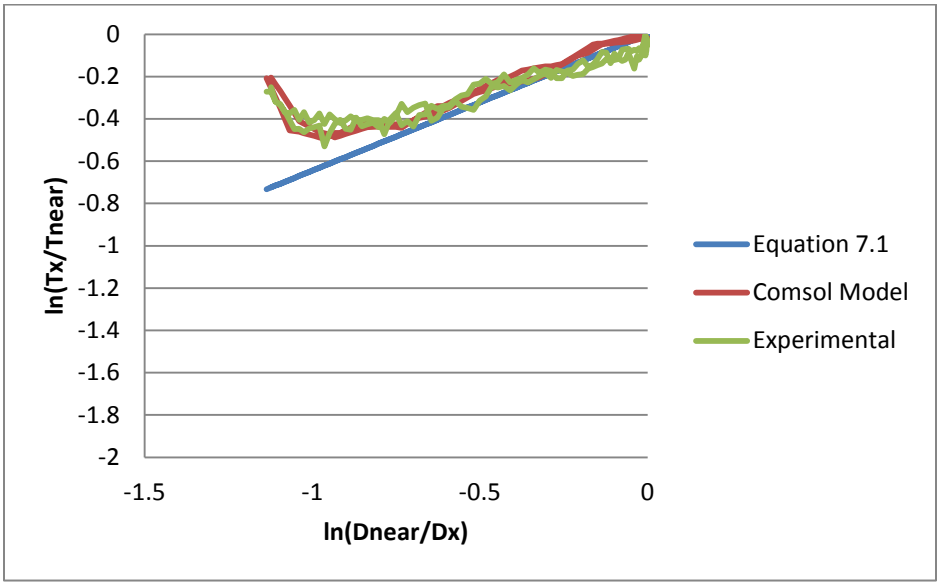

Figure 7.11 Log-log plot of eq 7.1, COMSOL Model, and experimental deposition thicknesses on a 2-inch cylinder with 30 g/L Cu^{2+}, 160 g/L H_2SO_4, 42.9 µg/L thiourea, and 26.4 µg/L glue at 30 °C and t = 14400s and *i* ranging from 40 to 400 A/m^2

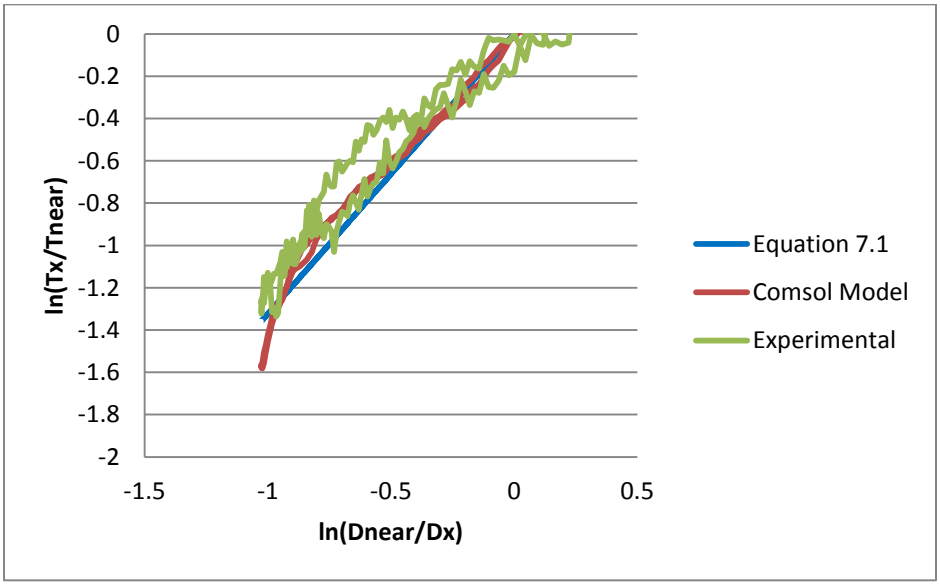

Figure 7.12 Log-log plot of eq 7.1, COMSOL Model, and experimental deposition thicknesses on a 2-inch angle with 30 g/L Cu^{2+}, 160 g/L H_2SO_4, 42.9 µg/L thiourea, and 26.4 µg/L glue at 30 °C and t = 14400s and *i* ranging from 40 to 400 A/m^2

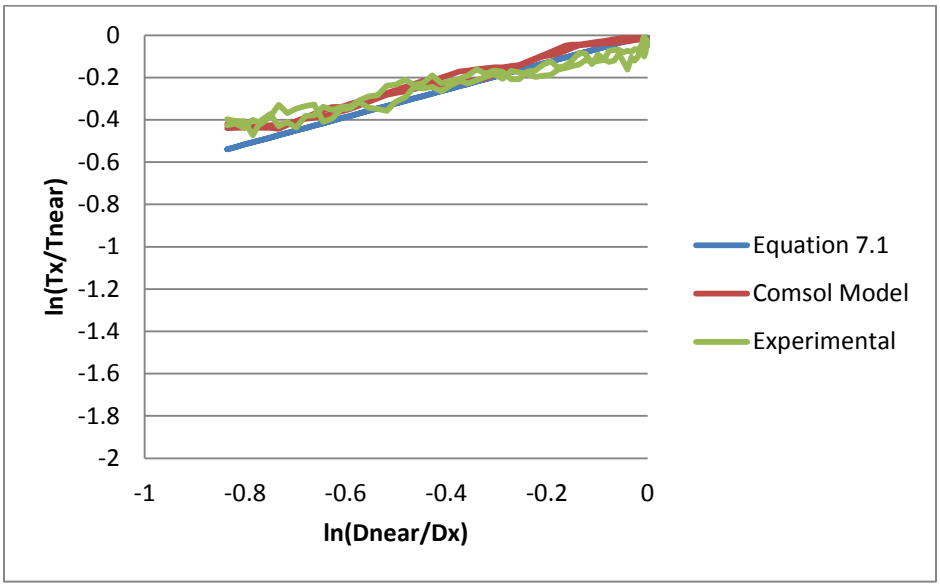

Figure 7.13 Log-log plot of eq 7.1, COMSOL Model, and experimental deposition thicknesses on a 2-inch cylinder with the 10 mm of the cathode closest to the edge excluded and 30 g/L Cu^{2+}, 160 g/L H_2SO_4, 42.9 µg/L thiourea, and 26.4 µg/L glue at 30 °C and t = 14400s and *i* ranging from 40 to 400 A/m^2

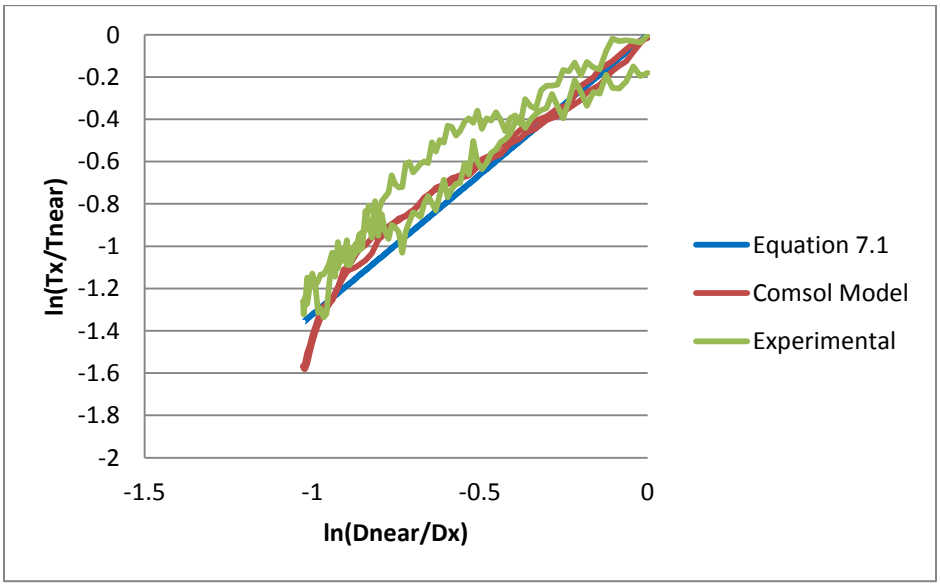

Figure 7.14 Log-log plot of eq 7.1, COMSOL Model, and experimental deposition thicknesses on a 2-inch angle with the 5 mm of the cathode closest to the edge excluded and 30 g/L Cu^{2+}, 160 g/L H_2SO_4, 42.9 µg/L thiourea, and 26.4 µg/L glue at 30 °C and t = 14400s and *i* ranging from 40 to 400 A/m^2

Table 7.2

Conditions of 50 COMSOL Models and the Slope of a Log-Log Plot According to Eq 7.2

Run Number	Geometry	Cu^{2+} Concentration (g/L)	Temperature (C)	Current Density (A/m^2)	Slope of log-log plot
1	Pipe	30	30	40	0.296192456
2	Pipe	30	30	100	0.460436992
3	Pipe	30	30	200	0.642846303
4	Pipe	30	30	300	0.781429544
5	Pipe	30	30	400	0.897519914
6	Pipe	30	60	40	0.212879828
7	Pipe	30	60	100	0.330925876
8	Pipe	30	60	200	0.462027334
9	Pipe	30	60	300	0.561630061
10	Pipe	30	60	400	0.645066683
11	Pipe	40	45	40	0.212778775
12	Pipe	40	45	100	0.330768787
13	Pipe	40	45	200	0.461808012
14	Pipe	40	45	300	0.561363459
15	Pipe	40	45	400	0.644760473
16	Pipe	50	30	40	0.224643061
17	Pipe	50	30	100	0.349212052
18	Pipe	50	30	200	0.487557865
19	Pipe	50	30	300	0.592664403
20	Pipe	50	30	400	0.680711533
21	Pipe	50	60	40	0.161455754
22	Pipe	50	60	100	0.250986142
23	Pipe	50	60	200	0.350418225
24	Pipe	50	60	300	0.425960532
25	Pipe	50	60	400	0.489241881
26	Angle	30	30	40	0.607945616
27	Angle	30	30	100	0.945063406
28	Angle	30	30	200	1.319465046
29	Angle	30	30	300	1.603912108
30	Angle	30	30	400	1.842191746
31	Angle	30	60	40	0.436943466
32	Angle	30	60	100	0.679237204
33	Angle	30	60	200	0.948327639
34	Angle	30	60	300	1.152765802
35	Angle	30	60	400	1.324022454
36	Angle	40	45	40	0.436736052

Table 7.2 Continued

Run Number	Geometry	Cu^{2+} Concentration (g/L)	Temperature (C)	Current Density (A/m^2)	Slope of log-log plot
37	Angle	40	45	100	0.678914774
38	Angle	40	45	200	0.947877473
39	Angle	40	45	300	1.152218591
40	Angle	40	45	400	1.323393948
41	Angle	50	30	40	0.461087923
42	Angle	50	30	100	0.716770236
43	Angle	50	30	200	1.000729968
44	Angle	50	30	300	1.216464898
45	Angle	50	30	400	1.397184785
46	Angle	50	60	40	0.331393713
47	Angle	50	60	100	0.515158039
48	Angle	50	60	200	0.719245948
49	Angle	50	60	300	0.874299238
50	Angle	50	60	400	1.004186471

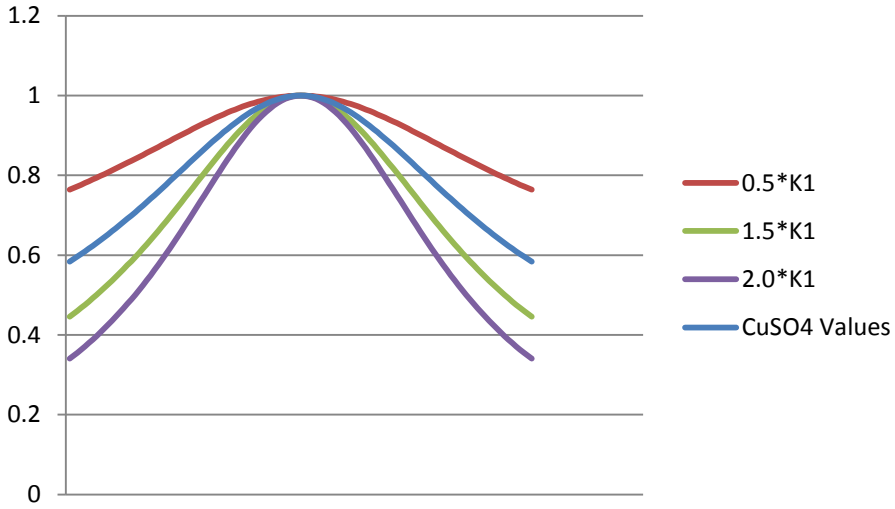

Figure 7.15 Plot of the effects of different K_1 values on the deposit distribution using eq 7.1 and K values from $CuSO_4$ as a baseline

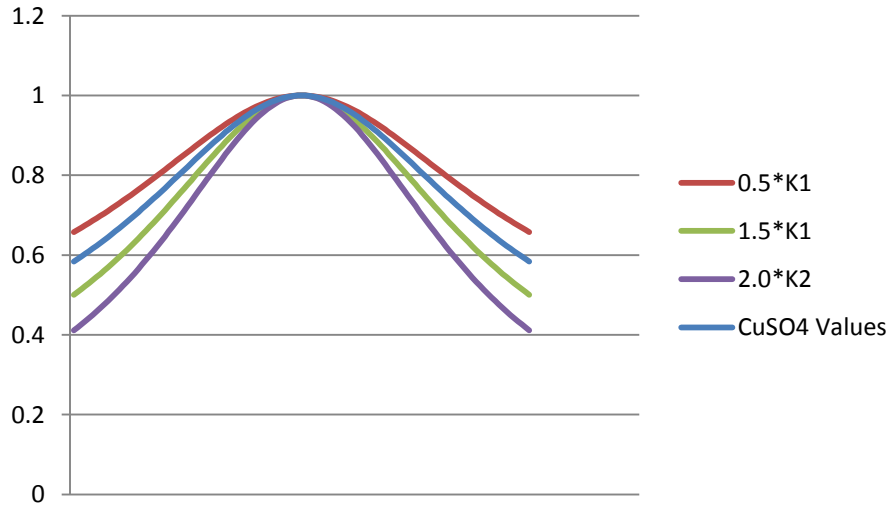

Figure 7.16 Plot of the effects of different K_2 values on the deposit distribution using eq 7.1 and K values from $CuSO_4$ as a baseline

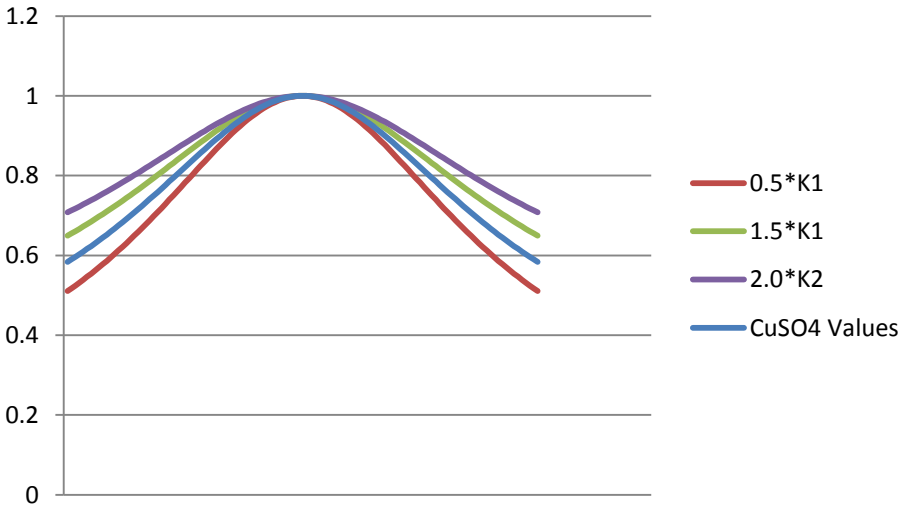

Figure 7.17 Plot of the effects of different K_3 values on the deposit distribution using eq 7.1 and K values from $CuSO_4$ as a baseline

CHAPTER 8

HARING–BLUM RESULTS AND DISCUSSION

8.1 Haring–Blum Experimental Setup

A Haring–Blum cell measures 60-cm by 10-cm by 10-cm with cathodes on each end of the cell. A single anode is placed between the two cathodes and can be placed at varying locations to produce different distance ratios between the near and far anode. In the experiments published by Haring and Blum (*7*) the anode was 10 cm from the "near" cathode and 50 cm from the "far" cathode. This geometry was reproduced in COMSOL and is shown in Figure 8.1.

Each condition was modeled using the geometry shown and the parameters in Table 8.1. The ratio of mass electrodeposited on each cathode was modeled and compared to that of the results of the Haring–Blum paper.

A comparison of the experimental results of Haring and Blum with the COMSOL model results shows some correlation; nevertheless, many of the comparisons show opposite effects of the electrodeposition conditions. Increasing sulfuric acid concentration in the model increased the deposition ratio; contrarily, in the Haring–Blum experiments the ratio decreased. This disparity is due to the manner in which COMSOL calculates the conductivity of the solution. The conductivity is calculated by using eq 4.3, which is solely dependent on the diffusivity of the solution; yet, in the case of copper

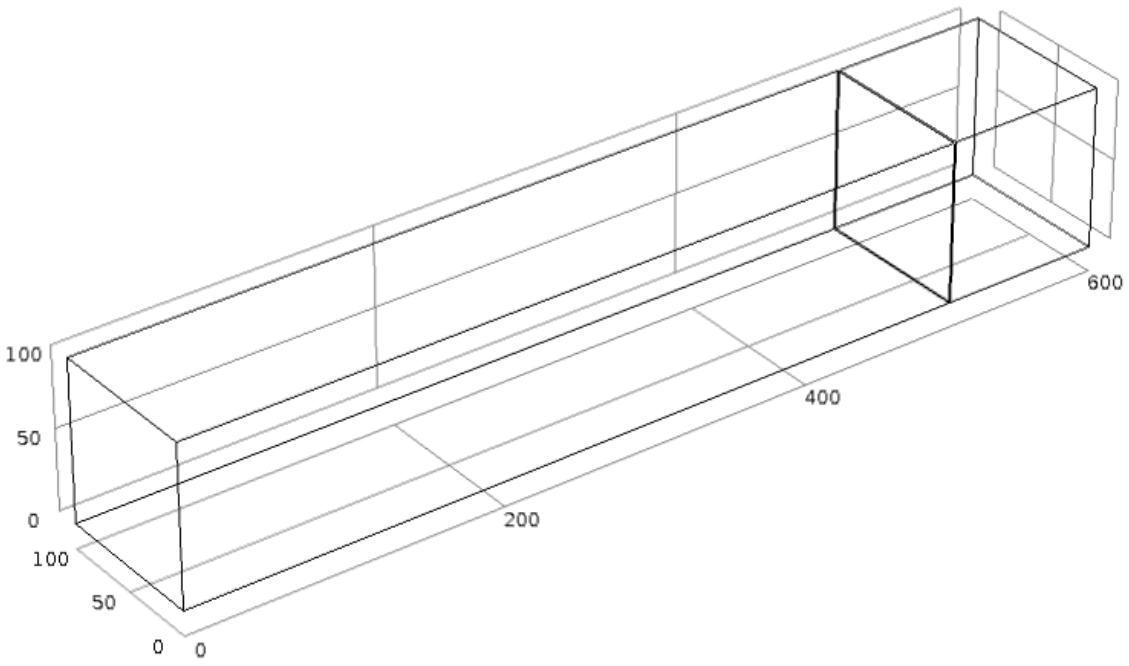

Figure 8.1 Model geometry of Haring–Blum Cell with units in mm

Table 8.1

Haring–Blum Model Comparison

Cu (M)	H2SO4 (M)	I (A)	T (C)	Time (min)	Model Ratio	Haring–Blum Ratio	Model to Haring–Blum Ratio
1.5	0.5	2	21	60	3.582113	4.8	0.746274
1.5	1	2	21	60	3.835185	4.67	0.821239
1.5	1.5	2	21	60	4.159696	4.53	0.918255
1.5	2	2	21	60	4.477075	4.46	1.003828
1	1.5	2	21	60	4.226087	4.46	0.947553
1.5	1.5	2	21	60	4.159696	4.53	0.918255
2	1.5	2	21	60	4.119349	4.64	0.887791
1.5	1.5	1	21	60	3.779565	4.52	0.836187
1.5	1.5	2	21	60	4.159696	4.53	0.918255
1.5	1.5	3	21	40	4.395786	4.59	0.957688
1.5	1.5	4	21	30	4.529517	4.63	0.978297
1.5	1.5	2	45	60	3.709414	4.89	0.758571

sulfate, adding sulfuric acid decreases the diffusivity while increasing the conductivity.

Increasing the copper concentration and increasing temperature also produced opposing effects between the model and the experimental results. Increasing current density increased the deposit ratio for both the model and the experiments; still, the effect of the current density was much stronger in the model.

CHAPTER 9

CONCLUSIONS

Extensive literature searches have yielded numerous papers describing the throwing power of solutions and many more papers with derived models to describe electrodeposition. However, the throwing power is specific to a certain plating cell geometry and is only useful for describing the relative behavior of the plating solution without being able to describe deposition on other plating geometries. In addition, the models in literature are seldom verified by experimental results, which casts doubt on the accuracy and effectiveness of the published models.

This study has attempted to address the lack of modeling applicable to multiple geometries by conducting copper electrodeposition experiments in conjunction with commercially available finite element based software modeling and numerical modeling.

According to the study presented in the experimental results and discussion sections, the following conclusions were made:

1. Experimental and modeling data predict thicker deposits and higher current densities at cathode edges; nonetheless, model results are less accurate at predicting the deposit thickness at the edges.
2. Model results are more accurate at elevated concentration levels and temperatures; at lower temperatures and concentrations, the deposits also develop

more irregular features, which modeling does not predict.

3. Smaller cathodes tend to have small linear ratios, which result in deposits that are quite uniform across the cathode area. The 3-D model has difficulty predicting the deposit thickness when there is a small linear ratio.
4. Natural convection in an electrodeposition model has a significant effect on the results of the deposition prediction.
5. An asymmetrical plating cell can cause unusual solution flow patterns in the model, which slow the calculations down by more than an order of magnitude.
6. 3-D modeling with a COMSOL Multiphysics software package can produce a model that is reasonably accurate as long as the feature that is being modeled is not too small.
7. A numerical equation has been derived that can predict electrodeposition thickness on protruding or recessed cathode features in a copper sulfate solution with accuracy comparable to a 3-D model. It does not predict deposition behavior at the edges of the cathode.

REFERENCES

1. Dini, J. W.; Snyder, D. D. *Modern Electroplating*, 5th ed.; John Wiley & Sons: Hoboken, NJ, 2010.

2. Weisenberger, L. M.; Durkin, B. J. Copper plating. In *ASM Handbook* Vol 5 Surface Engineering; ASM International: Materials Park, OH, 1994; pp 167–176.

3. Jernstedt, G. W.; Ceresa, M. (Westinghouse Electric Corp., USA) Acid copper plating. US Patent 2,700,019, January 18, 1955.

4. Casas, J. M.; Alvarez, F.; Cifuentes, L. Aqueous speciation of sulfuric acid-cupric sulfate solutions. *Chem. Eng. Sci.* **2000**, *55*, 6223–6234.

5. Foulkes, J. T.; Hinatsu, F.R. Diffusion coefficients for copper (II) in aqueous cupric sulfate-sulfuric acid solutions. *J. Electrochem. Soc.* **1989,** *136*, 125–132.

6. Moats, M. S.; Hiskey, J. B.; Collins, D. W. The effect of copper, acid, and temperature on the diffusion coefficient of cupric ions in simulated electrorefining electrolytes. *Hydrometallurgy* **2000**, *56*, 255–268.

7. Haring, H. E.; Blum, W. Current distribution and throwing power in electrodepostion. *Am. Electrochem. Soc.* **1923**, *44*, 313.

8. Jelinek, R. V.; David, H. F. Throwing index, a new graphical method for expressing results of throwing-power measurements. *J. Electrochem. Soc.* **1957**, *104*, 279.

9. Chin, D. T. A logarithmic throwing index of the measurement of throwing powers. *J. Electrochem. Soc.* **1971**, *118*, 818–821.

10. Assaf, Y. A new test for determining throwing power factor and improving covering power. *Metal Finishing* **2002**, *100*, 12–14.

11. Sanicky, M. K. A versatile plater's tool: all about the hull cell. *Plat. Surf. Finish.* **1985**, *72*, 20–21.

12. Hull, R. O. Current density characteristics, their determination and applications. *Proc. Am. Electroplaters' Soc.* **1939**, *27*, 52–60.

13. Dunigan, E. The Finishing Experts. http://www.thefinishingexperts.com /knowledgebase/perdiodic-table/ (accessed 5/11/2013)

14. Price, D.; Davenport, W. Densities, electical conductivities, and viscosities of CuSO4/H2SO4 solutions in the range of modern electrorefining and electrowinning electrolytes. *Metall. Trans.* **1980**, *11B*, 159.

15. Krzewska, S.; Pajdowski, L.; Podsiadly, H.; Podsiadly, J. Electrochemical determination of thiourea and glue in the industrial copper electrolyte. *Metall. Trans.* **1984**, *15B*, 451.

16. Wu, B.; Wan, C.; Wang, Y. Modeling of acid copper anisotropic deposition based on detailed calculation of the electrolyte composition. *J. Electrochem. Soc.* **2003**, *150*, C7–C15.

17. Wagner, C. Theoretical analysis of the current density distribution in electrolytic cells. *J. Electrochem. Soc.* **1951**, *98*, 116–128.

18. Poon, G. K.; Williams, D. J. Modeling of acid copper electroplating: a review. *J. Electron. Manuf.* **1998**, *8*, 15–37.

19. Introduction to Electrodeposition Module. http://www.comsol.com/model /download/121707/IntroductionToElectrodepositionModule.pdf (accessed 10/10/2013).

20. Mattsson, E.; Bockris, J. O'M. Galvanostatic studies of the kinetics of deposition and dissolution in the copper + copper sulphate system. *Trans. Far. Soc.* **1958**, *55*, 1586–1601.

21. Mathew, R. J. Increasing oxygen charge transfer resistance on the anode in copper electrowinning. In *Electrometallurgy 2012*; John Wiley & Sons: Hoboken, NJ, 2012; pp 41–48.

22. Smyrl, W. H.; Newman, J. Current distribution at electrode edges at high current densities. *J. Electrochem. Soc.* **1989**, *136*, 132–139.

23. German, R. M. *Powder Metallurgy*; Metal Powder Industries Federation: Princeton, 2005; pp 61–62.

24. Wilke, C. R.; Eisenberg, M.; Tobias, C. W. Correlation of limiting currents under free convection conditions. *J. Electrochem. Soc.* **1953**, *100*, 513–523.